University of Kent

The Solid-State Tautomerism of Donor-Acceptor Stenhouse Adduct Solvatomorphs

Thomas J. Hitchings

Supervisor: Helena J. Shepherd

School of Physical Sciences

Date of Submission: 4th January 2021

Contents

Abstract

Donor-Acceptor Stenhouse Adducts (DASAs) are a class of photoresponsive molecules that isomerise reversibly with visible light. The isomerism manifests as an observable colour change through the breaking and reformation of the pi-conjugated core - photochromism. DASAs have been subject to synthetic and solution-state investigations since their discovery in 2014. This work seeks to understand the first-ever observed instance of solid-state switching of DASA single-crystals and the effect of solvation upon the switching properties. It is believed that the solvation of the crystal structure allows sufficient molecular freedom to undergo dramatic structural changes within the solid-state. The materials' response to temperature, humidity and mechanical force has also been investigated as a means of inducing solid-state switching of the material. This project's consequences could see DASAs being used in new real-world applications as sensors, dopants in smart composite materials, and in the production of mechanically active materials for use in soft robotics and molecular motors.

1 Introduction

1.1 Molecular Photoswitches

Molecular photoswitches are a class of organic molecule that exhibits a response to radiation within various regions of the electromagnetic spectrum. These responses can cause a change in the molecule's electronic and chemical structure, resulting in changes to the molecule's macroscopic properties. This change in the properties of the molecular materials should be reversible for these systems to be considered a switch.[1] How these materials switch is usually through isomerism, or in some cases more specifically tautomerism, of the molecules between two metastable forms on exposure to light. Photoexcitation of these molecules results in structure changes during the isomerisation processes, but these are dependent on the molecular switch in question as different switches have different switching mechanisms. In the solid-state, structure-property relationships can be used to rationalise these systems' switching behaviour, with a long-term view to tailoring their properties for applications. Examples include sensors,[2] soft robotics and artificial muscles,[3–6] pigments and dyes, for anticounterfitting,[7–9] and molecular circuitry as logics or optical storage.[10–14] Practically, all these applications require stimuli-induced switching to occur in the solid-state or as part of a matrix for real-world devices to be feasible.

Among the standard, well-characterised organic photoswitches include azobenzenes,[15] diarylethenes,[16] fulgides,[17] oxazole and triazoles,[18] spiropyrans,[19] and others.[20] Examples of some of these systems can be seen in Figure 1. Some of these materials switch with specific wavelengths and can be reversed with another specified wavelength; others switch on irradiation and then reverse upon the radiation's removal. See the individual sections (1.1.1 – 1.1.3) for more detail on some of the more well studied photoswitching molecules.

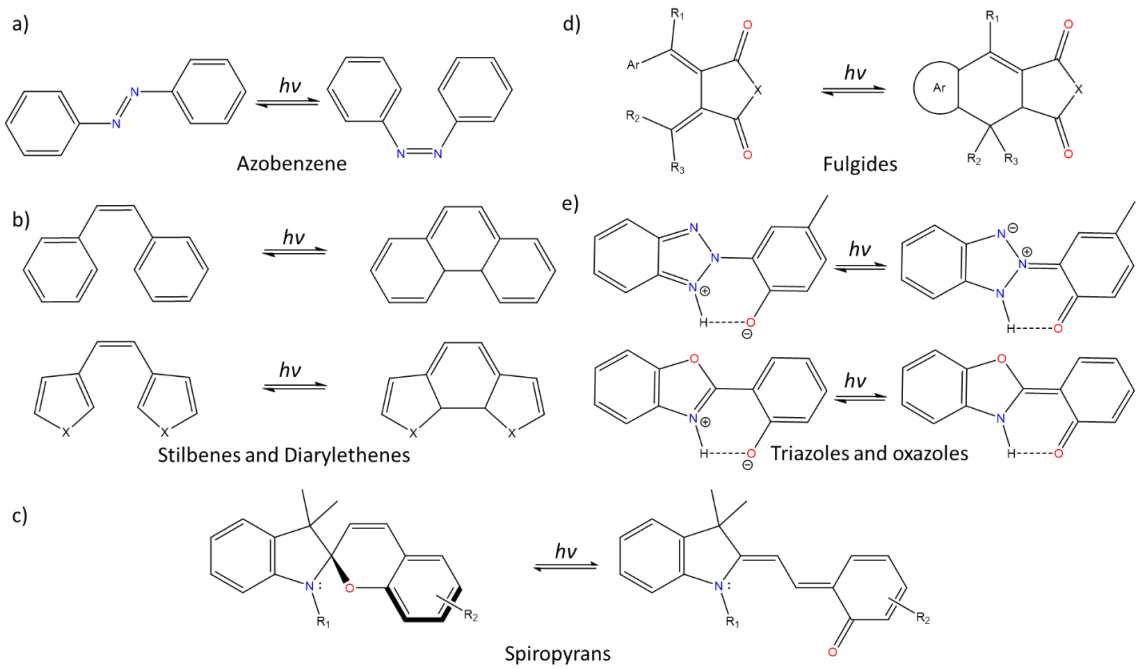

Figure 1. Examples of molecular photoswitches (produced using ChemOffice Pro)[21] of: a) azobenzene,[15] b) stilbenes and diarylethenes,[16] c) spiropyrans,[22] d) fulgides,[17] and e) triazole and oxazoles.[23]

All molecular photoswitches have a delocalised π-system which is important for absorbing photons of UV/visible wavelength. The π-electrons are promoted to an excited state through the absorption of these photons, initiating the photoswitching. Further details of some switching mechanisms will be discussed in later sections. The de-excitation process is where some of these switches' physical properties arise, like colour or fluorescence. The de-excitation efficiency is referred to as the quantum yield and is the ratio of the photons emitted to the number of photons absorbed.[24,25] The quantum yield is used in this field to give an idea of the efficiency of the photoswitches. Another indicator of this is the molecules switching fatigue.

Fatigue in the context of photoswitches refers explicitly to the loss of photoswitching molecules through side reactions, photodegradation or photo-bleaching. The breakdown of a molecule on exposure to light or through side reactions occurs alongside the photoswitching, resulting in a lower quantity of the photoswitching material.[26] This affects the number of switching cycles a material can undergo until the material no longer exhibits reversible photoswitching. This distinction between switching efficiency (quantum yield) and reversibility is crucial when researching these materials, as both are important when considering real-world applications.

1.1.1 Azo compounds

Discovered in 1858,[27] by the early 1900s, the photoactivity of azo compounds was being explored, and by the 1970s, of manufactured dyes, 60% were azo compounds.[28] The diazo bond is defined as two pi-bonded nitrogen atoms (R-N=N-R') with aromatic or aryl groups bonded as R-groups, which give rise to a large family of azo compounds, depicted in Figure 1a. For decades, azo compounds have been used as organic dyes, so usually, at least one R-group is an aromatic component is modified by the addition of various auxochromes to increase the amount of light absorbed by the molecules.[29,30]

Azobenzene is a common example of a molecular photoswitch with the two isomers depicted in Figure 1a. The material switches by E/Z isomerism of the azo bond initiated by exposure to UV/blue light. The reverse isomerism occurs by thermal processes in the dark, which indicates the thermodynamic stability of the trans isomer.[31] The elusive mechanism by which this switching occurs has been subject to great interest since the discovery of these compounds, and although proposals for the mechanism have been suggested, none are yet wholly accepted. The most popular mechanisms: rotation, inversion, concerted inversion, and inversion-assisted rotation, have been summarised in Figure 2.[15,32]

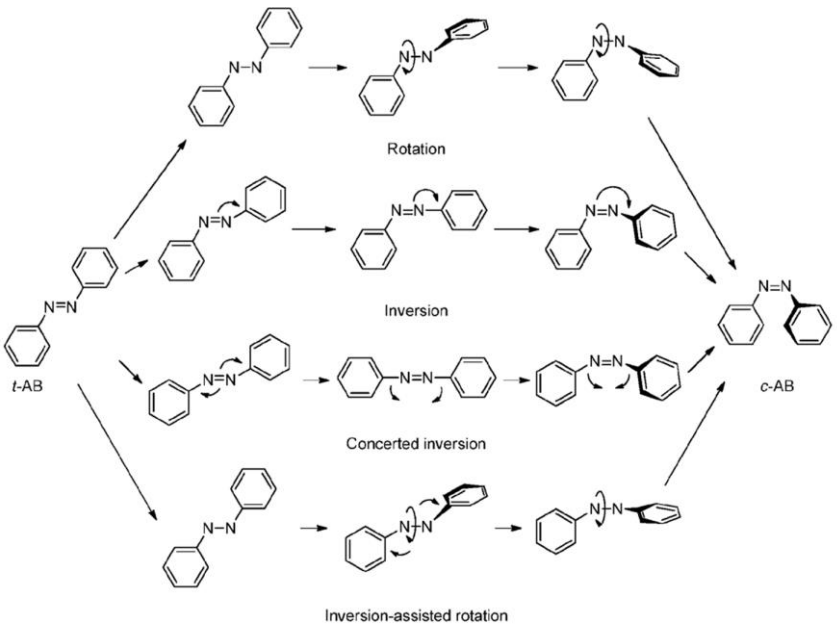

Figure 2. Proposed mechanisms for the E/Z isomerism of trans-azobenzene(t-AB) to cis-azobenzene(c-AB). (reproduced with permissions from the Royal Society of Chemistry).[15,32]

All these proposed mechanisms break the C_{2h} symmetry of the planar structure to adopt the non-planar C_2 symmetry of the trans-isomer. The symmetry change disrupts the delocalised π-system and results in a contraction of molecular length. The impact of this gives rise to properties including molecular motion and photo-actuation, photochromism, and photo-orientation.[11] These properties can be produced and enhanced by modulating regions of supramolecular structures, such as liquid crystals and polymer systems[33] and even metal-organic frameworks (MOFs)[34,35] to give rise to photoresponsive properties not previously associated with azobenzene materials alone.

Azobenzene has been incorporated through dispersion into solid-state materials like polymers with quantum yields similar to that of solution-state (86 %) at room temperature.[36] Development in this field has produced polymers with azobenzene within the polymer's backbone, side chains, and liquid crystalline gels. Photoactuators are an exciting product of this research developed as artificial flytraps,[37] molecular tweezers,[38] underwater motion,[39] and even artificial irises.[40]

1.1.2 Diarylethenes

Another of the well classified molecular photoswitches are stilbenes, one of the largest families of photoswitches. Their range is due to the diversity accomplished by modulation of the molecule without impacting the reversible switching properties. The simplest member of this family is shown in Figure 1b. The benzene groups can be substituted for five-membered aromatic heterocycles to give another family of photoswitching compound – diarylethenes.

First reported in 1988,[41] diarylethenes exhibit high quantum yields (near 100 %)[42] with very little fatigue[26] and even undergo a photochromic process in the solid-state as single-crystals. Diarylethenes and their derivatives are conjugated with π-delocalisation throughout the molecule, which can be extensively modified with various auxochromes to change the bandgap in which they absorb light, resulting in a spectrum of coloured materials. These molecules isomerise with visible light in the solution-state and the solid-state as single-crystals. The resulting isomer is very thermally stable, so this process is thermally irreversible with the reverse isomerism induced on exposure to UV light.[43]

This solid-state photoswitching is made possible by the mechanism only requiring a minimal structural change with the colourless isomer undergoing a 6π-electrocyclization mechanism with a single bond formed between two aromatic groups to extend the conjugation along the molecule.[44] This is summarised in Figure 3 and shows the photochromism in solution and the solid-state for single-crystals of various diarylethene derivatives.

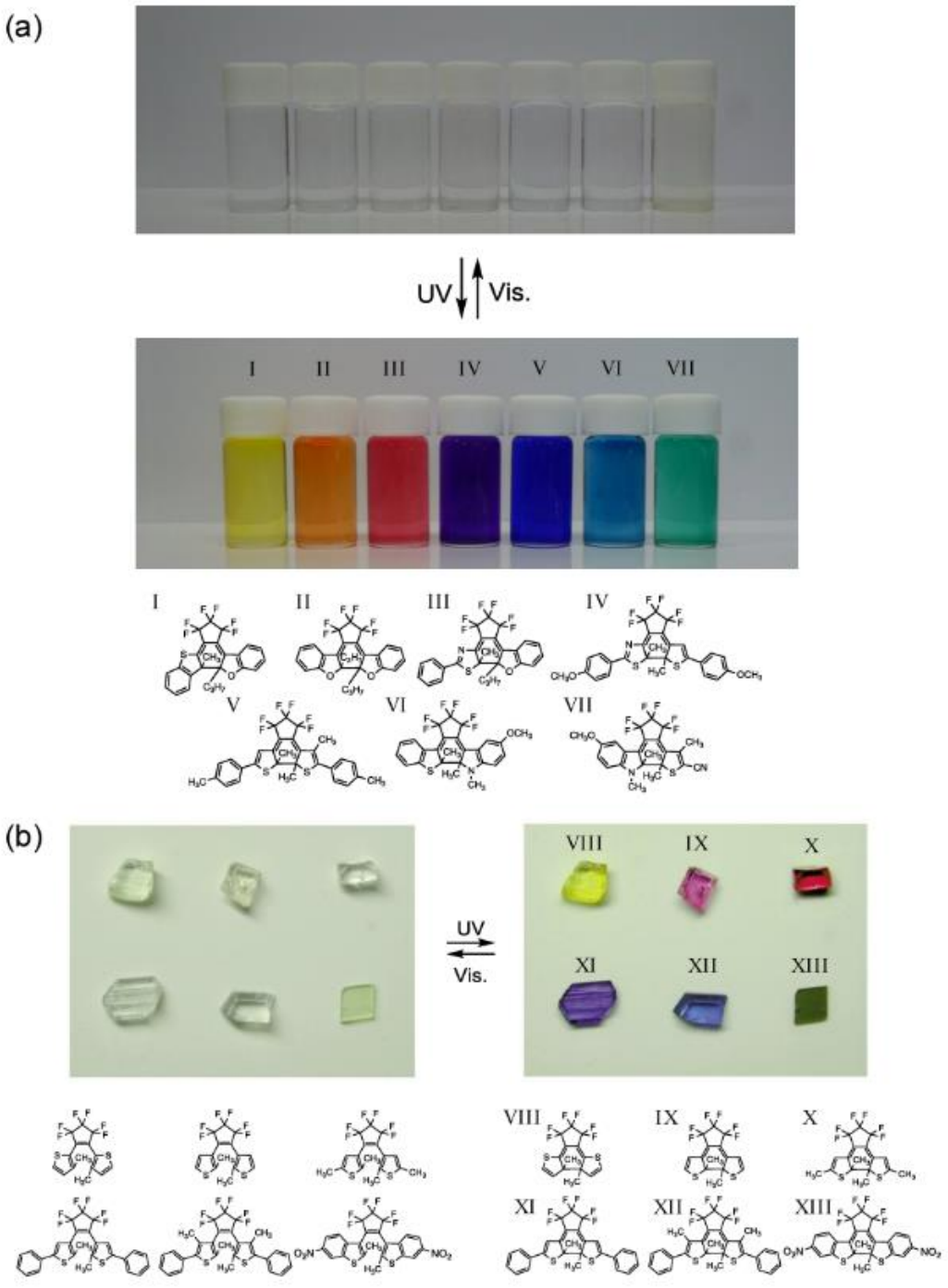

Figure 3. Photochromism of diarylethene derivatives in the a) solution state and b) the solid-state as single-crystals (reproduced from ref. [16] with the permission of the American Chemical Society).

On switching, diarylethenes exhibit a change in many of their physical properties, including colour, electrical conductance, chemical reactivity, and as single-crystals, shape. Potential applications of these highly reversible materials have been numerous due to their stability in the solid-state or as liquid crystals allowing them to be investigated as thin polymer or amorphous films[45–47] and single-crystals for optical memory devices [48,49] and as molecular logic gates in circuitry.[14] They are also easily incorporated into polymer materials either as sidechains or in the polymer's main chain. Using their shape-changing properties allows the production of photo-actuators with the ability to convert light into mechanical motion.[50,51] Like azobenzenes, It is through their ability to switch in the solid-state and be effectively incorporated into polymer systems that these applications have been able to be developed.

1.1.3 Spiropyrans

Spiropyrans are organic photoswitches comprised of an indoline moiety connected to a chromene moiety through a spiro junction,[52] each of which can be extensively modulated to give a large family of compounds. The photo-induced isomerism can be seen in Figure 1c, with the reverse isomerism occurring through thermal processes in the absence of light.[53] Upon irradiation with UV-light or near-infrared (NIR), a ring-opening mechanism is triggered, by the C-O bond cleavage of the spiro-junction, leading to a zwitterionic species. This results in a planar structure with an extended π-conjugated system along the chromene moiety and is the source of the de-cyclised isomers' colour. This reversible process results in the photochromism of the material.[12] The reverse isomerism occurs in the absence of UV light by a ring-closing mechanism with thermodynamic driving forces. This mechanism of switching is summarised in Figure 4.

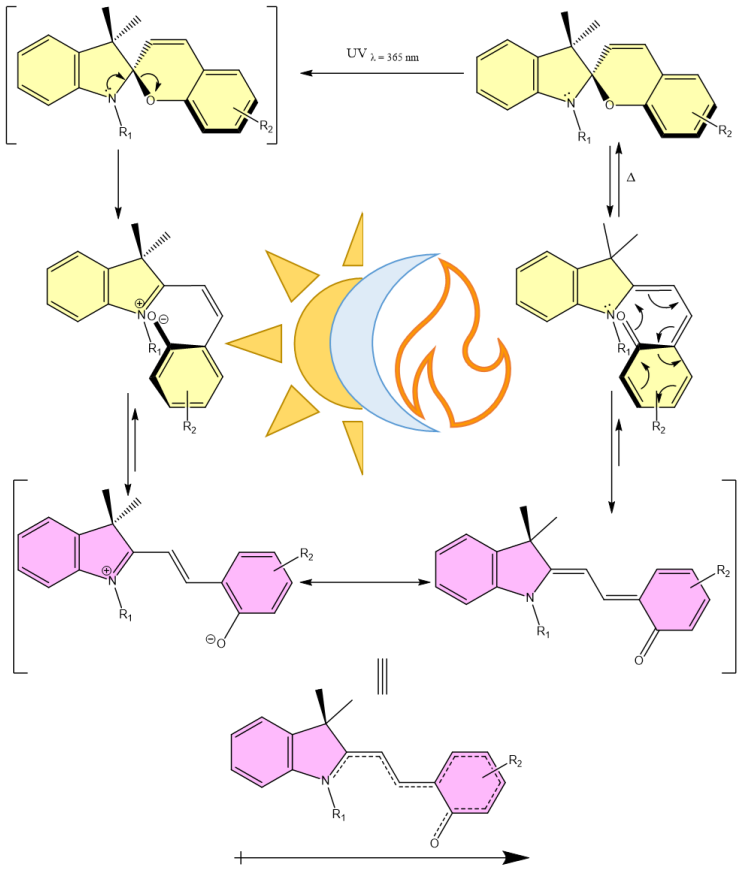

Figure 4. The switching mechanisms of spiropyrans (adapted from ref.[19] with permissions of the Royal Society of Chemistry).

A unique feature of this molecular switch is the resonance form of the de-cyclised isomer. The zwitterionic structure is charged and is more soluble in polar solvents, whilst the form containing the ketone group will favour non-polar solvents. This gives rise to solvatochromism whilst also affecting the reversibility of the materials isomerism.[54] This leads to the fact that spiropyran compounds are multi-responsive, reacting to, as well as light and solvent, changes in Ph (acidochromism), redox potential (electrochromism), metal ions, and even mechanical force (mechanochromism).

Isomerism with mechanical force was observed to be reversible by D. S. Tipikin[55] in 2001 by grinding the material with a mortar and pestle, with melting and local thermochromism ruled out as stimuli. This study was followed by Meng *et al.* in 2015, who performed *in-situ* high-pressure analysis on spiropyran single-crystals to observe the mechanochromism directly.[56] Spiropyrans have been incorporated into polymer backbones, and mechanochromism has been observed upon uniaxial tensile stress, reversible over long periods, Figure 5a.[57] This work was improved by W. Qui *et al.* [58] by comparing different attachment points of the polymer to the spiropyran and characterised by *in-situ*

colour analysis during the mechanical tests along with UV-vis and absorption spectroscopy. It was concluded that the force-induced colour change was dominated by geometric effects with electronic effects being less significant and using DFT calculations, they could optimise the attachment points to best rupture the C-O spiro bond. This means that by using mechanical force, the molecules of spiropyran can be forced to isomerise to the elongated de-cyclised isomer, identifiable by the change in colour, Figure 5b. In all cases, compression of the material was also investigated resulting in isomerism, with the flexibility of the de-cyclised isomer suggested as the reason for this along with the idea that uniaxial compression results in perpendicular tensile stress, Figure 5c, (if you compress it along one direction it expands along the perpendicular directions). Applications of this include visual force/impact sensors such as strain identification in materials for example.

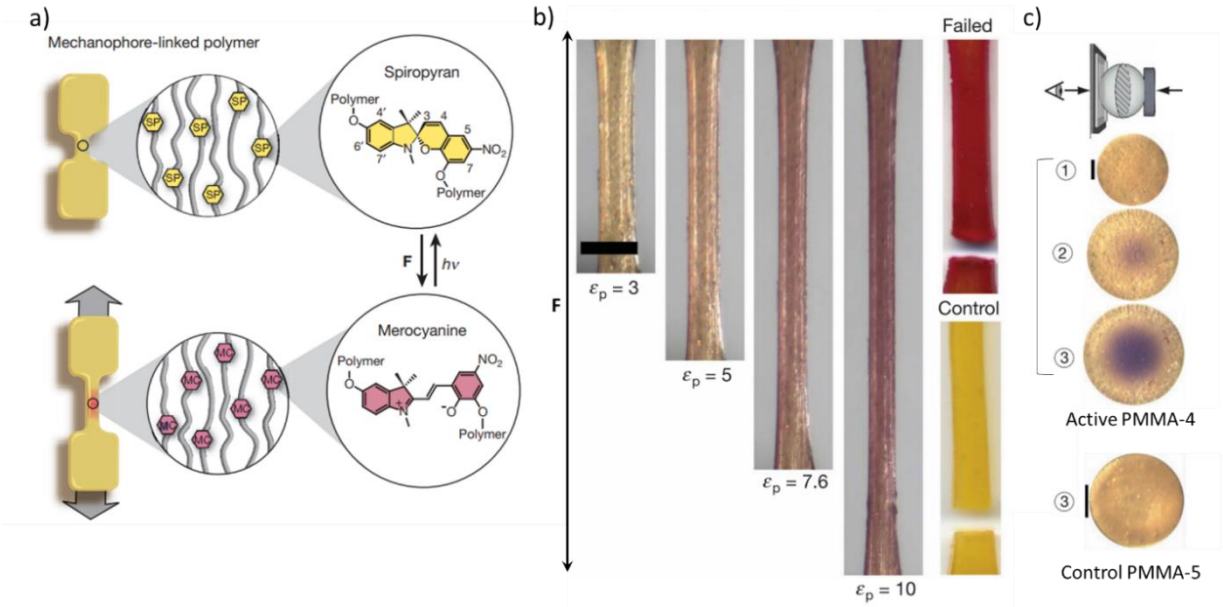

Figure 5. An example of mechanochromic properties showing: a) a schematic of the mechanophore method of action, b) spiropyran-linked PMA elastomer where ε_p is applied tensile stress, with control and failed samples to show the colour change's two extremes, c) spiropyran linked PMMA beads shown over three compression stages (1-3) with a control sample. Scale bar equivalent to 2 mm. (Adapted from ref. [57] *with permission from Springer Nature Publishing).*

The large electric dipole moment of the zwitterionic isomer, measured by density functional theory,[59] not only plays a role in manifesting solvatochromism but also electrochromism and acidochromism. Solvatochromism and acidochromism arise due to the resonance structure of the de-cyclised isomer being zwitterionic and so will have varying stability based on the polarity and acidity of the surrounding solvent.

The work on solid-state photoswitchable polymers is still ongoing, with the most considerable difficulties being the switching times and fatigue resistance. In 2016 a method of encapsulating mixtures of spiropyran photoswitches within vesicles of a polymer matrix was established and allowed for quicker switching times and more fatigue-resistant solid-state materials.[60] This work was carried on by the same group, and they have recently established highly tuneable materials and switch in the solid-state.[61] The materials were tuneable by the interaction of the spiropyrans with surrounding solvent in the vesicles in which they were situated, taking advantage of the materials' solvatochromism but in the solid-state. A limitation of the materials, though, is that only non-volatile solvents can be used. These materials, however, have superior fatigue resistance than previously reported solid-state photochromes, and the tunability means they can potentially make more selective sensors. Examples of the colours achievable, reversibility and visualisation of the vesicles within the polymer matrix are shown in Figure 6.

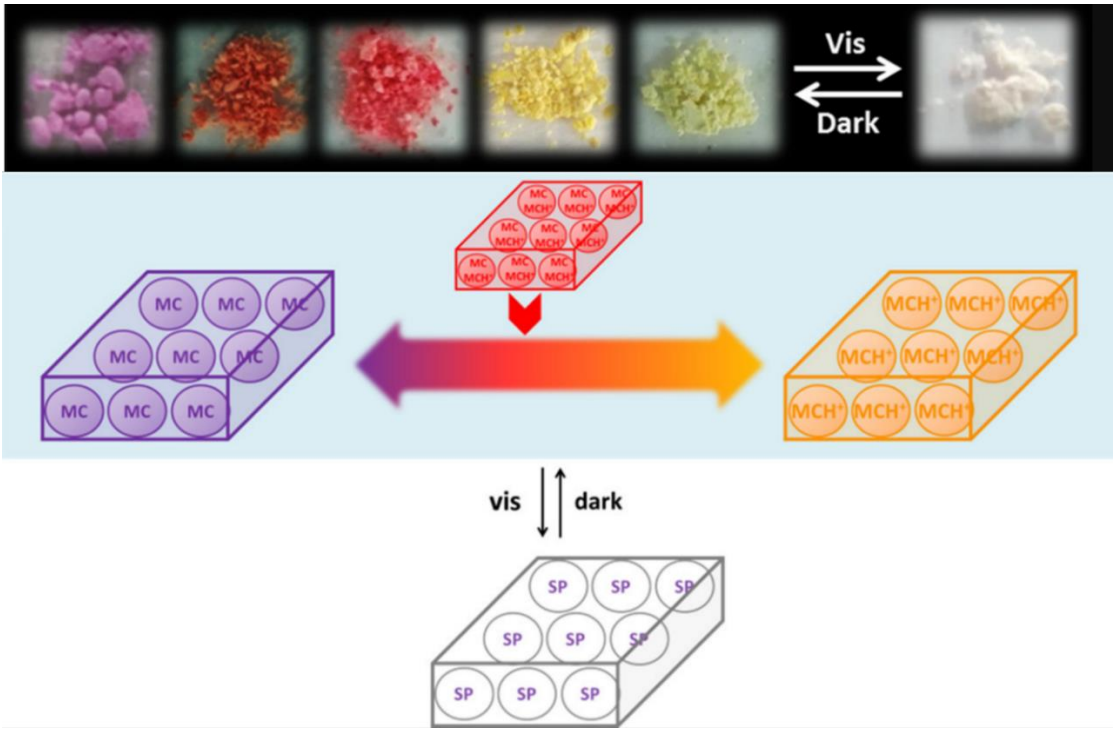

Figure 6. Reversible solid-state photochromism of spiropyran doped polymer matrices by vesicle encapsulation. (Reproduced from ref. [61] with permission the American Chemical Society).

1.2 Molecular Solid-State Transitions

Many materials undergo solid-state transitions of some kind and include colloids, amorphous solids,[62] functionalised polymers, and single-crystals. In the case of single-crystals, there can be either; single-crystal to single-crystal phase transition, or the single-crystal undergoes a phase transition to an amorphous phase, the latter of which is irreversible in respect of reforming crystallinity. Examples of single-crystal to single-crystal transitions include the diarylethene single-crystals previously discussed that retain their single-crystal nature upon photoswitching. The isomerisation causes a change in the unit cell and a change in the crystal's shape and colour. Examples of this are shown in Figure 7a-b. Not only does the colour change in both cases, but the crystal in Figure 7a distorts its shape with angles changing by ± 6°. The rectangular crystal in Figure 7b elongates by 7 %, and both these mechanical effects are induced and reversed using UV light.[63]

Applications of these mechanical effects have been further explored to create systems with more rapid response times, and crystals of rotaxane functionalised ferrocene have been found to exhibit this.[64] This effect can be seen in Figure 7c showing the rapid expansion and contraction of the crystal by two different pathways, one of which is entirely light-based. In this case, the crystals were investigated for use as microswitches in security were using a laser the crystal would expand and complete a circuit (ON) and then contract to break a circuit (OFF). There have also been investigations to look at these systems as microparticle transports. This involves using the crystal's mechanical action, induced by a laser, to transport microparticles, usually silica but sometimes lead testifying crystalline strength.[65] This is also closely related to photoactivation, which these crystals have been explored for too.

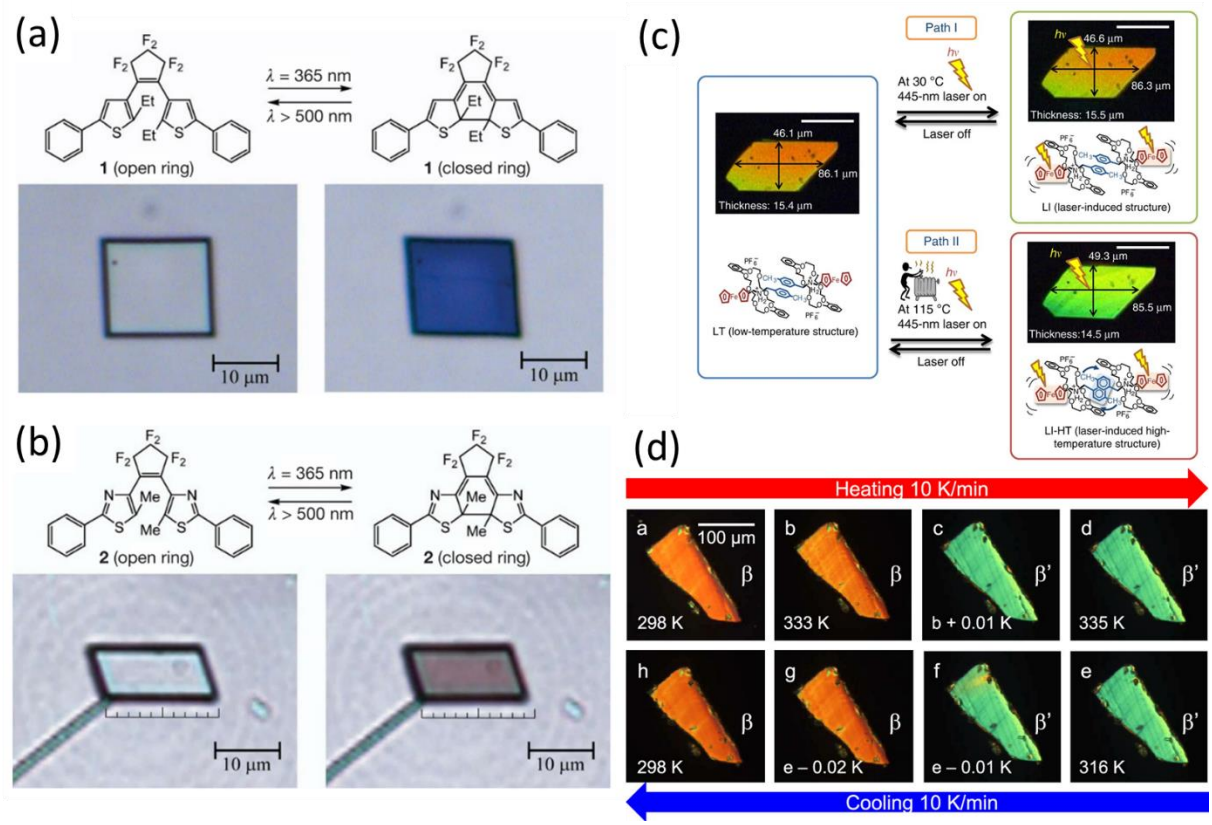

Figure 7. Examples of single-crystal to single-crystal transitions of (a-b) diarylethenes induced by light (adapted from ref. [63] *with the permission of Springer Nature Publishing) c) rotaxane functionalised ferrocene expanding and contracting with visible light. (reproduced from ref.* [64] *with the permission of Springer Nature Publishing) d) thermally induced polymorphism of nifedipine (reproduced from ref.* [66] *with permission from the American Chemical Society).*

In a similar study conducted by G. Yue *et al.,*[66] the solid-state transitions between polymorphs were investigated to yield thermochromic materials. In this case, single-crystals of nifedipine (a nitro-aniline derivative) changed their nitro-torsion angle at different temperatures. This was found to give reversible solid-state transitions and was observable through orange to green colour change. This is shown in Figure 7d with the very abrupt transition occurring with tiny increments of temperature.

Degradation of single-crystals from initiation of a transition is common. Mechanical force, internal stress and pressure from these transitions have been studied for many molecular crystals. For that induced by light is known as the photosalient effect and is observed as crystals rapidly changing shape resulting in jumping or popping on exposure to light.[67–69] Diarylethenes are an example of a molecular photoswitch that exhibit this dramatic property.[70,71] Whilst occasionally reversible if there are single-crystal to single-crystal transitions, it is unsurprising that usually, the crystals break apart.

A recent example of this was explored in the study of single-crystals of vinyl azide.[72] Upon irradiation with UV light, N_2 gas was generated, which increased internal pressure within the crystal. When this pressure is high enough, the crystals fragment and break apart, the process of which was observed to occur along distinct crystallographic faces. This has implications for use as photoactivated mechanical materials by transforming light into mechanical energy.

1.3 Polymorphism of Molecular Solids

From the Latin '*many forms*', polymorphism in molecular solids describes how the same molecular unit can pack together in different ways to produce materials with vastly different properties. Arguably the most famous polymorphic material and an excellent example of polymorphism is 5-methyl-2-[(2-nitrophenyl)amino]-3-thiophenecarbonitrile, nicknamed ROY for the first three polymorphs discovered being red, orange, and yellow. To date, ROY has the largest number of known polymorphs[73] for a given compound, and those that are crystalline come in a range of colours and shapes; these, along with the molecular structure, can be seen in Figure 8.

The polymorphism arises from many functional groups with potential for intermolecular forces, but what gives ROY such variety is the free rotation around the central bond between o-nitroaniline and thiol groups. Deviations in the resulting torsion angle (θ°) between polymorphs gives a range of conformations, increasing the number of combinations in which the molecules can pack together. The torsion angle is also one of the ways colour variations appear by altering the extent of the molecule's conjugation. Other polymorph induced property variations can include melting point, elasticity, solubility, and more. These property variations can have dramatic effects on many chemistry fields, from altering bioavailability for drug molecules to a pigments' lifespan in paints. There are also substantial commercial implications of finding a superior polymorph to an existing patented material that can then be patented as a competitor. [73–78]

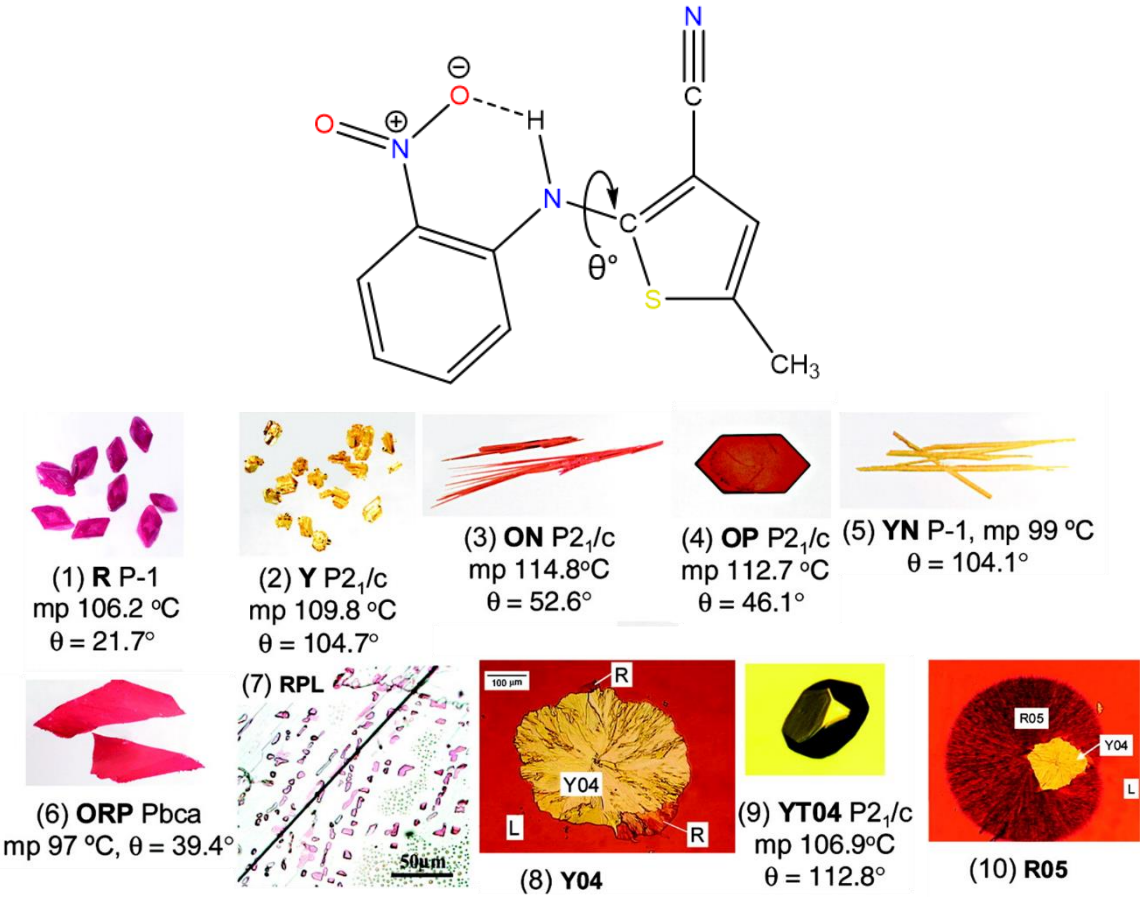

Figure 8. a) Molecular structure of (ROY) with the highlighted torsion angle(ϑ°). b) images of ROY polymorphs (1-10) with respective torsion angle, space group and melting point if known. (Adapted from ref.[78] *with permission from the American Chemical Society).*

1.3.1 Solvatomorphism

ROY represents solvent-free polymorphs, but the presence of different solvents in the molecular crystal can also drastically impact the physical properties of the material. This phenomenon is known as solvatomorphism. This is where solvent molecules are included within the crystal lattice during the crystallisation process, and the chemical composition of the crystal is altered.[79] In changing the composition, the material can then pack in alternative ways. The pharmaceutical industry specifically embraces this area regarding innovative drug patenting, as each solvatomorph is considered unique enough that it needs to be patented itself, even if it isostructural. Crystallising a material from many different solvents can produce solvatomorphs but is not guaranteed.

1.3.2 Hydrogen Bonding

Hydrogen bonding is a specific type of strong dipole-dipole interaction involving a hydrogen atom that is bonded to a strongly electronegative atom.[81] The resulting partial positive charge on the hydrogen can form interactions with partial negative charges within the same or neighbouring molecules.[82] The electrostatic attraction between these partially charged regions, one being the hydrogen-containing donor moiety and the other, usually a Lewis base, acceptor - is a hydrogen bond. Hydrogen bonding plays a crucial role in polymorphism as one of the strongest individual intermolecular interactions.

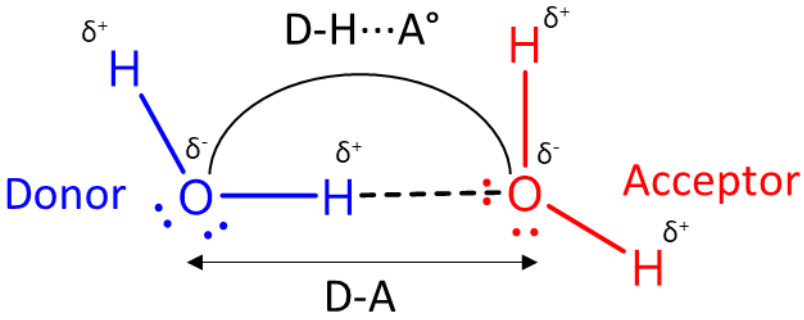

Figure 9. Hydrogen bonding schematic using molecules of water as an example, showing the donor(D) – acceptor(A) distance and bond angle adapted from ref. [80] with permission from John Wiley and Sons using ChemOffice Professional.[21]

Table 1. The comparative strength of hydrogen bonds adapted from ref [80] with permission from John Wiley and Sons.

	Strong	*Moderate*	*Weak*
Type of interaction	*Covalent*	*Mostly electrostatic*	*Electrostatic dispersive*
H···A/ Å	*1.2 – 1.5*	*1.5 – 2.2*	*>2.2*
Donor-Acceptor distance/ Å	*<2.2 – 2.5*	*2.5 – 3.2*	*>3.2*
D-H···A bond angle/ °	*170 – 180*	*>130*	*>90*
Bond energies/ Kcal mol^{-1}	*15 – 40*	*4 – 15*	*<4*

Figure 9 shows a typical hydrogen bond between water molecules, which is the basis for the system presented in Table 1. This is used to categorise and compare the relative strengths of different hydrogen bonds with the bond in Figure 9, corresponding to a hydrogen bond of moderate strength. The shorter the hydrogen bond length, the stronger the interaction. This references the permanence of the dipole between the hydrogen donor and the electronegative acceptor atom of another molecule. The strongest theoretical hydrogen bond has been determined as 82 kJ mol^{-1} with a bond

length of less than 2.5 Å. For context, the hydrogen bond distance between water molecules in single-crystals of ice has been determined as 2.76 Å, and this falls into the moderate category regarding strength. Bond angles for hydrogen bonds tend to the computationally calculated ideal of 177.8° with that constituting optimal orbital overlap generating strong donor-acceptor bonding pairs associated with hydrogen-bonded systems. Bond strength is proportional to donor-acceptor distance as well as the intermolecular bond angle. The bond angle can be influenced by neighbouring electronegative atoms, which can subsequently affect the bond strength.[82–85]

Carbon atoms have been known to act as hydrogen bond donors when bonded to a particularly electronegative element themselves, but there has been contention as to whether this is a formal hydrogen bond or a strong dipole-dipole interaction. An example of a species that forms such interactions is chloroform.[86] The existence of an X-C-H···A bond was proposed initially to account for deviations in the ideal properties of mixtures of chloroform and other organic solvents[87] and initially evidenced through crystallography.[88] This concept became popular in biochemical fields.[89] However, it was still an unpopular concept with crystallographers until recently, where X-C-H···A bonding has become more accepted, through more modern studies, as a weak interaction that can exercise significant influence over crystal packing.[88,90]

1.4 Donor-Acceptor Stenhouse Adducts

Donor-acceptor Stenhouse adducts (DASAs), named for John Stenhouse, having discovered Stenhouse salts in 1850[91] were first reported as photoswitches in 2014.[92,93] These are highly reversible photoswitches and have been the subject of many synthetic and solution state studies.[94,95] A donor amine group and an acceptor group linked by a triene system are produced by a modular two-step synthesis. First, by adding furfural to either a barbituric acid or Meldrum's acid acceptor, an intermediate is produced and synthesis completed by adding a secondary amine via (aza-)Piancatelli rearrangement.[96] This is a quick, simple, high-yielding synthesis allowing DASAs to be efficiently manufactured in large quantities, an essential consideration for potential applications and industrial

scale-up. The secondary amine can either be completely aliphatic, the first-generation DASAs, or contain an aromatic group joined to a cyclised aliphatic amine, the second-generation DASAs.[97] Whilst second-generation DASAs look at modifying the donor group, third-generation DASAs modify the acceptor groups.[98] These concepts are summarised in Figure 10.

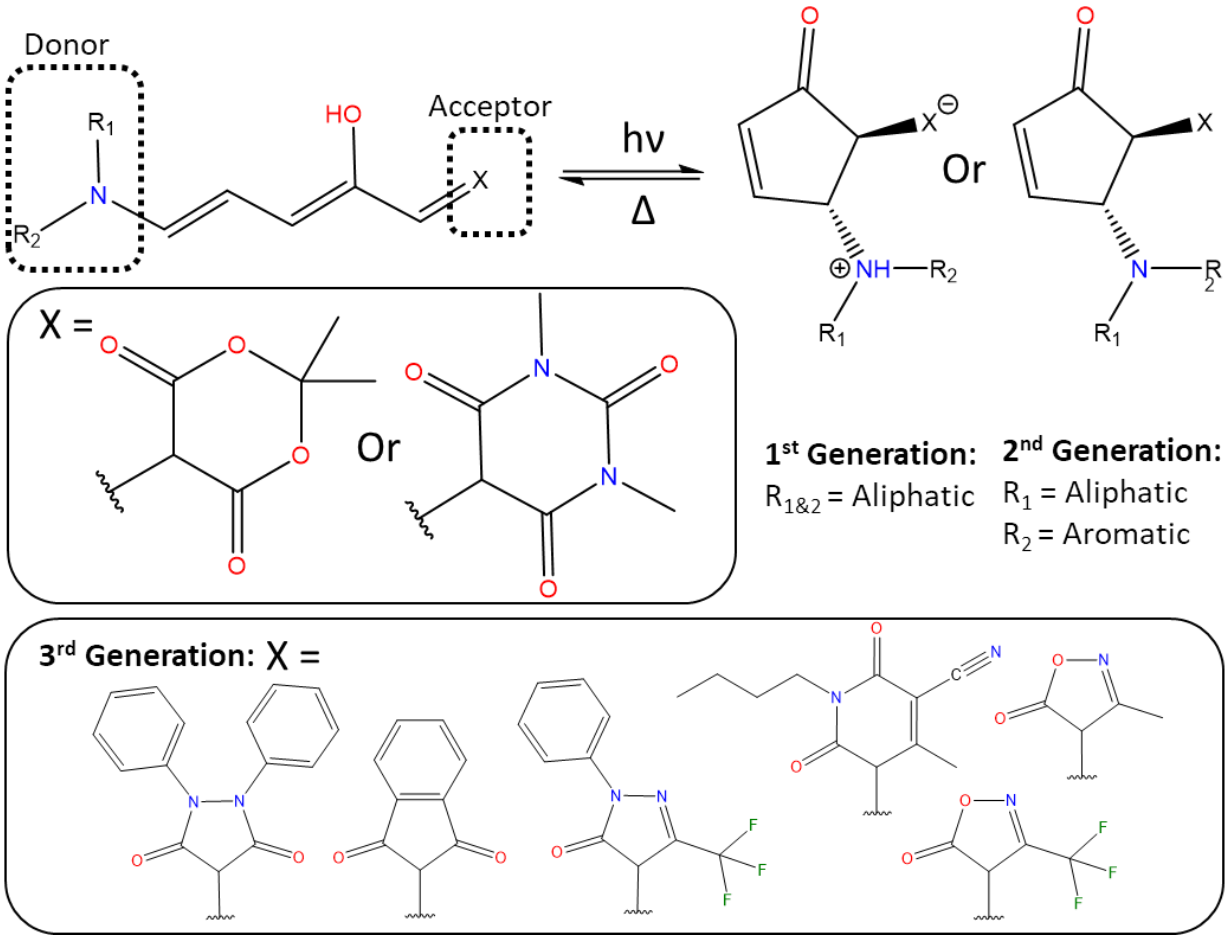

Figure 10. The general structure and isomerism of Donor-Acceptor Stenhouse adducts (DASAs) drawn using ChemOffice Professional.[21]

The photoswitching mechanism of DASAs has only recently been understood. On stimulation with visible light π-π* transitions trigger E/Z isomerism of one of the double bonds along the molecule's triene core, similar to that observed in azobenzenes photoswitches. Through DFT calculations, it has been suggested that the double bond selected for this isomerism is that which is adjacent to the hydroxy group. This importance of the hydroxy group was highlighted by Lerch *et al.* [99] where they used ultra-fast spectroscopy to observe the different stages of isomerism and found that a hydrogen bond between the carbonyl of the acceptor and the hydroxy group stabilises the excited state,

allowing for ring-closing (similar to that in diarylethenes), completed by a proton transfer. This splits the mechanism into multiple steps with light triggering the initial E/Z isomerism but the subsequent 4π-electrocyclization and proton transfer steps being thermally driven, making the latter stages of the isomerism the rate-determining step. The kinetics of the isomerism was investigated extensively by M. Lerch[100] and Di Donato *et al.*[101], with the total mechanism shown in Figure 11.

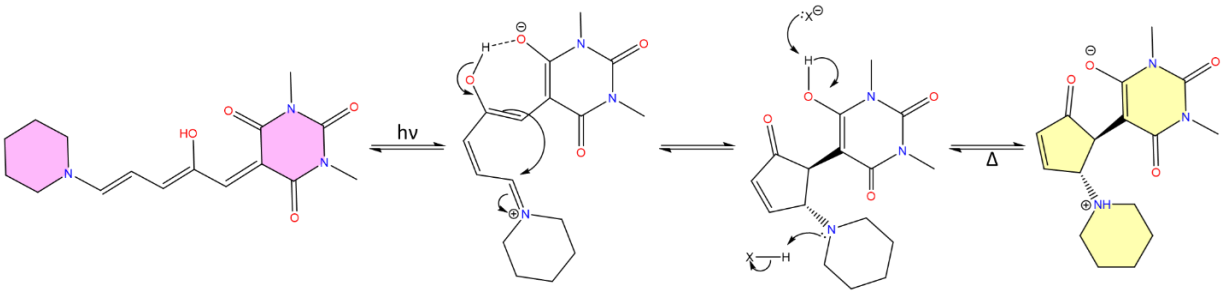

Figure 11. DASA isomerism mechanism using 5-[(2Z,4E)-2-hydroxy-5-(piperidin-1-yl)penta-2,4-dien-1-ylidene]-1,3-dimethyl-1,3-diazinane-2,4,6-trione as an example. (adapted from ref. [99] *with permission from the American Chemistry Society).*

The differences in chemical structure between the two isomers are where their different properties originate. For first-generation DASAs, the linear isomer contains a π-conjugated core that extends conjugation from the donor's nitrogen to the acceptor. This results in the high molar absorptivity values for linear DASAs, with second-generation DASAs having further extended conjugation beyond the donor's nitrogen. On linear-cyclic isomerisation, this conjugation is broken, resulting in the loss of light absorption in the visible wavelengths. Absorption of light is not the only stimulus that can initiate the switching behaviour as these materials are multi-responsive. The materials are thermally active, but the zwitterionic structure of the cyclised first-generation DASAs gives the cyclic isomer a large dipole moment, which leads to solvatochromism too. This zwitterionic structure also results in some degree of acidochromism, but this does deactivate the photoswitching, limiting the property to one-time use applications.[2] In the absence of light, isomerism can still occur by changing the solvent as depicted in Figure 12 or by heating the material.

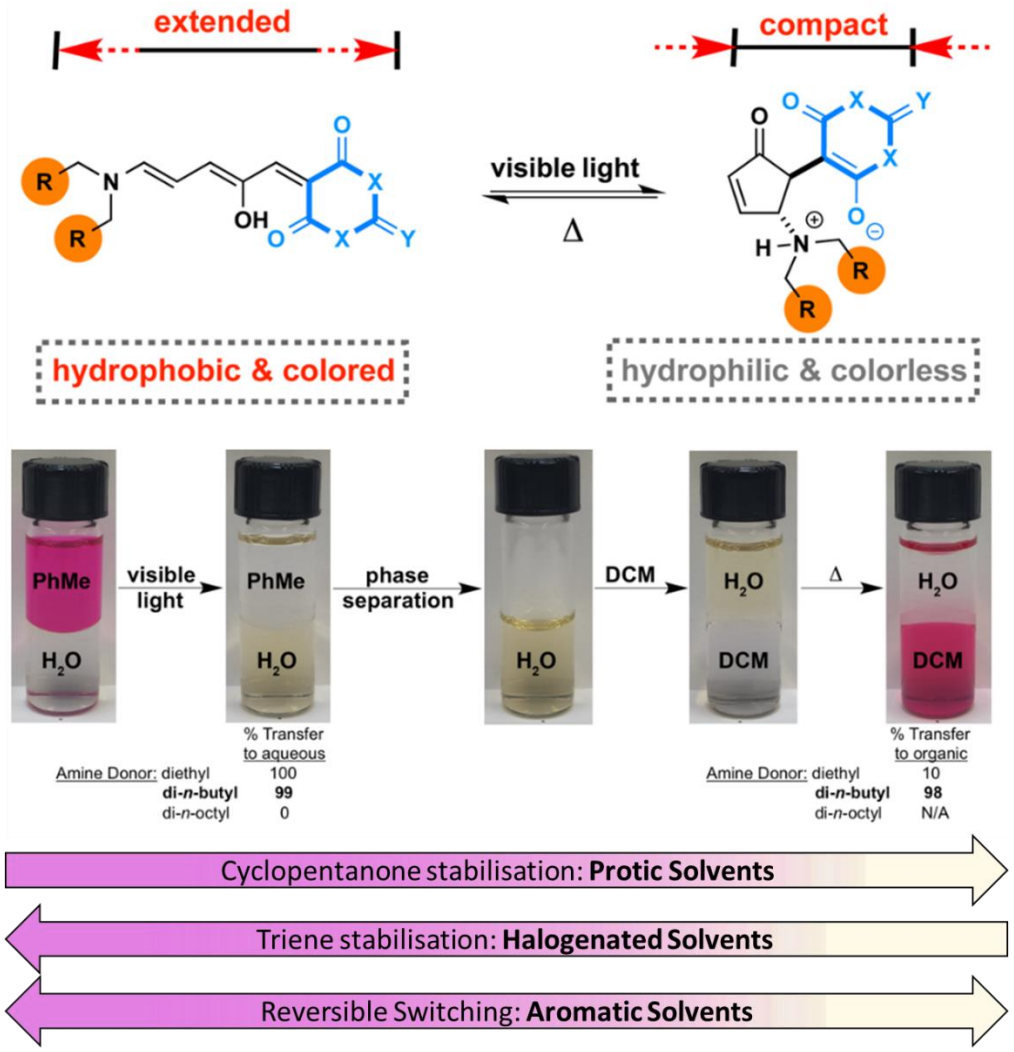

Figure 12. Solvatochromism of first-generation DASAs with physical differences between isomers highlighted (adapted from ref. [93] with permission from the American Chemical Society).

The first-generation DASA isomers' nature means that the solvatochromism disables the photoswitching behaviour with the zwitterionic isomer strongly energetically favoured in polar solvents. The opposite is true for chlorinated solvent, which usually appears coloured due to the very low amount of photoswitching to the colourless cyclopentanone form that occurs, resulting from energy barriers present during the rate-determining 4π-electrocyclization step.[101] Using this, each isomer can be selectively obtained by selecting an appropriate solvent and transitioning between separated solvent phases, as shown in Figure 12. Figure 12 also highlights another feature exhibited by the material on isomerism – a change in molecular length. This property has received significant interest from researchers, particularly in materials science, for their use as sensors or mechanically active materials for soft robotics.[5]

First-generation DASAs have been used as dopants to produce thermal sensor materials, taking advantage of their thermochromic properties. For example, the Hooper group produced a ~3 % DASA doped polyurethane-based elastomer for ballistics applications, specifically identifying micro-explosive projectiles. They tested the material using firearms to penetrate the material resulting in a colourimetric mapping of the projectile's path.[102] In this case, there was no covalent bonding between the polymer or the DASA; the material was a mixture. The colouration was reversible with prolonged exposure to visible light, but this also results in the partial photodegradation of the DASA molecules leading to poor fatigue resistance.

Like spiropyrans and azobenzenes, attempts have been made to incorporate DASAs into polymer systems as side chains. Photopatterning of polycarbonate-based polymers containing covalently bonded first-generation DASAs has been reported, but this was limited to polymer films' surface instead of the bulk material. The switching was also found to be enhanced when the film was undergoing transitions whilst submerged in solvents like ethanol, and so was only the first step to a solid-state DASA switching.[9]

Because of their enhanced switching ability in different environments,[97] second-generation DASA polymers were produced with the DASAs in the bulk of the material instead of just the surface. Ulrich *et al.*[103] used second-generation DASAs with Meldrum's acid acceptor as pendants along both pentafluorophenyl acrylate and methacrylate polymer chains. The absorption tunability of the second-generation DASAs meant that different coloured polymer films were produced by altering the aromatic amine donor. Utilising the wavelength selective switching of the second generation DASAs, Figure 13a-b, mixtures of these different polymers were produced, and wavelength-specific photopatterning achieved, Figure 13c. This photopatterning has also been explored using other photoswitches like azobenzene alongside DASAs to produce multifunctional devices for use as molecular logics that are wavelength specific.[10] Another reason second generation DASAs were used is that first-generation DASAs fail to switch when incorporated as pendants onto the PMA chains.[103]

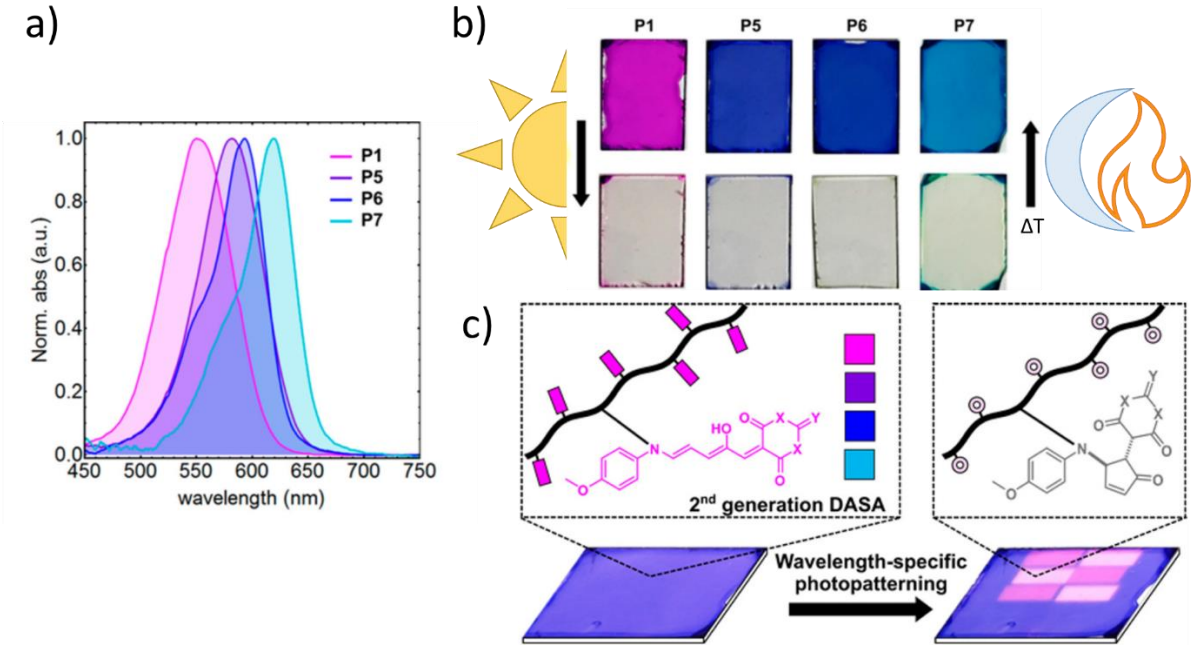

Figure 13. Production of a wavelength-specific photoactive DASA polymer film (adapted from ref.[103] with permission from the American Chemical Society).

Both previously discussed polymers were formed by producing a polymer with the amine in the backbone followed by the addition of the activated furan intermediate to produce the pendants. Alternative approaches place the activated furan intermediate in the polymer backbone and then use this polymer as a chemosensor selective for secondary amines. This means that polymers with covalently bonded first-generation DASAs are possible, with up to 30 % concentrations reported.[104] This has potential applications as food spoilage sensors through the colourimetric detection in protein-based foods[105,106] but also as defined-range thermal sensors as the colourimetric indication is observable by the human eye at high resolutions over tuneable temperature ranges. This method overcomes a limitation of DASA doped polymers, which is that DASAs have a high affinity to aqueous systems and so doped polymers are unfavourable due to leaching. This is overcome, though, by covalently linking the activated furan group to the polymer main chain.

This affinity to water led to Wang *et al.*[107] investigating the photoswitching of DASAs induced by water vapour. They found that using DASAs as inks during this study, reversible linear to cyclic hygrochromism was observed. They supported this finding with DFT calculations and found that co-ordination of water molecules stabilised intermediates, thermodynamically favouring the cyclised

isomer. The group went on to use this orthogonal switching behaviour with light and water vapour to produce a double encryption system for anti-counterfeiting. This used, as well as DASAs, oxazolidines which are positive hygrochromes. With DASAs being negative hygrochromes, this application focuses on the DASAs ability to switch with humidity.[7] Prior to this, in 2018, another group had suggested using spiropyran molecules in a latex matrix for a very similar purpose.[8]

DASAs incorporated into polymers have also been used as sensors to detect nerve agents[108] and metal cations,[109] but these are single-use sensors because the analytes disable the material's reversible isomerism. Drug delivery systems are also being developed by using DASA molecules to form micelles with other lipid-based surfactants.[110,111] This resulted in a liquid crystalline material that allows the encapsulation of drug cargos which can be released on-demand at a target site using visible light. This is a very non-invasive drug delivery system, and using visible light is a benefit over higher energy UV radiation, associated with other molecular photoswitches, which is known to damage biological systems.

One of the significant benefits of DASAs is that they are negatively photochromic and so can have high conversion efficiencies. When the DASA isomerises from the linear triene form to the cyclised cyclopentanone form, it no longer absorbs the exciting light which is then transmitted into the bulk of the material until it has completely switched. [12,112] The main limitation of DASAs is that they perform best in the solution-state at lower concentrations, but most applications require either high concentration solutions or preferably solid-state photoswitching.[112] Studying DASA single-crystals also offers the opportunity to carry out detailed mechanistic analysis of the switching if they undergo single-crystal to single-crystal transitions.

The switching of multi-responsive DASA materials has not previously been reported in the solid-state for any DASA, with solution-state studies dominating the literature.[94] Composite materials containing first-generation DASAs often fail to switch entirely after the first cycle, which has been attributed to either degradation or trapping of the dopant DASA molecules in the zwitterionic state resulting in

discontinuation in molecular motility.[92,103] By contrast, the thermally induced solid-state switching of 5-[(2Z,4E)-2-hydroxy-5-(piperidin-1-yl)penta-2,4-dien-1-ylidene]-1,3-dimethyl-1,3-diazinane-2,4,6-trione (**D1**) was first observed qualitatively by S. W. Connolly, as described in their Master's thesis;[113] and this work seeks to investigate and understand this switching process and how it is affected by solvatomorphism. This has been done using X-ray diffraction and other characterisation methods, including thermogravimetric analysis (TGA), differential scanning calorimetry (DSC) and variable temperature reflectivity measurements for quantification of colour change during the switching process.

2 Experimental

2.1 Synthetic procedure

The synthesis starts with the preparation of 5-[(cyclopenta-1,3-dien-1-yl)methylidene]-1,3-dimethyl-1,3-diazinane-2,4,6-trione (**INT1**) as described by Helmy *et al*.[92] and is displayed in Figure 14. The DASA was prepared from barbituric acid (4.68 g, 30 mmol) dissolved in 100 mL of water. Furfural (2485 µL, 30 mmol) was added and stirred for 2 hours at room temperature (~25 °C). The resulting precipitate was dissolved in dichloromethane (DCM) and consecutively washed with water and saturated aqueous: $NaHSO_3$, $NaHCO_3$, and NaCl solutions. After drying with $MgSO_4$, crude **INT1** was then collected by removing DCM via rotary evaporation and purified by recrystallization from hexane to yield the bright yellow needle crystals of the intermediate (5.38 g, 23 mmol, 76.5 %). Samples of **INT1** in deuterated chloroform were analysed by ^{1}H-NMR and matched to those previously published,[92] details can be found in Figure B of the Appendix along with a PXRD pattern in Figure C.

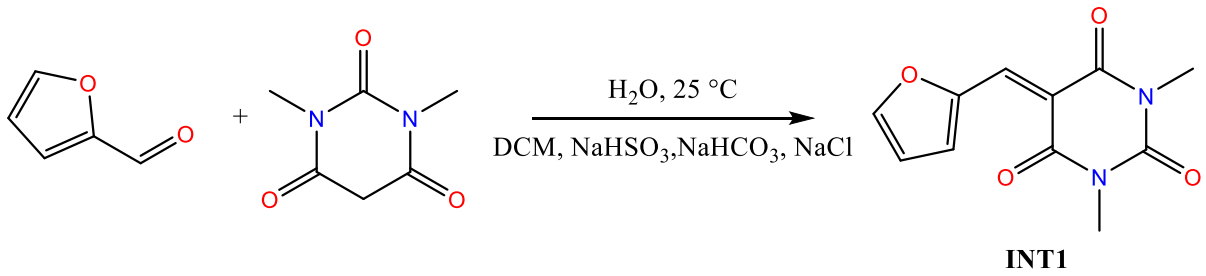

Figure 14. The reaction scheme, depicting the synthetic procedure for 5-[(cyclopenta-1,3-dien-1-yl)methylidene]-1,3-dimethyl-1,3-diazinane-2,4,6-trione (INT1).

The final product 5-[(2Z,4E)-2-hydroxy-5-(piperidin-1-yl)penta-2,4-dien-1-ylidene]-1,3-dimethyl-1,3-diazinane-2,4,6-trione (**D1**) was prepared as described by Mallo *et al.*[95] and S. W. Connolly[113] and is displayed in Figure 15. **INT1** (3.00 g, 12.8 mmol) is dissolved in THF (200 mL) and stirred at room temperature (~25 °C). Piperidine >99% (1265 µL, 12.8 mmol) was added and stirred for 1- 2 hours and cooled in the freezer for 12 hours. The resulting precipitate was collected via vacuum filtration and washed with diethyl ether (~5 mL) to yield a bright pink powder when dried (2.706 g, 8.5 mmol, 66.4 %). Samples of **D1** in deuterated DCM were analysed by ^{1}H-NMR and matched to those previously published,[95] details can be found in Figure D of the Appendix.

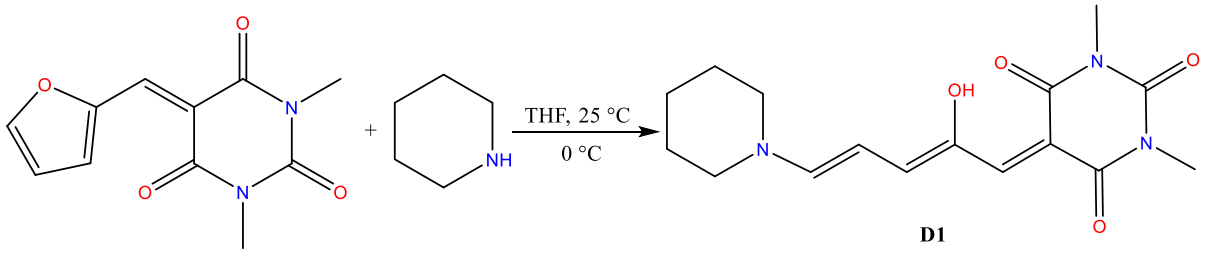

*Figure 15. The reaction scheme depicting the synthetic procedure of 5-[(2Z,4E)-2-hydroxy-5-(piperidin-1-yl)penta-2,4-dien-1-ylidene]-1,3-dimethyl-1,3-diazinane-2,4,6-trione (**D1**).*

2.2 Crystallisation single solvent screening

Freshly synthesised **D1** is added to the solvent (3 mL) until saturation is reached. The resulting mixture is sonicated for 1 minute and then heated to below the solvent boiling point to maximize the sample's dissolution. The solution is then filtered through glass wool into three glass vials and capped with a plastic lid with a small hole in the centre. These were then arranged in a polystyrene sample holder, as per Figure 16, to prevent sudden thermal changes and left at ambient light, temperature, pressure and humidity — the crystals formed by the slow evaporation of the solvent.[114]

Methanol A [1]	Methanol B [2]	Methanol C [3]	THF A [4]	THF B [5]	THF C [6]	DCM A [7]	DCM B [8]	DCM C [9]
Chloroform A [10]	Chloroform B [11]	Chloroform C [12]	Water A [13]	Water B [14]	Water C [15]	Diethyl Ether A [16]	Diethyl Ether B [17]	Diethyl Ether C [18]
Ethanol A [19]	Ethanol B [20]	Ethanol C [21]	Toluene A [22]	Toluene B [23]	Toluene C [24]	DMSO A [25]	DMSO B [26]	DMSO C [27]
Acetonitrile A [28]	Acetonitrile B [29]	Acetonitrile C [30]	Hexane A [31]	Hexane B [32]	Hexane C [33]	Benzene A [34]	Benzene B [35]	Benzene C [36]
Acetone A [37]	Acetone B [38]	Acetone C [39]	Ethyl Acetate A [40]	Ethyl Acetate B [41]	Ethyl Acetate C [42]	DMF A [43]	DMF B [44]	DMF C [45]
Chlorobenzene A [46]	Chlorobenzene B [47]	Chlorobenzene C [48]	Petroleum Ether A [49]	Petroleum Ether B [50]	Petroleum Ether C [51]	Bromobenzene A [52]	Bromobenzene B [53]	Bromobenzene C [54]
Amonium Hydroxide A [55]	Amonium Hydroxide B [56]	Amonium Hydroxide C [57]						

Figure 16. Crystallisation solvent screen map, solvent, vial identifier, position in the sample holder.

Of the 19 solvents screened, two solvents were immediately abandoned due to poor solubility of **D1**, hexane and petroleum ether. Of those remaining, **D1** was highly soluble in halogenated solvents along with polar solvents such as water, alcohols, and amines, in-line with literature findings.[95]

The samples crystallised from methanol, water, DCM and chloroform were characterised by reflectivity, thermogravimetric analysis (TGA) with simultaneous differential scanning calorimetry (DSC), single-crystal X-ray diffraction (SCXRD) and powder X-ray diffraction (PXRD).

2.3 Reflectivity

Sample preparation involved isolation of crystal samples and either grinding using an agate pestle and mortar or crushing single-crystals between two glass slides. The colour of an opaque solid sample arises from the absorption of light by the material. The reflectance (the light not absorbed) can be measured by means of the following set-up. This strategy assumes no emission in the visible region, fluorescence or phosphorescence and that no colour arises from structural means by way of diffraction, refraction, or scattering. These are reasonable assumptions due to the nature of the sample being completely organic, highly conjugated small molecules.

Using a hyper-lapse camera with a 30 FPS frame rate, measurements of reflected light from the sample were collected. This was conducted in a light box coated in a blackout cover, and an LED D65 sample illuminant. Using the light box removes any external stray light from reflecting off the sample. The Linkam THMS600 heating stage, with an optically transparent quartz window, connected to a T96 system controller with Linkpad and a liquid nitrogen pump, was used to conduct variable temperature measurements and was set up within the light box. Heating rates of 5 °C min^{-1} were typically used with any deviations to this later specified.

Using the heating rate and frame rate, digital image processing with ImageJ[115] was used to individually segment the frames from the video and match each frame to the sample's temperature. Each frame was converted to grayscale and the average pixel intensity for each frame calculated for a defined region of interest (ROI). A background ROI was also measured and, when required, deducted from the sample values to remove background fluctuations associated with any stray light and camera focus or white balance adjustments. Further information on this process can be found in the Appendix, described in Figure A and by Equation A. Percentage average pixel intensities were then plotted against each frame's temperature to produce a characteristic curve for the sample's thermochromic property. By using median average pixel intensities, outlier reflectance values from light scattering (gloss) were given less weighting than mean average intensities.

2.4 Thermogravimetric analysis & differential scanning calorimetry

Thermogravimetric analysis (TGA) and differential scanning calorimetry (DSC) was conducted on most isolated solvatomorphs using the Netzsch-Gerätebau GmbH - STA 409 PC Luxx Simultaneous thermal analyser. Samples were weighed into aluminium crucibles on the milligram scale. The measurements were taken under a 30 mL/min flow rate of 80/20 nitrogen/oxygen air between 30 °C- 400 °C with a ramping rate of 10 K/min. A reference crucible and background correction were applied to ensure all measurements were attributed to the samples' behaviour and not environmental factors.

2.5 SCXRD

Single-crystal X-ray diffraction (SCXRD) allows detailed analysis of the DASA in the solid-state, including bonding within the molecule and crystal packing, including supramolecular interactions between molecules and with solvent molecules. This method is also used to investigate and explore intermolecular interactions and geometries to understand how these effects impact macroscopic sample properties by looking at how the material self-assembles in the solid-state. How these properties change under varying thermal conditions will help understand solid-state switching. A limitation of SCXRD is that it only gives a characterisation of a single-crystal from a larger bulk sample, but phase purity can be determined by comparing powder X-ray diffraction (PXRD) patterns with the single-crystal data.

Single-crystals underwent structural analysis by single-crystal X-ray diffraction (SCXRD) techniques using the Rigaku Oxford Diffraction dual-source SuperNova, equipped with an Atlas S2 CCD detector. A micro-focus sealed X-ray tube was the source of copper K_α radiation with a wavelength of 1.54184 Å, focused using multi-layered optics. Samples were mounted onto MiTeGen micro-loops in oil or affixed to glass fibres with nail polish (Boots UK Limited, PONCHO PINK), and analysis carried out at a range of temperatures. Temperature control was achieved using an Oxford cryostream, using a flow of dry nitrogen over the sample. After collection, data reduction, absorption adjustments and finalisation were made using CrysAlisPro[116] and solved using direct methods in Olex2[117] with SHELXS and least-squares refinements carried out using SHELXL[118]. Non-hydrogen atoms were refined anisotropically, and hydrogen atom positions geometrically located and set as riding their parent atom. Where necessary, the solvent disorder was modelled by splitting the occupancy of atoms across two crystallographically distinct environments; EADP and SADI commands were used to ensure stability of the refinement while refining the relative occupancies.

2.6 PXRD

Powder X-ray diffraction was performed using the Rigaku Miniflex benchtop X-ray powder diffractometer. Samples were crushed with glass slides or ground with an agate pestle and mortar and pressed flat onto silica sample mounts. Diffraction of Cu K_α radiation was collected within a 2θ range of 5° to 40° with the sample holder spinning.

2.7 Hirshfeld Surface analysis

By means of computationally generated surfaces, intermolecular contacts can be determined based on contact length. These surfaces are computationally straightforward to produce using CrystalExplorer[119] that utilises the TONTO computational chemistry package.[120] First developed by M. Spackman *et al.* in 1997,[121] the method uses Fred Hirshfeld's stock-holder partitioning method,[122] which was initially a quantitative description of molecular charge distribution, allowing for the calculation of inter/intra molecular electrostatic potentials or interaction energies. M. Spackman applies this to crystal structure models by dividing the crystalline electron distribution into molecular fragments resulting in smooth surfaces that surround individual molecules, whilst also defining areas of low electron density as voids.[123,124] The surfaces, once produced, can be used as a visualisation tool with different properties mapped onto the surfaces with a focus on inter/intra contact distance from parts of the molecule to the surface.[125] Using this technique, all intermolecular interactions can be summarised and compared to identify all interactions that play a role in the crystal packing. Hirshfeld surfaces are generated from a .cif file and are dependent on the quality of the crystal data.

2.7.1 Surfaces

The d_e (external distance) surface maps the distance between external nuclei and the surface, using colour to convey intensity. The d_i (internal distance) surface is the same, except it maps the distance between the internal nuclei and the surface.[125]

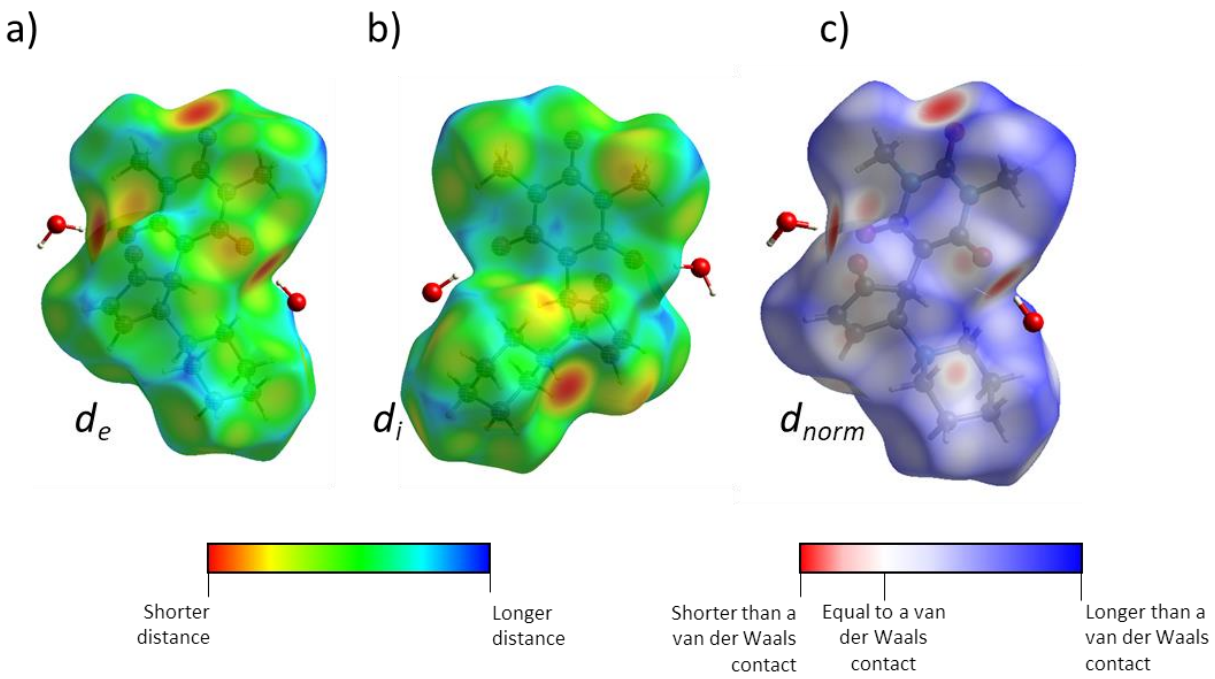

*Figure 17. An example surface, using (**D1·1.5H₂O**), and accompanying keys with a) d_e, b) d_i, and c) d_{norm} mapped onto the surface.*

The d_e and d_i surfaces can be modelled independently to show which parts of the molecules accept the contact and the origins of the donating region of the molecule. The visible spectrum is used to convey regional information regarding $d_{e/I}$ distance. In Figure 17a, the surface's red regions are centred on oxygen atoms in the barbituric acid ring. For a d_e surface, this indicates proximity to external nuclei, in this case, hydrogen atoms, and so shows that each of these highlighted oxygens are each acting as hydrogen bond acceptors in some capacity. Conversely, in Figure 17b, the d_i surface highlights the amine cation, which, in a d_i surface, indicates proximity to an internal atom, suggesting that this is a hydrogen donor. The red regions suggest these interactions are the shortest intermolecular contacts suggesting these likely govern this molecule's packing. This specific example is explored later in section 3.1.3 using SCXRD analysis with the use of Hirshfeld surfaces used to identify all other intermolecular contacts involved in the packing of the crystal. There are orange/yellow regions on both surfaces, suggesting more extended contacts than a hydrogen bond but a shorter contact than a dispersive interaction.

Figure 17c is a d_{norm} (normalised distance) surface and is the sum of the normalised d_e and d_i surfaces, where each is normalised by the van der Waals radius involved. Mapping this property onto the surfaces in place of $d_{e/I}$ overcomes the limitation that relative atom sizes are not well accounted for, so interactions between larger atoms are not effectively highlighted on individual d_e and d_i surfaces. The d_{norm} surfaces are the ones that will be used in the analysis of crystal packing to look at non-hydrogen bonding interactions. The colour of this surface shows the length of the intermolecular contact relative to a van der Waals interaction, as seen by the key in Figure 17c.[125]

2.7.2 Fingerprint plots

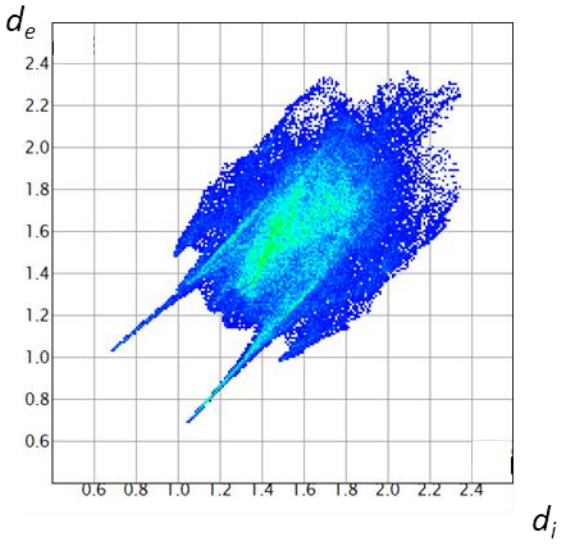

*Figure 18. An example of a fingerprint plot generated from the d_{norm} surface of (**D1·1.5H₂O**).*

From a d_{norm} surface, two-dimensional plots can summarise the surface by plotting d_i vs d_e. This summary encapsulates all possible intermolecular interactions and the significance of these interactions interpreted by each fingerprint plot's unique morphology. [126,127]

Figure 18 shows such a plot. The shorter d_i and d_e are, the closer the internal and external nuclei are to each other; on a plot, features closer to the origin indicate shorter interatomic contacts. Interpreted as intermolecular distance, this can be indicative of intermolecular forces, which is significant when trying to understand structurally derived properties. The sharp 'wings' of the plot arise from significantly interactive forces such as the hydrogen bonding in the system. The centre of the plot

shows dispersive interactions characteristic of van der Waals forces, usually observed through H-H contacts. The plots' regional colours can be crudely described as the frequencies of these interactions, and as these are reasonably uniform across the plot, the varying combinations of d_e and d_i must also occur at similar frequencies.

A numerical value could then be calculated to summarise the overall proportion of each contact type, indicating which could be the dominating effect. This specific example is discussed further in section 3.1.3.

2.8 Melting point analysis

Powdered samples of D1.H_2O were packed into a glass capillary tube with one end sealed. These samples were then heated at a ramping temperature of 0.5 °C/min, and the clear point values were recorded.

2.9 ^{1}H-NMR

^{1}H-NMR spectroscopy was performed using the Bruker AV2 400 MHz spectrometer with samples dissolved in deuterated solvents. Using ACD Labs software,[128] the chemical shifts in ppm were calibrated to the centre of the solvent peaks[129] and assigned to the relevant proton environments.

3 Results and Discussion

Four different crystalline phases have been isolated: a water solvate (**D1·1.5H_2O**), an unsolvated **D1** obtained after recrystallisation from methanol (**D1·unsolv**), a dichloromethane solvate (**D1·1.5DCM**) and a chloroform solvate (**D1·$CHCl_3$**), using the procedure described in the experimental section. All crystals are colourless, of various block shapes and varying sizes. In Figure 19, images of a representative example of each solvate and its respective asymmetric unit can be observed. SCXRD structures of the four samples are shown in Figure 19, and crystallographic parameters for data collections at 150 K are presented in Table 2.

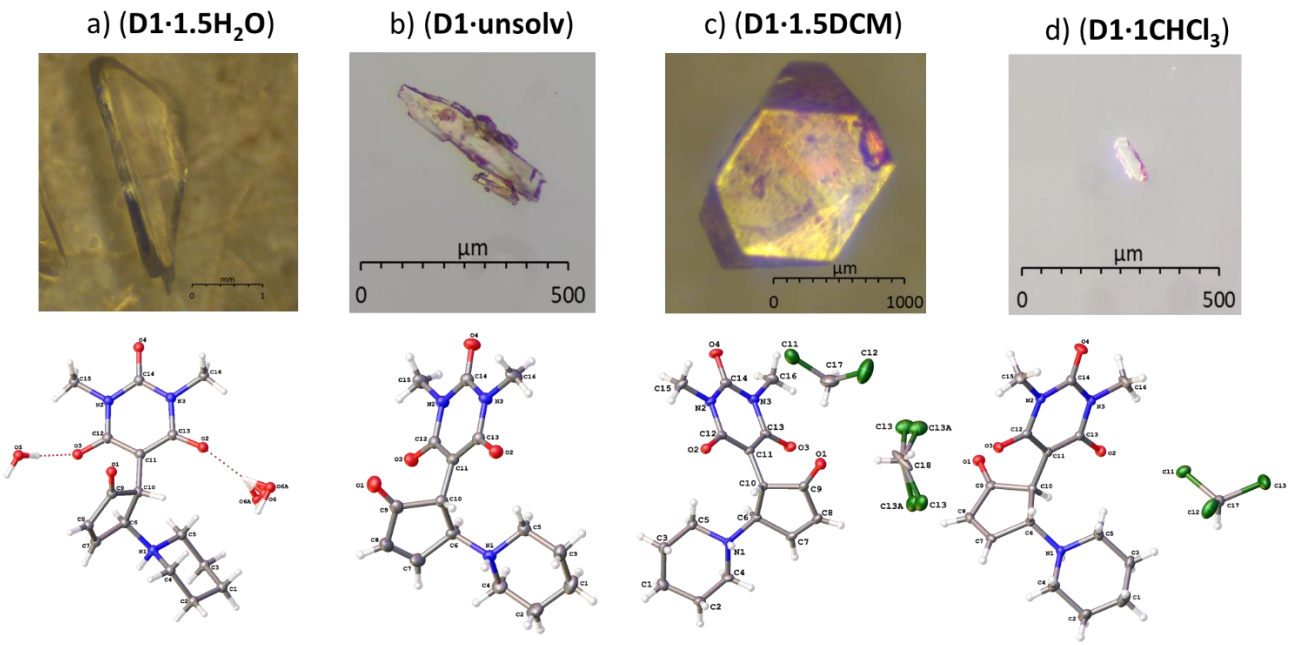

*Figure 19. Images of crystallised **D1** asymmetric units, crystallised from: (a) H_2O, (b) MeOH, (c) DCM and (d) $CHCl_3$*

Table 2. Structure refinement details from single-crystal X-ray diffraction for each of the four isolated solvatomorphs

Identification code	(D1·1.5H$_2$O)	(D1·unsolv)	(D1·1.5DCM)	(D1·CHCl$_3$)
Empirical formula	$C_{16}H_{24}N_3O_{5.5}$	$C_{16}H_{21}N_3O_4$	$C_{17.5}H_{24}Cl_3N_3O_4$	$C_{17}H_{22}Cl_3N_3O_4$
Formula weight	346.38	319.36	446.75	438.72
Temperature/k	150(1)	150(1)	150(1)	150(1)
Crystal system	monoclinic	monoclinic	monoclinic	triclinic
Space group	C2/c	P2$_1$/n	C2/c	P-1
a/Å	21.30932(19)	10.2539(3)	18.4119(4)	10.3622(7)
b/Å	13.76512(12)	13.8928(3)	10.4172(2)	10.3852(6)
c/Å	11.50918(12)	11.9994(4)	21.8817(6)	10.6390(6)
α/°	90	90	90	63.752(6)
β/°	99.0903(9)	114.639(4)	98.928(2)	70.317(6)
γ/°	90	90	90	76.982(5)
Volume/Å^3	3333.54(5)	1553.75(10)	4146.07(17)	962.89(12)
Z	8	4	8	2
P_{calc} /g cm^{-3}	1.380	1.365	1.431	1.513
M/mm^{-1}	0.875	0.821	4.253	4.569
F(000)	1480.0	680.0	1864.0	456.0
Crystal size/mm^3	0.446 × 0.307 × 0.13	0.12 × 0.083 × 0.045	0.123 × 0.08 × 0.056	0.12 × 0.096 × 0.054
Radiation/ Å	Cu Kα (λ = 1.54184)	Cu Kα (λ = 1.54184)	Cu Kα (λ = 1.54184)	Cu Kα (λ = 1.54184)
2θ range/°	7.674 to 142.56	9.574 to 143.686	8.18 to 143.902	9.102 to 143.56
Index ranges	-26 ≤ h ≤ 25, -16 ≤ k ≤ 16, -12 ≤ l ≤ 13	-12 ≤ h ≤ 11, -15 ≤ k ≤ 17, -12 ≤ l ≤ 14	-22 ≤ h ≤ 22, -12 ≤ k ≤ 12, -26 ≤ l ≤ 25	-12 ≤ h ≤ 12, -11 ≤ k ≤ 12, -13 ≤ l ≤ 9
Reflections collected	15693	11066	19959	7187
Independent reflections	3208 [R_{int} = 0.0215, R_{sigma} = 0.0128]	3024 [R_{int} = 0.0261, R_{sigma} = 0.0224]	4026 [R_{int} = 0.0435, R_{sigma} = 0.0275]	3674 [R_{int} = 0.0216, R_{sigma} = 0.0309]
Data/restraints/parameters	3208/0/318	3024/0/292	4026/20/377	3674/0/340
Goodness-of-fit on F^2	1.029	1.049	1.082	1.033
Final R indexes [i>=2σ (i)]	R_1 = 0.0323, wR_2 = 0.0833	R_1 = 0.0354, wR_2 = 0.0909	R_1 = 0.0470, wR_2 = 0.1263	R_1 = 0.0303, wR_2 = 0.0750
Final R indexes [all data]	R_1 = 0.0336, wR_2 = 0.0847	R_1 = 0.0404, wR_2 = 0.0953	R_1 = 0.0535, wR_2 = 0.1304	R_1 = 0.0375, wR_2 = 0.0787
Largest diff. Peak/hole / e Å^{-3}	0.28/-0.34	0.24/-0.22	0.35/-0.46	0.25/-0.27

DASAs with barbituric acid groups - such as **D1** - have multiple hydrogen-bond donors and acceptor functionalities present in the linear and cyclised form. Because of this, they have been known to have their switching properties in solution governed by intermolecular interactions with solvent molecules, so it is no surprise that this leads to the likely stability of multiple crystal solvates.[130] This, coupled with the cyclised isomer's zwitterionic structure, grants the potential for multitudes of intermolecular interactions and forms of crystal packing, leading to the abundance of solvatomorphism observed. Detailed analysis of crystal packing allows the development of structure-property correlations between the different solvates. As all four solvates contain **D1**, differences in their properties must be a result of differences in their solvation and crystal packing. This crystal packing is a result of the shape and size of the molecule as well as intermolecular interactions between molecules.

(**D1·1.5H_2O**) was crystallised in the space group *C2/c*, with 1.5 molecules of water per **D1** molecule. Hydrogen bonding between the barbituric acid group and two crystallographically distinct water molecules are the most substantial intermolecular interactions present; a more detailed structural analysis of this and all other solvates is provided later in section 3.1.

(**D1·unsolv**) was crystallised with a monoclinic unit cell in the space group $P2_1/n$ without any solvent present in the crystal structure. The molecules pack as dimers where hydrogen bonding again features as the most significant intermolecular interactions. This is explored in section 3.2.

(**D1·1.5DCM**) was crystallised in the space group *C2/c* with 1.5 DCM per **D1** molecule. The crystals are unstable and spontaneously disintegrate, crack, and change from colourless to purple on removal from the mother liquor at ambient temperature. Hydrogen bonding plays an important role still in this crystal structure, with the **D1** molecules packing together as dimers, as described in detail in section 3.3.

(**D1·$CHCl_3$**) was crystallised in the space group *P-1* with one $CHCl_3$ per **D1** molecule. There are, on average, two asymmetric units per triclinic unit cell. The crystals are unstable and spontaneously crack,

disintegrate, and change from colourless to purple on removal from the mother liquor. The molecules again form hydrogen-bonded dimers. This is described further in section 3.4.

The macroscopic switching of **D1** is observable through the material's positive thermochromic behaviour, making thermal analysis of the samples a fundamental aspect of the investigations. The colour change is an obvious indication of isomerism and has been quantified using reflectivity measurements to determine the temperatures at which events occur. This has been combined with TGA & DSC analysis and crystallographic data, where possible, to give a robust characterisation of the isolated solvatomorphs. The water solvate (**D1.1.5H_2O**) has previously been shown[113] to exhibit switching in the solid-state; thus, this is where the investigation initially focused.

3.1 Hydrated DASA; (**D1**·1.5H_2O)

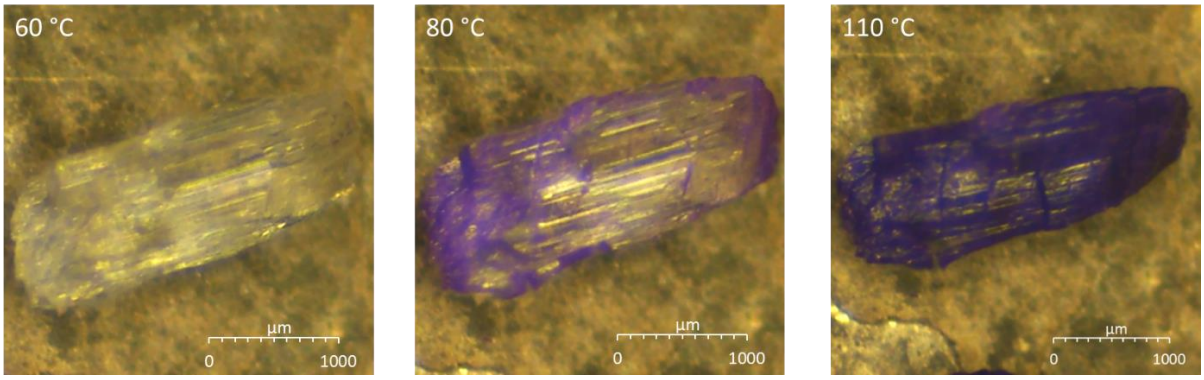

*Figure 20. Single-crystals of (**D1·1.5H_2O**) undergoing a solid-state thermochromic process under the microscope.*

Figure 20 shows the crystal before, during and after the thermochromic transition, when the crystal disintegrates. Before switching, the crystal is clear and colourless. A purple colour starts to appear on the crystal's surface, and cracks form throughout the crystal, exposing fresh internal material during heating. The whole crystal transitions and disintegrates. The solid-state switching of (**D1·1.5H_2O**) was characterised by tracking property changes of both single-crystal and powdered samples across a range of temperatures.

3.1.1 Reflectivity

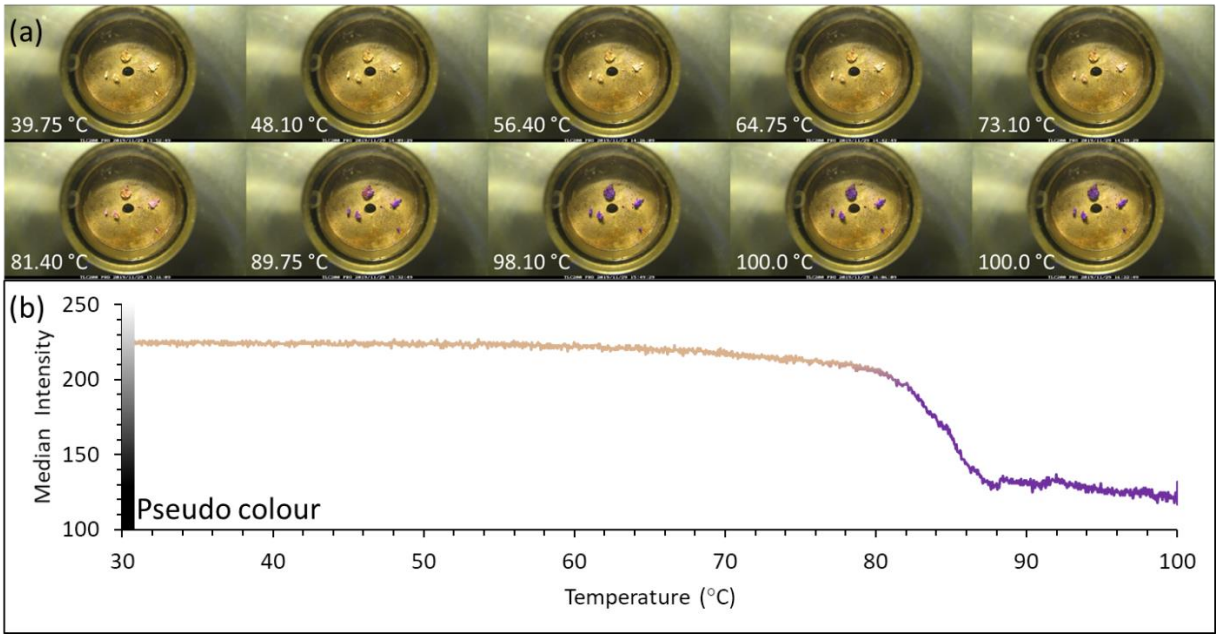

*Figure 21. a) Reflectivity measurements of (**D1·1.5H₂O**) crystals of varying size, b) Reflectivity measurements of (**D1·1.5H₂O**) as a function of temperature.*

Figure 21a shows a montage of images taken from the reflectivity measurement of (**D1·1.5H₂O**) while heating, demonstrating the thermochromism observed. Clear colourless crystals transition to dark purple colour with increasing temperature and the degradation of the crystals. From this measurement, reflectivity data were acquired, Figure 21b, as described in the experimental section. The point at which the material begins to switch can be observed visually, and by plotting reflectivity data, the switching temperature can be derived for this sample with high resolution. The determined switching temperature of this material starts at around 80 °C and completes switching by 88°C.

Figure 22 shows a montage of the same sample of (**D1·1.5H₂O**) after being crushed into a powder. The sample begins as a pale-yellow powder (60 °C – 80 °C) and as temperature increases (90 °C – 150 °C), switches to a dark purple colour, terminating at a black sintering point (~210 °C), after which it begins to melt.

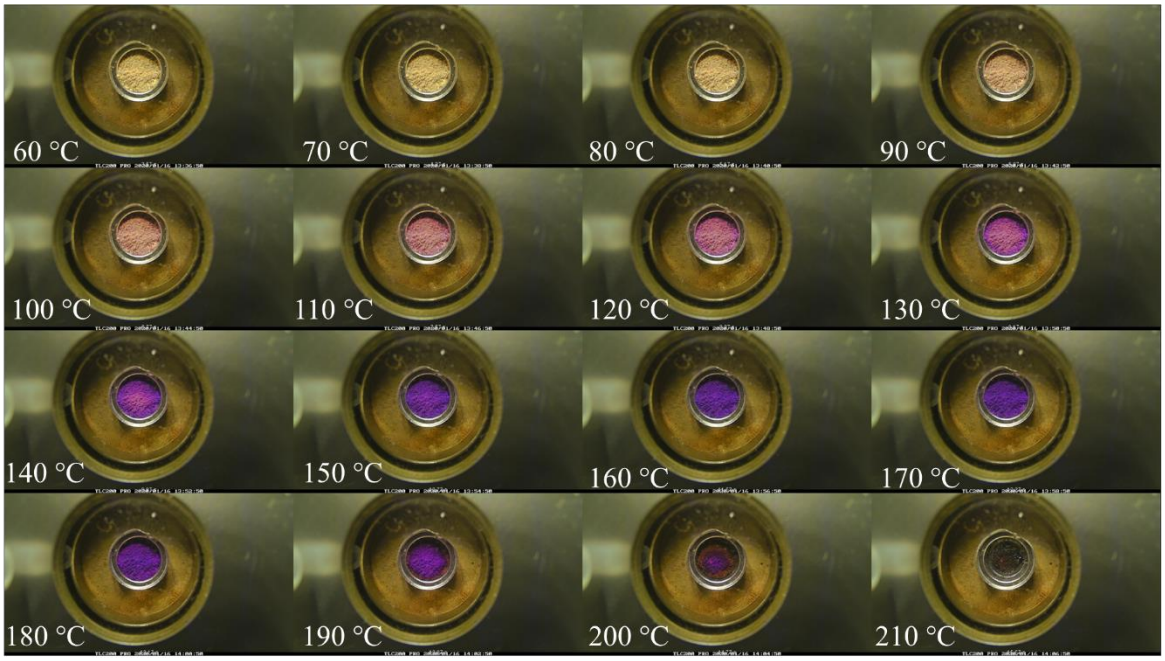

*Figure 22. Montage at 2 min intervals of the reverse isomerism of the powdered (**D1·1.5H₂O**) at a heating rate of 5 °C/min.*

Measurements on a powdered sample of (**D1·1.5H₂O**), later confirmed by PXRD in section 3.1.5, at a higher ramping rate and to higher temperatures, the material's bulk properties are observed. These differ from those of individual crystals and are summarised in the plot Figure 23a. With higher uniformity of crystallite size in the powder, compared to individual single-crystals, it is assumed that the sample's homogeneity means thermal diffusion throughout each crystallite will be largely the same and instead, any discrepancy in thermal diffusion occurs throughout the sample as a whole. This is observed in Figure 22, where the onset of the switching is between 80 °C – 90 °C depending upon the region of the sample measured, with these effects summarised in Figure 23b). As the ROI defined for Figure 23a is the whole sample, this will give an average for the pixel intensities and hence an average switching temperature.

At higher temperatures (**D1·1.5H₂O**), begins to melt and degrade and these processes start beyond 210 °C. The clear point was established to be **219 °C – 222 °C** via melting point determination as described in the experimental section 2.8.

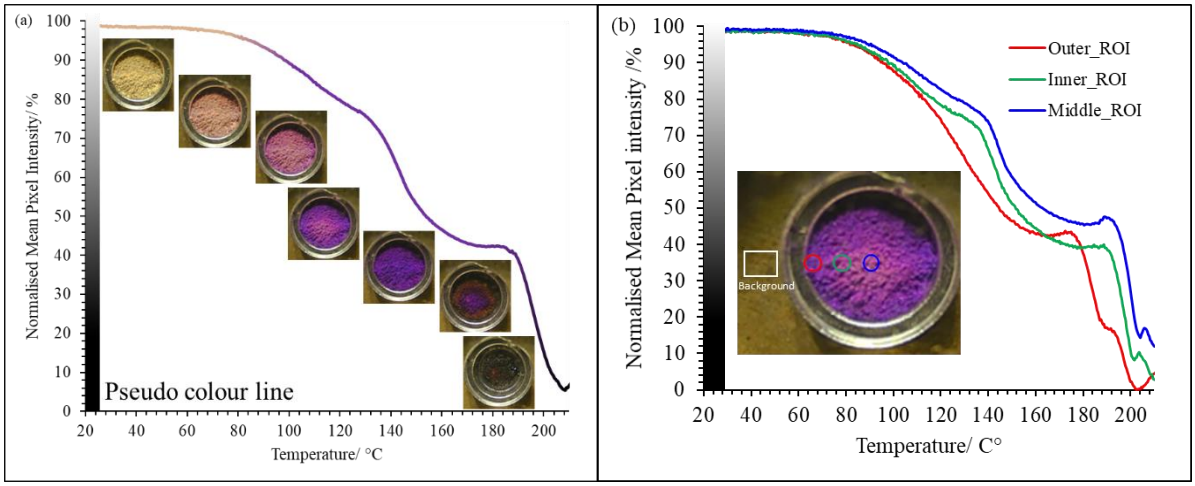

*Figure 23. Normalised reflectivity measurements at a 5 C°/min ramp rate. a) The line pseudo coloured to give approximate matches to montage images. b) Effects of thermal diffusion on the switching temperature of (**D1·1.5H₂O**) displayed by comparing regions of interest (ROI).*

3.1.2 TGA & DSC

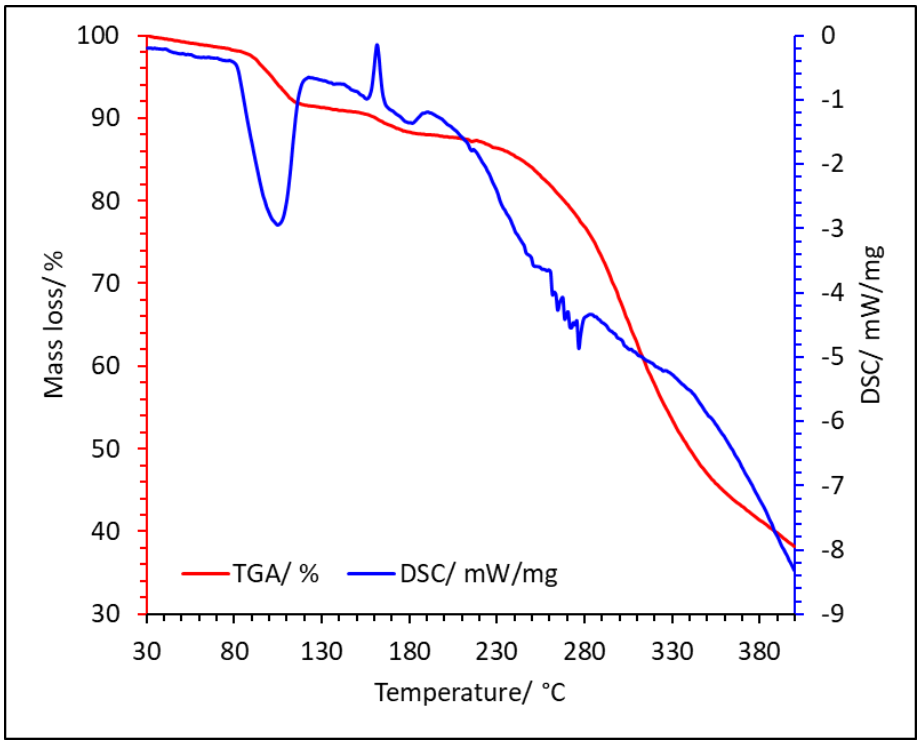

*Figure 24. Thermogravimetric analysis and differential scanning calorimetry of powdered (**D1·1.5H₂O**) under a flow of air with a ramp rate of 10 K/min.*

Simultaneous TGA & DSC were carried out on a powdered sample of (**D1·1.5H₂O**) to give insight into the thermal processes happening as the material underwent tautomerisation, and the thermogram can be seen in Figure 24. There are three observable mass loss events measured, occurring at the ranges: 80 °C – 120 °C (**6.63 %**), 150 °C – 180 °C (**2.42 %**) and 230 °C- 380 °C (**49.00 %**). There are three distinct energy flow changes, shown by the DSC, including an endothermic process centred at 97 °C

and two exothermic processes recorded at 162 °C and 192 °C. As this is a solvated crystalline sample containing water, it is expected that water loss will be attributable to at least one of these mass-loss events. The percentage weight of each water environment, based on the empirical formula calculated from the single-crystal data in Table 2, are water (O5) 5.20 % and water (O6) 2.60 % for the total theoretical water content of 7.8 % (see Figure 19a).

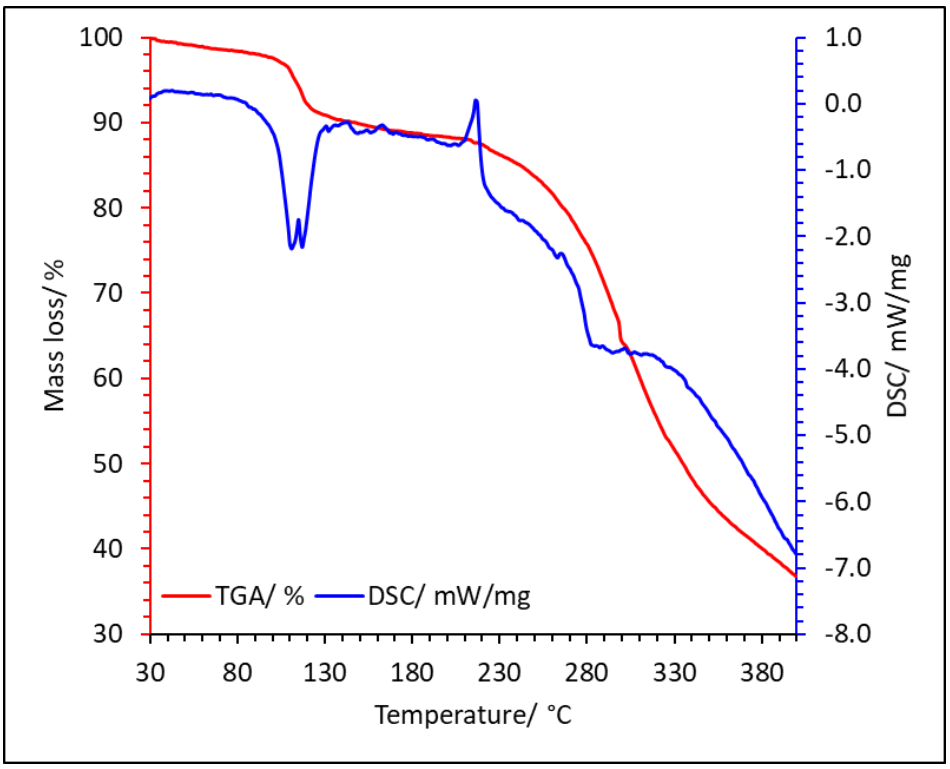

*Figure 25. Thermogravimetric analysis and differential scanning calorimetry of a single-crystal of (**D1·1.5H$_2$O**) under a flow of air with a ramp rate of 10 K/min.*

When TGA & DSC analyses were performed on a single-crystal, displayed in Figure 25, only two mass loss events occurred, with the first at 100 °C – 125 °C (**6.32 %**) and the second from 210 °C – 400 °C (**51.30 %**). The DSC is like that of the powdered sample; however, the first change in energy flow appears to be made up of two overlapping endothermic processes, with peak centres being at 111 °C and 117 °C. A change in energy flow increased and became positive at 216 °C, indicating an exothermic process was occurring, likely to do with the melting process as this also signifies the start of the second mass loss event. The temperature at which the first mass-loss event occurs is directly between the two mass loss events of the powder.

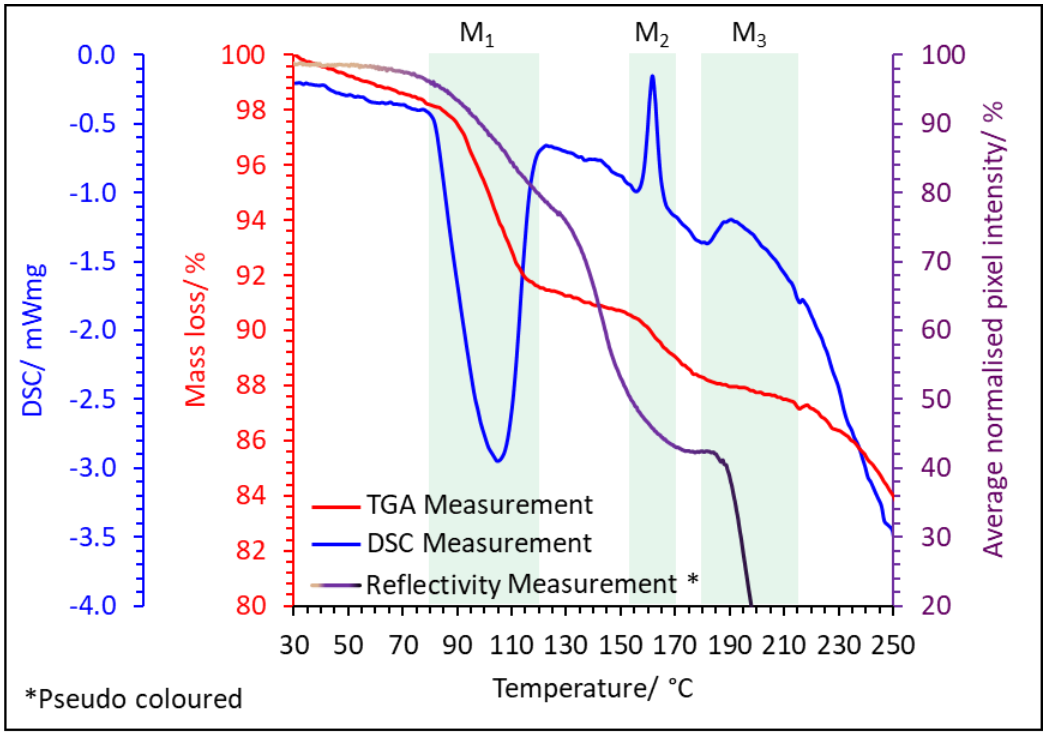

*Figure 26- Thermogravimetric analysis and differential scanning calorimetry data (Figure 24) overlaid with the reflectivity data (Figure 23a) all from powdered (**D1·1.5H$_2$O**) with significant events highlighted.*

Comparison between the TGA & DSC and reflectivity measurement, as shown in Figure 26, allows the identification of three distinct events in Figure 26: M_1, M_2 and M_3:

M_1 is the event in which the colour change is initiated from pale yellow to dark purple. There is a mass loss event associated with this colour change (**6.63 %**) which is likely water loss, and it is shown to be concomitant with an endothermic process. This water loss percentage corresponds to 1.275 of the 1.5 empirical water environments, leaving an average of 0.23 water molecules per asymmetric unit. An endothermic process could also be indicative of a phase transition from a crystalline to an amorphous solid. The colour change indicates that some degree of cyclic to linear isomerisation of the DASA occurs at this temperature, so the endothermic process could also be attributed to this chemical activity.

M_2 is the end of the colour change, with the average pixel intensity starting to stabilise as a constant dark purple. There is a mass loss during this event (**2.42 %**) as well as an exothermic process. This mass loss is likely water loss again, corresponding to 0.47 average water molecules per asymmetric unit. If both mass losses are attributed to water loss, this exceeds the sample's maximum theoretical water content (**7.8 %**). This could be accounted for if the sample had taken in more (**1.25 %**) water from the

air, which would potentially leave alongside the first water environment. This analysis suggests that single-crystals of (**D1·1.5H_2O**) lose different water environments at different temperatures, and using the empirical formula, these can be attributed to water environments from the crystal structure. The first mass loss event can be attributed to the water (O5) environment and the second mass loss event attributed to the water (O6) environment. As a powder, both water environments leave simultaneously, or at temperatures indistinguishable with this experimental set-up, potentially to-do with the increased surface area.

Finally, M_3 is the process in which the sample starts to melt and turn black. This process is further evidenced by the TGA analysis, with a relatively constant mass before the more considerable mass decrease (49.00 %) beyond the clear point. This larger mass loss event is associated with the thermal degradation of the sample in air from the decomposition of the organic components. The DSC indicates a small exothermic process at this point, likely associated with the phase transition from solid to liquid.

The switching temperature is slightly different between the two powder/single-crystal reflectivity measurements and the TGA & DSC results, even though they are both (**D1·1.5H_2O**). A potential explanation for this could be found through an investigation of the relationship between the size of the crystal, its surface area, and the switching temperature. Further work would be required to examine this possibility in detail. Another factor affecting the switching temperature is the ramping rate at which the sample heats. A higher ramping rate will give a higher perceived switching temperature as the sample has less time to equilibrate to the temperature of the surroundings and so is limited by the thermal diffusion through the sample.

These analyses' objective was to correlate the solid-state switching behaviour of this material through the inherent colour change that occurs with the mass and energy changes associated. The switching process is associated with loss of water both in single-crystals as well as in powder form. A detailed investigation of this water loss was undertaken using single-crystal X-ray diffraction.

3.1.3 Crystal packing; SCXRD with complimentary Hirshfeld Surface Analysis

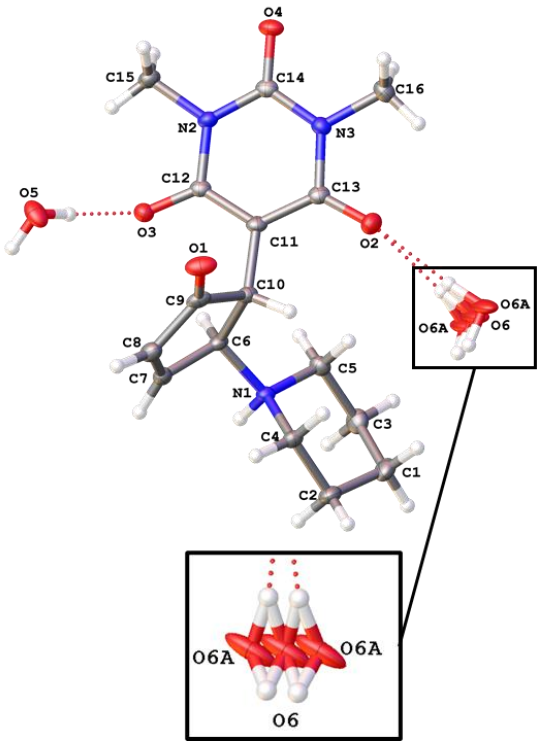

*Figure 27. The (**D1·1.5H_2O**) crystal structure showing the modelled solvent disorder of water (O6) environment at 120 K.*

SCXRD was used to confirm that the colourless crystals were indeed the cyclised form of **D1**, with the asymmetric unit displayed in Figure 27. There is a 1:1.5 molar ratio of molecules of **D1** to water, giving an empirical formula of $C_{16}H_{24}N_3O_{5.5}$. There are two crystallographically distinct water environments, water (O5) and water (O6), with the latter being disordered about a special position. At 120 K, both water molecules are modelled as fully occupied, and water (O6) was modelled over two distinct positions. At all other temperatures, the solvent disorder was modelled using a single position and an isotropic displacement parameter, as discussed in the experimental section 2.5.

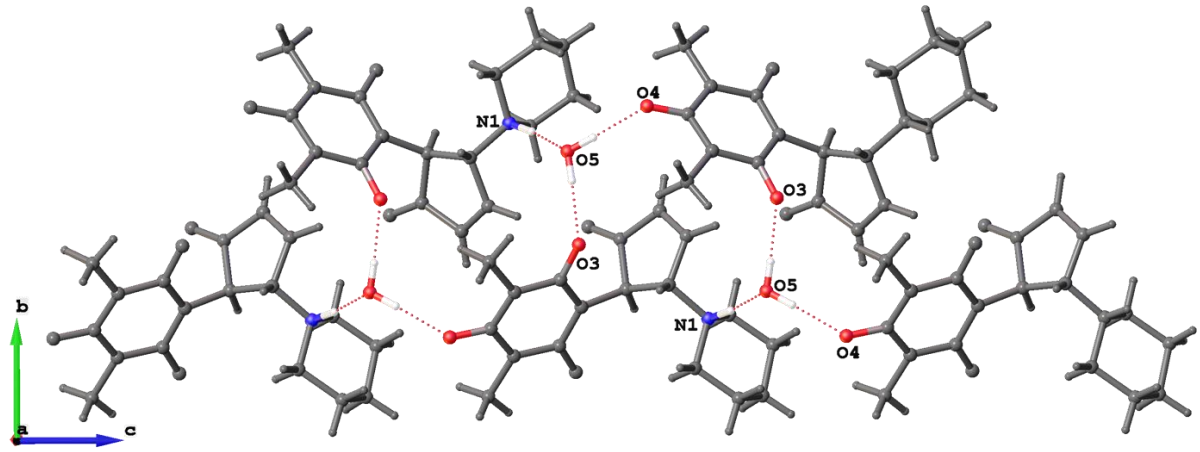

*Figure 28. The crystal packing of (**D1·1.5H$_2$O**) extending along the c-axis, bonding via hydrogen bonding, at 120 K.*

Using Olex2[117], the packing of the molecules can be explored by looking at the atomic positions and their connectivity and the implied strength of the intermolecular interactions involved in the crystal packing. Starting with the hydrogen bonding interactions between the **D1** and water (O5) molecules that are displayed in Figure 28, with the relative bond strengths (inferred from the bond lengths and angles) presented in Table 3.

Table 3. A summary of values associated with hydrogen bonding originating from water(O5) in (D1·1.5H$_2$O) at 120 K

Bond	H-Acceptor Distance/ Å	Donor-Acceptor Distance/ Å	Bond angle/ °
O5 – H ··· O4	1.90(2)	2.7686(12)	177.0(18)
O5 – H ··· O3	1.86(2)	2.7145(13)	176.1(19)
O5 ··· H – N1	1.794(17)	2.7112(13)	171.0(15)

The water (O5) forms three hydrogens bonds with **D1**, forming one-dimensional chains along the *c*-axis, as shown in Figure 28. Two of these hydrogen bonds are the hydrogens of the water (O5) acting as hydrogen bond donors, and the hydrogen bond acceptors are the π-bonded oxygens (O4, O3) of the barbituric acid ring. The bond lengths and bond angles of these two hydrogen bonds are the same, within error, indicating equivalence in these hydrogen bonds' strength. The donor-acceptor bond lengths do deviate, suggesting that the (O5-H···O3) bond is stronger than the (O5-H···O4) bond.

Water (O5) also acts as a hydrogen bond acceptor, with a hydrogen bonded to a nitrogen cation as the donor. The electronegativity of a nitrogen cation is less than that of a nitrogen atom; therefore

the N^+-H is a less polarised bond. However, the electron-donating group of the oxygen from the water (O5) stabilises the nitrogen cation making the hydrogen bond favourable.[131] This bond is comparatively more substantial than the other two, denoted by its shorter H-acceptor bond length, but the bond angle deviates more significantly from the ideal 180° to 171.0°. The donor-acceptor distance of this bond is comparable to the other hydrogen bonds in which water (O5) engages, suggesting that they are all of comparable strength. Nitrogen is a less electronegative atom than oxygen, so it is expected that these hydrogen bonds would be weaker.[132] This nitrogen cation plays a significant role in switching this material, accommodating the proton transferred from the furfural alcohol core allowing for cyclisation.

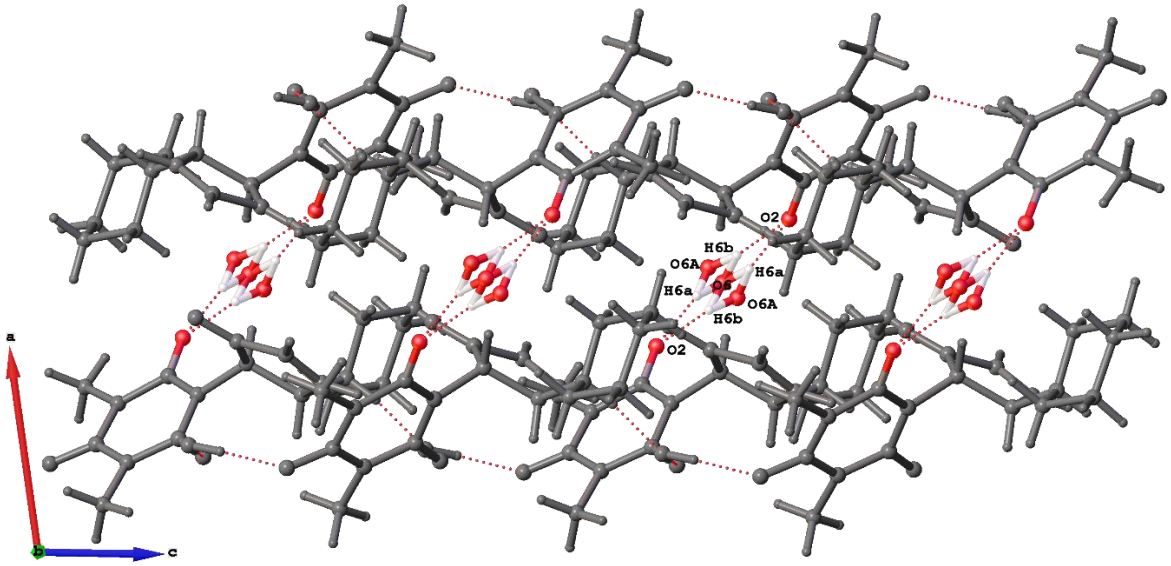

*Figure 29. Crystal packing of (**D1·1.5H₂O**), viewed down the b axis, showing hydrogen bonding, at 120 K.*

Table 4. Summary of values associated with hydrogen bonding originating from water (O6) in (D1·1.5H₂O) at 120 K

Bond	H-Acceptor Distance (Å)	Donor-Acceptor Distance (Å)	Bond angle (°)
O2 ··· H6a – O6A	2.0156(8)	2.865(9)	167.0(8)
O2 ··· H6a – O6	2.0156(8)	2.832(3)	155.83(10)
O2 ··· H6b – O6	1.9976(8)	2.832(3)	160.20(6)
O2 ··· H6b – O6A	1.9976(8)	2.861(9)	165.5(9)

It can be seen, by rotating around the *c*-axis, that the 1-D chains of **D1** and water (O5) molecules extending indefinitely along the *c*-direction are bridged together by another water (O6) environment. The result is a discrete rod-like structure that propagates along the *c*-direction, as shown in Figure 29.

The water environment involved in this hydrogen bonding, as previously discussed, has a level of disorder that has been modelled. Table 4 displays the hydrogen bond lengths and angles for the water (O6) environment from which hydrogen bond strength can be inferred. The oxygen (O6) is situated on a symmetry element; consequently, this water environment forms hydrogen bonds each with a symmetrical equivalent.

The water (O6) forms two symmetrically equivalent hydrogen bonds to the oxygen (O2) acceptor group on the barbituric acid ring. However, due to the solvent disorder, the hydrogen bond donor is subjected to different environments. The two hydrogen environments arising from the solvent disorder can either be bonded to the oxygen (O6) or oxygen (O6A), giving a total of four unique bonds. In the two cases where the hydrogen environments and the acceptor (O2) are the same, the bond distance will also be the same, but the change in oxygen (O6/O6A) environment will give an alternative bond angle for the interaction. The difference in the bond distance between the two hydrogen environments is within the estimated standard deviation (ESD), so they are considered equivalent. Although indicative of the bond strength, the values of the bond angles may not be as reliable for the disorder in the solvent due to the hydrogens being added via Q-peaks as opposed to at calculated positions, in this case.

When comparing the hydrogen bond angles for water (O5) with the hydrogen bond angles from water (O6), the hydrogen bonds associated with water (O6) are not as ideally linear. This means, for the more disordered water (O6) environment, there would be poorer covalent bonding interaction, resulting in weaker hydrogen bonds. Comparing hydrogen bond distance to those of the previous hydrogen bonds engaged with the water (O5) molecule coupled with decreased linearity shows that these bonds are significantly weaker. Weaker hydrogen bonding implies this water (O6) molecule has

higher mobility than the water (O5) molecule, and from the solvent disorder/crystal structure, more space in which to utilise this mobility. A cross-section of the rods formed by these intermolecular bonding interactions can be seen in Figure 30.

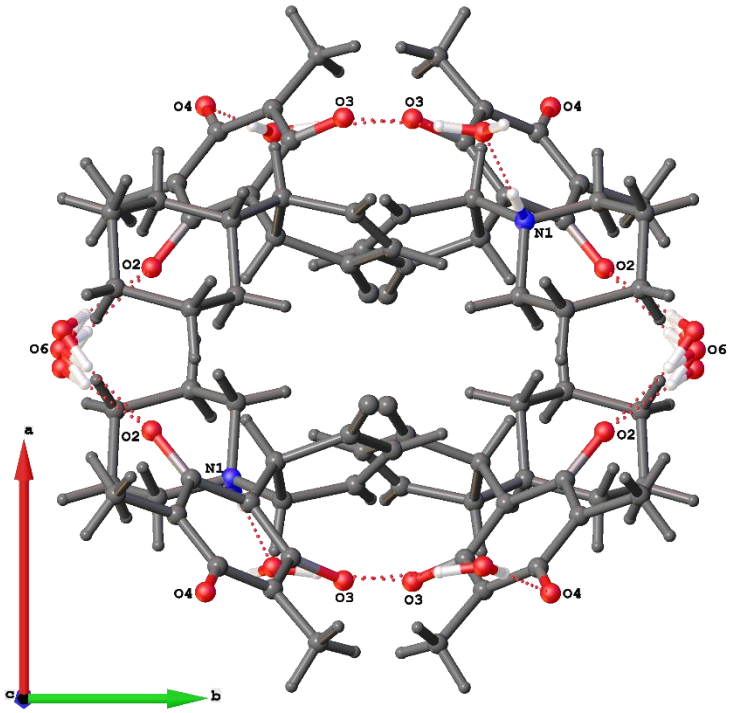

*Figure 30. Cross-section of (**D1·1.5H$_2$O**) rod structure propagating along the c-axis with hydrogen bonding interactions highlighted, at 120 K.*

Through hydrogen bonding interactions, **D1** molecules assemble as one-dimensional rods along the *c*-axis with the aid of two water molecule environments. The cross-section shows how these rods are structured with the internal part occupied by the cyclopentanone rings, which in isolation have a dielectric constant of 16.3[133], suggesting hydrophobicity. This could be a significant driving force in the self-assembly of this crystal structure.

Hirshfeld surfaces(d_{norm}) for the **D1** molecule in (**D1·1.5H$_2$O**) are shown in Figure 31a, along with a fingerprint plot summarising all close contacts between atoms of adjacent molecules. Figure 31 also shows the fingerprint plot segmented by contact type to look at specific contact types independently with their locations highlighted on the surface. The overall proportions of interactions are also displayed in Figure 31 and compare each interaction, indicating the dominating effect. In this case, the H-H contacts play a significant role in the plot's morphology, being characteristic of dispersive van der

Waals interactions. This is followed by the hydrogen bonding between the solvents and the molecules. Although the O-H contacts are less frequent than the dispersive interactions, their relative strength is indicated by the fingerprint plot. The narrow features that stretch towards the origin of the plot originate from the hydrogen bond, where each 'spike' representing either $d_i < d_e$ (O-H) or $d_i > d_e$ (H-O).

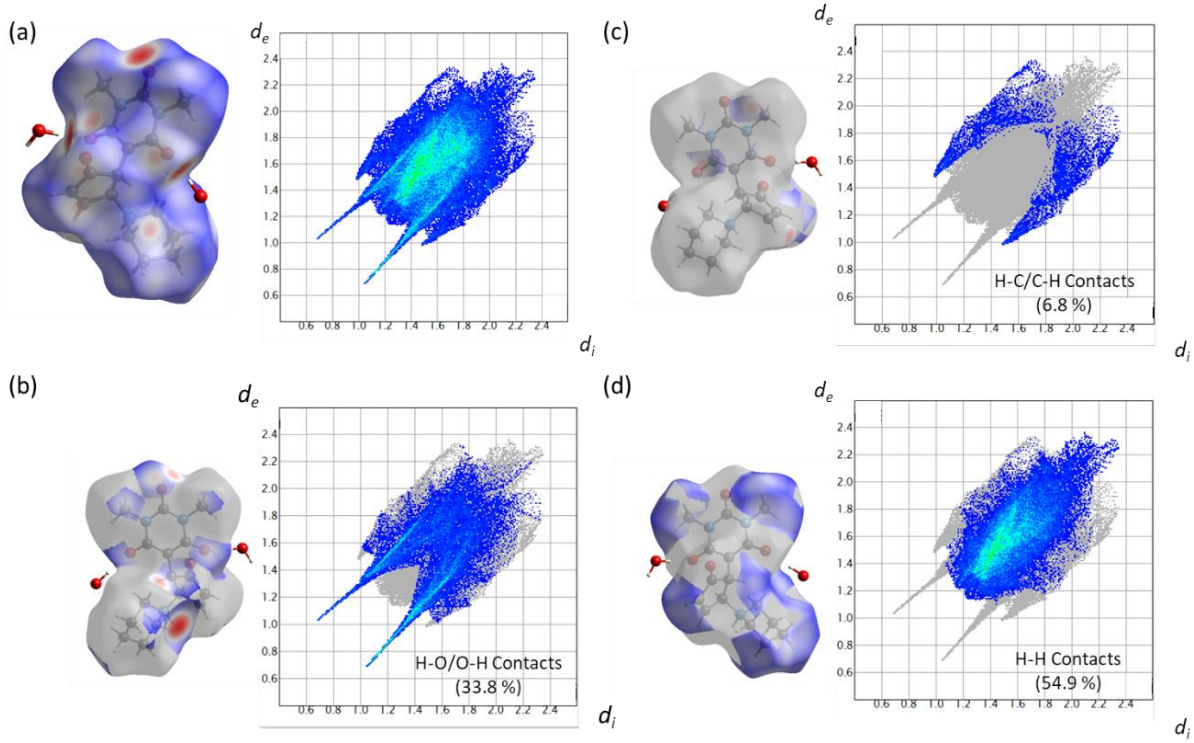

*Figure 31. The d_{norm} Hirshfeld surface at 120 K with accompanying fingerprint plot and subsequent filtering of a) (**D1·1.5H₂O**), with b) showing O-H/H-O contacts, b) H-C/C-H contacts, and c) H-H contacts.*

Because this molecule contains a variety of oxygen and hydrogen environments and not all are directly involved in hydrogen bonding, Figure 31b also shows some dispersive interactions from these environments. The greener colour in this plot region indicates that the shorter H-H contacts are of a higher frequency for this system. This, together with the H-H interactions, make-up ~90 % of all intermolecular interactions suggesting these are the dominating effect.

The non-hydrogen-bonding contacts that were observed between **D1** molecules are summarised in Table 5 with O-H contacts that are not necessarily hydrogen bonds. The shortest of these (O···H-C) contacts is between the pi-bonded oxygen (O4) on the barbituric ring and the hydrogen bonded to carbon (C5) of the piperidine ring. These interactions are between the rods along the *a*-direction but

are significantly longer interactions than the previously discussed hydrogen bonding interactions and consequently expected to be much weaker. An even weaker O-H contact is between the water (O6) and the hydrogen bonded to carbon (C1) on the piperidine ring. This contact is along the *b*-direction, stacking the rods on top of another.

Table 5. Interatomic distances for close contacts of (D1·1.5H_2O) at 120 K

Atom labels	Distance/ Å	Donor-acceptor distance/Å	Angle/ °
O4 ··· H – C5	2.439(16)	3.3616(15)	161.8(13)
C12 ··· H – C7	2.594(16)	3.4227(16)	147.2(12)
O6 ··· H – C1	2.633(19)	3.499(4)	149.5(14)

The outer 'winged' features, produced from the C-H interactions, are of low frequency and only makeup 6.8 % of the total interactions in the plot, Figure 31c. However, they are stronger than the H-H interactions in this case with a shorter d_i and d_e than the shortest dispersive features of Figure 31d. The shortest C-H contact is an interaction between carbon (C12) on the barbituric acid ring and the hydrogen bonded to carbon (C7) from an adjacent cyclopentanone core. This may not necessarily constitute a formal bonding interaction, but the proximity indicates some degree of attractive force, likely a van der Waals interaction.

Of course, there are dispersive H-H contacts along with other van der Waals forces that contribute to the packing of these rods to form a crystal structure, but those discussed in this section are the shortest of these interatomic contacts. The full packing of the crystal can now be considered.

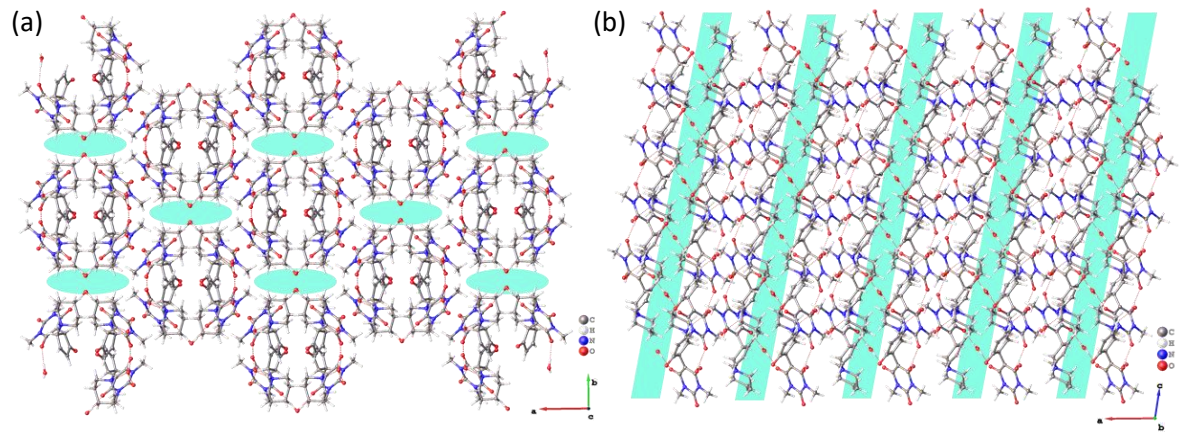

*Figure 32. View of the crystal packing of (**D1·1.5H$_2$O**) viewed down the c-axis (a) and the b-axis (b) both with aqua-coloured regions highlighting solvent channels through the crystal.*

With the rods packed together in the *ab*-plane by the short C-H contacts and H-H interactions, a porous structure forms with channels containing the disordered water (O6) environment. The rods pack together in a regular arrangement along the *c*-axis as seen in Figure 32a, and the formed channels can be clearly observed in Figure 32b in both instances highlighted by the figure's aqua-coloured regions.

In summary, the crystal packing of (**D1·1.5H$_2$O**) consists of one-dimensional rods linked via hydrogen bonding to the water (O5) environment, and these rods then bind together via the second water environment, water (O6). The space between the rods, in which the water (O6) occupies, are solvent channels along the *c*-axis. These are identifiable in Figure 32 by the highlighted aqua coloured regions. The intermolecular interactions are predominantly H-H contacts and stronger hydrogen bonding interactions. To understand how this solid-state morphology is related to the switchable properties of the material, variable temperature experiments were conducted.

3.1.4 Variable temperature analysis

In an attempt to explore the water loss from the crystal as a function of the temperature, diffraction methods were used alongside the previously established physical characterisation methods. Table 6 presents the unit cell parameters produced from variable temperature single-crystal X-ray diffraction (VT-SCXRD).

Table 6. The unit cell parameters of the (D1·1.5H_2O) at varying temperatures

Collection Temperature (K)	a/ Å	b/ Å	c/ Å	β/ °	Cell volume/ Å³
120	21.2505(3)	13.74910(19)	11.50249(15)	99.0204(13)	3319.17(8)
150	21.30932(19)	13.76512(12)	11.50918(12)	99.0903(9)	3333.54(5)
170	21.3451(3)	13.77871(18)	11.50969(14)	99.1503(12)	3342.02(8)
220	21.4504(3)	13.81209(19)	11.51897(15)	99.2757(13)	3368.15(8)
270	21.5651(6)	13.8480(4)	11.5231(3)	99.418(2)	3394.79(16)
290	21.6193(9)	13.8742(5)	11.5308(4)	99.526(4)	3411.0(2)
295	21.6200(7)	13.8620(4)	11.5120(5)	99.575(4)	3402.0(2)
300	21.6358(9)	13.8712(5)	11.5371(4)	99.530(4)	3414.6(2)
305	21.6483(4)	13.8757(3)	11.5295(2)	99.531(2)	3415.51(12)
310	21.6481(14)	13.8790(7)	11.5453(7)	99.612(6)	3420.1(3)
315	21.6899(14)	13.8882(10)	11.5300(7)	99.619(6)	3424.4(4)
325	21.6821(18)	13.9010(13)	11.5423(10)	99.584(8)	3430.3(5)
335	21.677(4)	13.894(3)	11.522(2)	99.540(19)	3422.4(12)
345	21.80(2)	13.948(6)	11.592(8)	99.52(7)	3476(4)

As expected, with increasing temperature, there is a general expansion of the unit cell, observed as increasing cell volume. However, this expansion is asymmetric, as displayed in Figure 33, with the expansion rate for each unit cell parameter being independent of each other. The figure shows that expansion along the *a*-axis is substantially more significant, being twice that of the *b*-axis and ten times the rate of expansion in the *c*-axis.

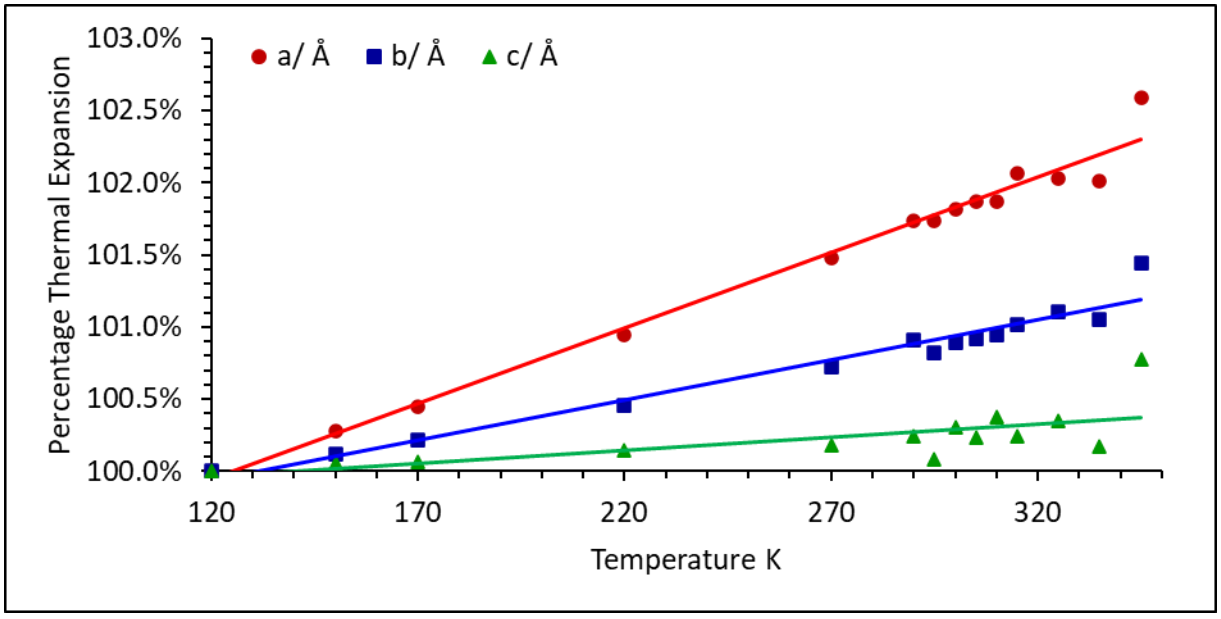

*Figure 33. The non-uniform thermal expansion of the (**D1·1.5H_2O**) unit cell.*

This shows that the material favours expansion along the *a*-axis whilst having less expansion along the *b*-axis and even less along the *c*-axis. The chain-structures run along the *c*-direction bonded together by the water (O5) environment via strong hydrogen bonding, and so being the strongest of the intermolecular forces are the least likely to be initially overcome, allowing for expansion. The rods are formed by bridging two of these chains together along the *a*-direction by weaker but still firm hydrogen bonds. The rods then stack together, running along the *c*-axis in a way resembling honeycomb. Channels of the water (O6) environment formed from this stacking run along the *c*-direction too, but run perpendicular to the *a*-axis, as displayed in Figure 32. With an increase in temperature, the intermolecular interactions responsible for the close packing will likely be lengthened, increasing the diameter of the channels until, eventually, the interactions are lost altogether. The channels are an artefact of the rods packing together, which do so through weaker intermolecular interactions. As the temperature increases, these weaker interactions may lengthen along the *ab*-axis.

Table 7. Hydrogen bonding donor-acceptor distances and bond angles at different temperatures of (D1·1.5H_2O)

Temperature/ K	*O5 - N1 (D-A)/ Å*	*O5 - N1 angle/ °*	*O5 - O3 (D-A)/ Å*	*O5 - O3 angle/ °*	*O5 - O4 (D-A)/ Å*	*O5 - O4 angle/ °*	*O6 - O2 (D-A)/ Å*	*O6 - O2 angle/ °*
120	2.711(3)	171.1(19)	2.715(3)	176(3)	2.769(3)	177(3)	2.827(10)	173(6)
150	2.713(3)	170.7(19)	2.716(3)	175(3)	2.772(3)	175(3)	2.832(10)	179(6)
170	2.715(3)	170.8(19)	2.716(3)	176(3)	2.774(3)	175(3)	2.839(10)	177(6)
220	2.720(3)	172.8(19)	2.717(3)	175(3)	2.782(3)	175(3)	2.840(10)	159(6)
270	2.728(3)	171.4(19)	2.722(3)	176(3)	2.789(3)	175(3)	2.844(10)	174(6)
290	2.731(3)	172.3(19)	2.723(3)	177(3)	2.794(3)	174(3)	2.847(10)	172(6)
295	2.731(3)	171.8(19)	2.724(3)	177(3)	2.794(3)	175(3)	2.848(10)	171(6)
300	2.730(3)	175.2(19)	2.722(3)	176(3)	2.798(3)	174(3)	2.849(10)	171(6)
305	2.731(3)	172.8(19)	2.724(3)	176(3)	2.795(3)	175(3)	2.847(10)	171(6)
310	2.733(3)	174.7(19)	2.726(3)	177(3)	2.799(3)	172(3)	2.849(10)	162(6)
315	2.736(3)	171.6(19)	2.723(3)	179(3)	2.801(3)	171(3)	2.848(10)	159(6)
325	2.733(3)	166.9(19)	2.730(3)	175(3)	2.803(3)	170(3)	2.859(10)	171(6)

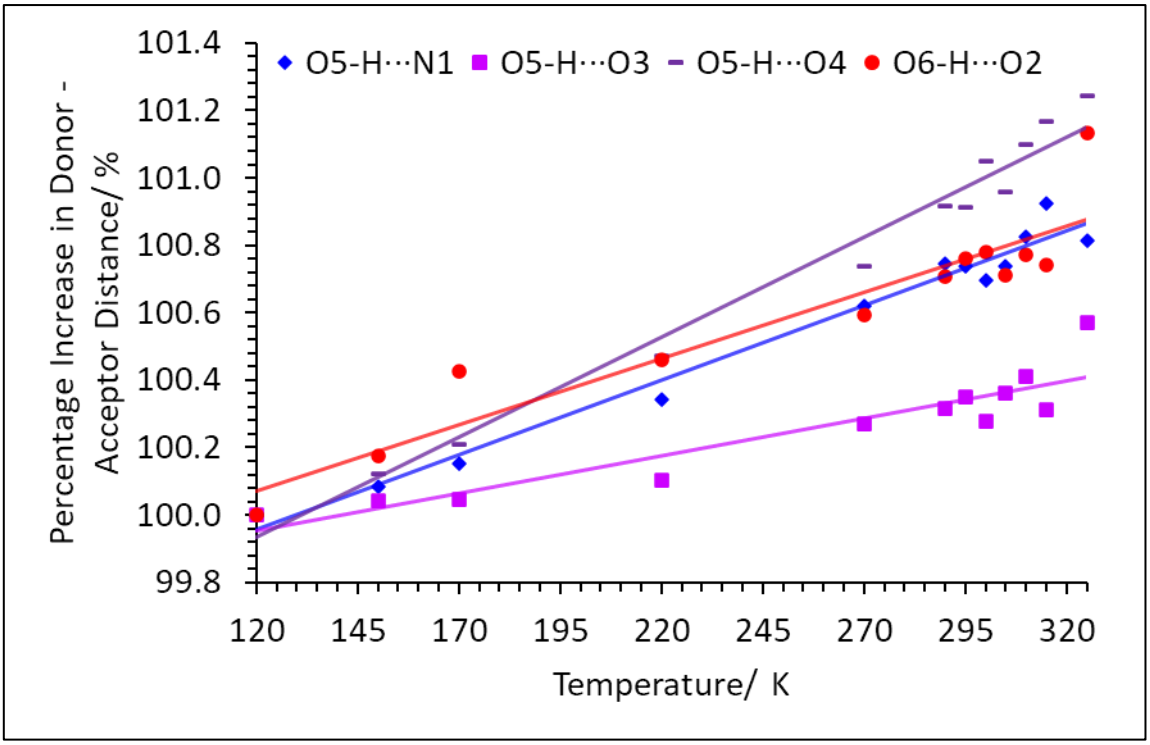

*Figure 34. The change in hydrogen bond length for (**D1·1.5H₂O**) with increasing temperature.*

This process can be observed more directly by looking at the donor-acceptor distance for the hydrogen bonds within the rod structures and how these change with temperature. This data is summarised in Table 7 and presented in Figure 34. These show that the percentage increase in donor-acceptor distance with increasing temperature is mostly the same between the two water (O5, O6) environments. The hydrogen bond with the most considerable rate of expansion, the O5-H···O4 bond, extends the structure along the *c*-direction, which when looking at the unit cell parameters is the lowest percentage thermal expansion for the unit cell.

This data shows that as temperature increases, the unit cell preferentially expands along the *a* and *b* directions, but the hydrogen bonds do not significantly lengthen when compared to the unit cell. This suggests that the rods stay intact, and the space between them increases with temperature increasing the volume of the channels.

The atomic displacement parameter (ADP) for the water (O6) environment was significantly larger with increasing temperature than the other ADPs in the crystal structure. As the water (O6) occupies and likely vacates the structure through these channels, a different approach can be taken.

To quantify the desolvation of the crystal structure, as a function of temperature, the oxygen atom (O6) was modelled using an isotropic ADP. The magnitude of this parameter was fixed and the occupancy of the atom refined. This gives the percentage occupancy of the water (O6) position and so the amount of water that has already vacated the lattice at a given temperature calculated. This is displayed in Figure 35.

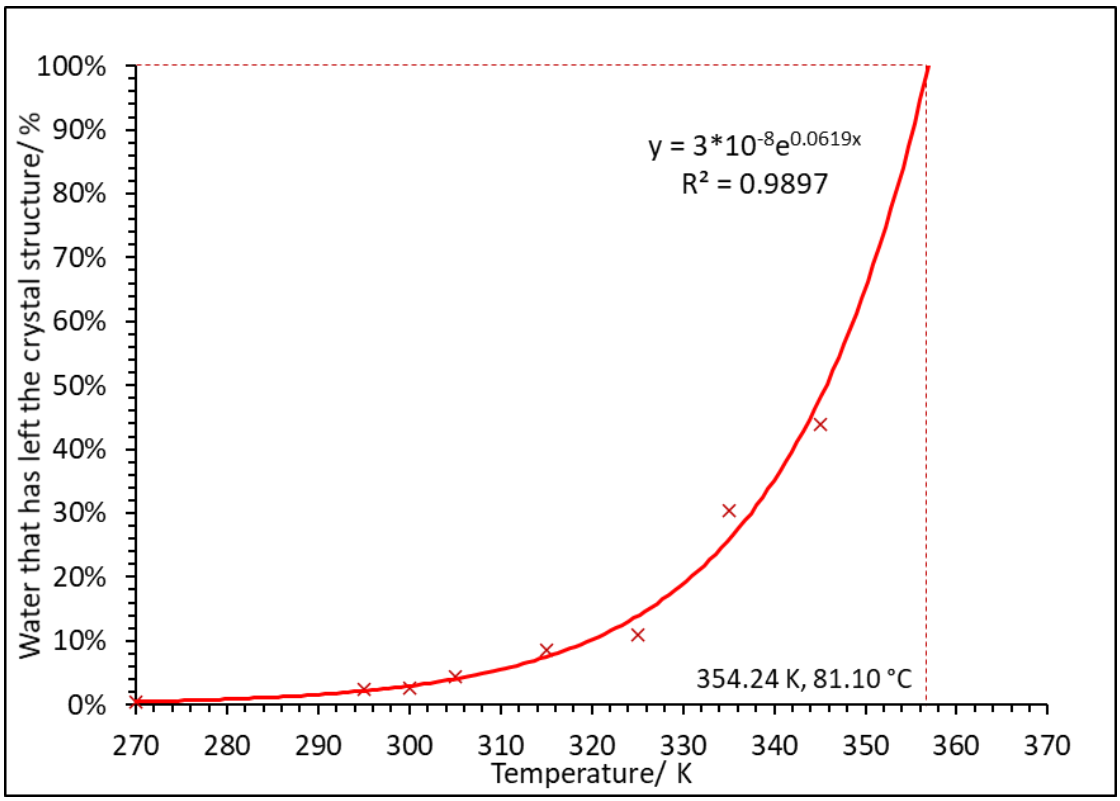

*Figure 35. The effect of temperature on the percentage occupancy of water (O6) within the (**D1·1.5H$_2$O**) crystal lattice.*

An exponential increase is observed for temperatures above 270 K, where all lower temperatures are assumed to have 100 % occupancy, with the exponential curve tending to zero. The general increase in thermal motion from heating a crystal lattice will increase the ADP of the modelled atoms, which is intrinsically linked to the occupancy; this was corrected by fixing the ADP of water (O6) to another oxygen (O1) atom within the same structure at the same temperature. The reduction of occupancy of the oxygen (O6) atom is observed by a reduction in average electron density across the crystal structure at the oxygen (O6) sites with increasing temperature. Therefore, the percentage occupancy of the water (O6) site is synonymous with the average water (O6) content of the whole crystal.

The water (O5) does not have a noticeable decrease in occupancy and is assumed to leave the crystal structure after the water (O6) has left the crystal through the channels along the *c*-direction. Interestingly, this is a direct contradiction of the evidence interpreted from the TGA & DSC analysis and is currently unexplained.

This initial departure could either instigate; the switching process causing the other water (O5) environment to leave the structure or the departure of the water (O5) environment resulting in the switching process. The TGA & DSC data suggest a two-step process occurring for single-crystals (Figure 25), and so the latter is more likely. By extrapolating the exponential curve generated from the variable temperature occupancy analysis, a temperature value of 81 °C is calculated to coincide with 100 % water (O6) loss. This matches the combined reflectivity and combined TGA & DSC experimental observations (Figure 26) for the switching temperature of (**D1·1.5H_2O**).

In summary, Figure 35 shows the departure of the water from the channels within the crystal. This trend supports the idea previously discussed from the TGA & DSC data; the vacation of water from the crystal structure is linked to the switching of the material.

The limit to which these measurements can be taken for (**D1·1.5H_2O**) is 345 K because with increasing temperature, the material undergoes tautomerism from the crystalline cyclised form to the linear form, upon which the crystal begins to disintegrate as it becomes purple, as seen in Figure 20. The temperature of disintegration is lower for crystals mounted on the diffractometer due to the use of the cryostream, a constant flow of dry nitrogen over the crystal. This likely has a mechanical action increasing diffusion rates, removing solvent from the structure faster than in ambient conditions.

3.1.5 Powder X-ray diffraction (PXRD)

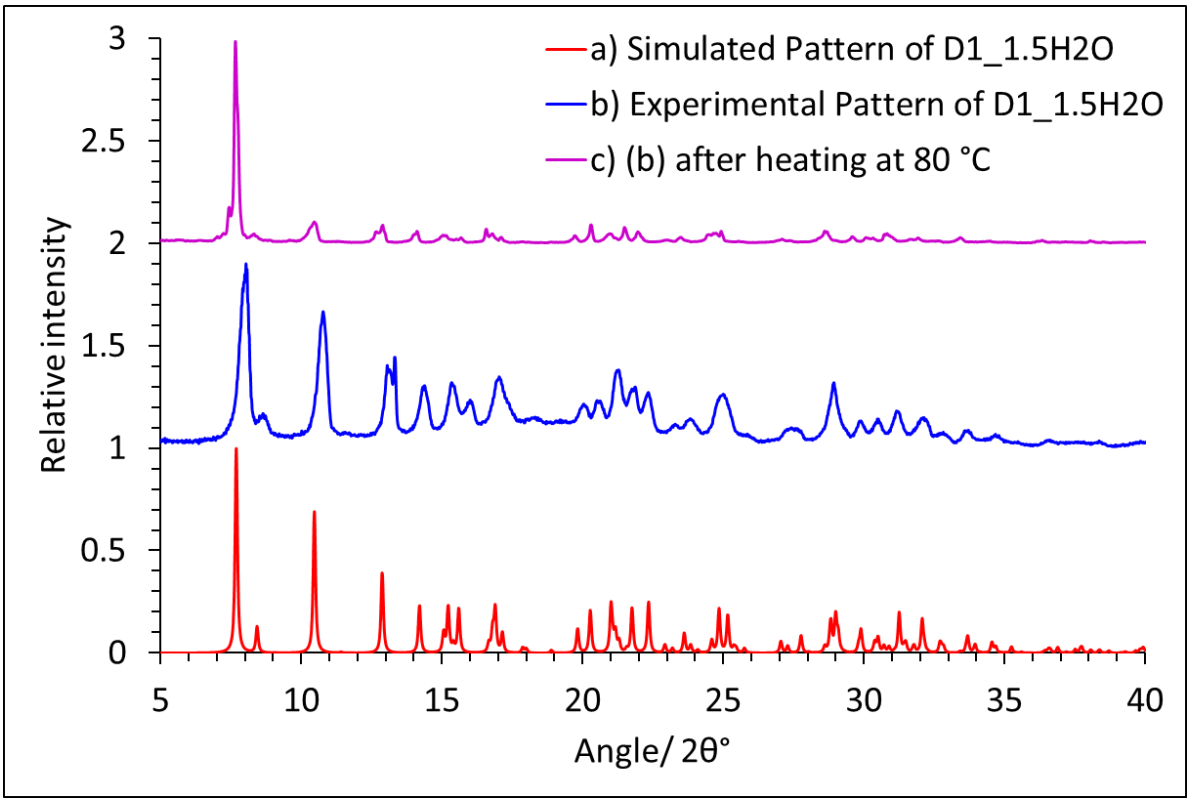

*Figure 36. PXRD patterns of (**D1·1.5H₂O**) from: a) simulated from Single-crystal X-ray diffraction data, b) experimental PXRD pattern collected at room temperature, c) pattern after heating to 80 °C for 1 hour (turned purple).*

PXRD analysis is used for further structural investigations at room temperature, with the sample being heated in an oven to 80 °C for 1 hour and cooled before a further diffraction pattern was collected. The powder X-ray diffraction data, Figure 36, shows that crushed (**D1·1.5H₂O**) are the same solvatomorph as the single-crystals. The analysis also confirms the crystalline phase purity of the sample with no other polymorphs or crystalline impurities present in the sample. Upon heating the sample to the switching temperature calculated for this solvatomorph, a decrease in crystallinity was presumed, more noticeable at higher angles. This is suggestive that upon switching, the material undergoes a phase transition to a non-crystalline state.

This makes the linear DASA more challenging to characterise. Spectroscopic analysis by Raman and FTIR also proved challenging due to broad overlapping peaks and fluorescence. Surprisingly, there was no strong broad O-H bands observed in FTIR and the transparent crystals and purple powder had very similar spectra, these can be seen in the appendix as Figure F. Solid-state fluorescence spectroscopy

was also attempted, but the results were low quality from the overwhelming of the detector, these are shown in Figure E of the Appendix. Only preliminary results were recorded using these techniques, and these were unable to be completed due to the COVID-19 university closure. Future work to help understand the other side of the switching process could include a collaboration with an institution with access to solid-state NMR facilities to study the local structure of the DASA molecules in their linear form in the solid-state.

3.1.6 Humidity induced switching and Tribochromism

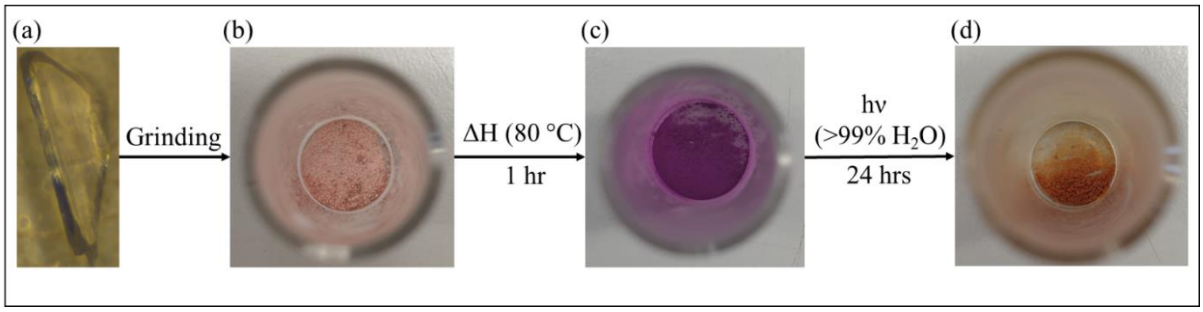

*Figure 37. A qualitative summary of tribochromsim of (**D1·1.5H₂O**) and its humidity-induced reversibility from: (a) a clear colourless crystal of (**D1·1.5H₂O**); (b) crystals that have been lightly ground; (c) after heating at 80°C; (d) the co-operative hygro-photochromism.*

The multi-responsiveness of (**D1·1.5H$_2$O**) has been qualitatively investigated by means of controlled grinding to look at the potential for tribochromism and controlled humidity environments to assess if the material shows hygrochromism. Light intensity was also investigated to determine whether these were acting independently or co-operatively. This was done by placing samples in both high and low humidity environments in the dark and exposed to white light.

Figure 37(b-c) shows the colour change associated with the heating of the material, but to check the sample's reversibility, it was placed in a closed high humidity chamber under the light to identify a reversible colour change in the solid-state Figure 37(c-d). Water has been reported in the literature as independently inducing the switching process in solution[7,107] but whether this extends to the solid-state is what is being investigated. Vapochromsim is a known property of organic materials, although the field, like DASA chemistry, is still only in its infancy.[134] The uptake of water by the high humidity (>99%) samples were confirmed gravimetrically with samples in high humidity chambers, in the light

and dark, undergoing colour change and mass increase whilst samples in lower humidity (<20%) in the dark did not change colour or gain significant mass.[135] But this is still only a qualitative approach, FTIR spectra were taken pre and post exposure to light and humidity, figure G in the appendix, but little was understood from these, so more work is needed to understand this further.

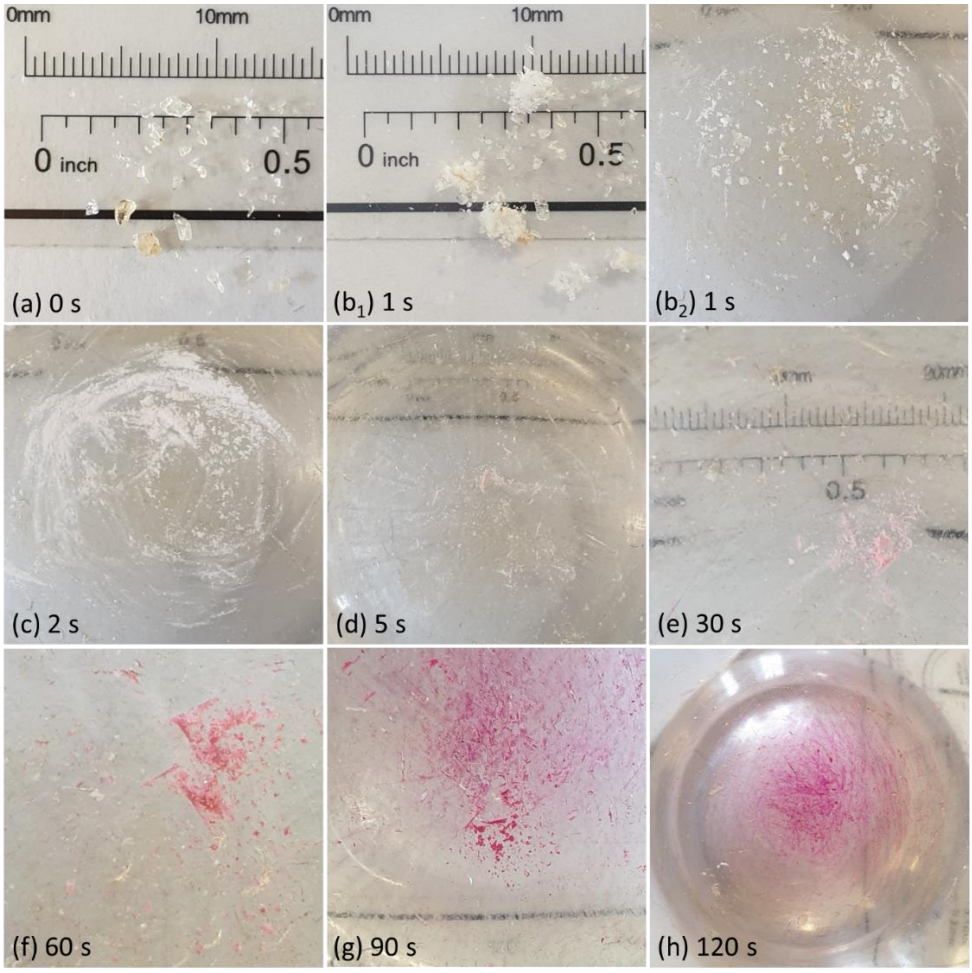

Figure 38. (a-h) The grinding stages show the effect of mechanical force on the colour of ***(D1·1.5H$_2$O)****.*

The effect of grinding the sample was first observed during the PXRD sample preparation. Figure 38 shows various intervals of grinding, and the associated mechanically induced colour changes. Pictures b_1-b_2 show the transfer of lightly crushed crystals to a glass mortar and pestle. The cumulative grinding time associated with each image is displayed in the lower left-hand corner.

Increased grinding duration results in smaller particle size of the crystallites, so there is a higher surface area for water loss to occur from the sample, inducing the isomerism. An alternative possibility is that the local heat generated by the mechanical grinding causes the switch (thermochromism), so

further work is required to confirm these ideas. Mechanically induced tautomerism is not a new idea,[55,136–138] but it is uncommon, and this is the first instance observed for DASAs. This could lead to applications such as frictional indicators in engineering with DASAs used as monitors for lubricant performance, for which the thermochromic properties complement.

3.2 Unsolvated DASA; (**D1·unsolv**)

The crystallographic data displayed in Table 2 indicates that the material isolated from methanol is purely a **D1** crystal with no solvation. This is a good control sample as the solvatomorphism must be responsible for any differences in properties. This crystal does not undergo the same thermochromism observed in the solvatomorphs, so solid-state switching was assumed not to occur. Because of this, the solid-state switching is increasingly likely to be linked to the solvation. Figure 39 shows a single-crystal of (**D1·usolv**) being heated to beyond the melting point, before which the material fails to entirely switch with only surface changes observable.

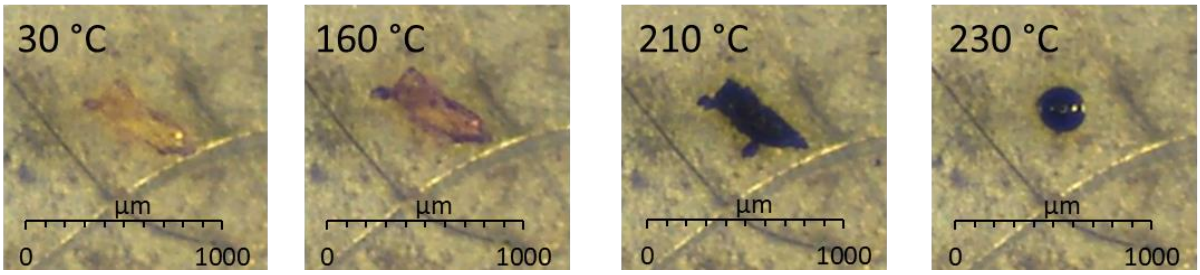

*Figure 39. A crystal of (**D1·unsolv**) heated under the microscope, showing a surface change but no bulk switching, before the crystal melts and degrades.*

3.2.1 Reflectivity

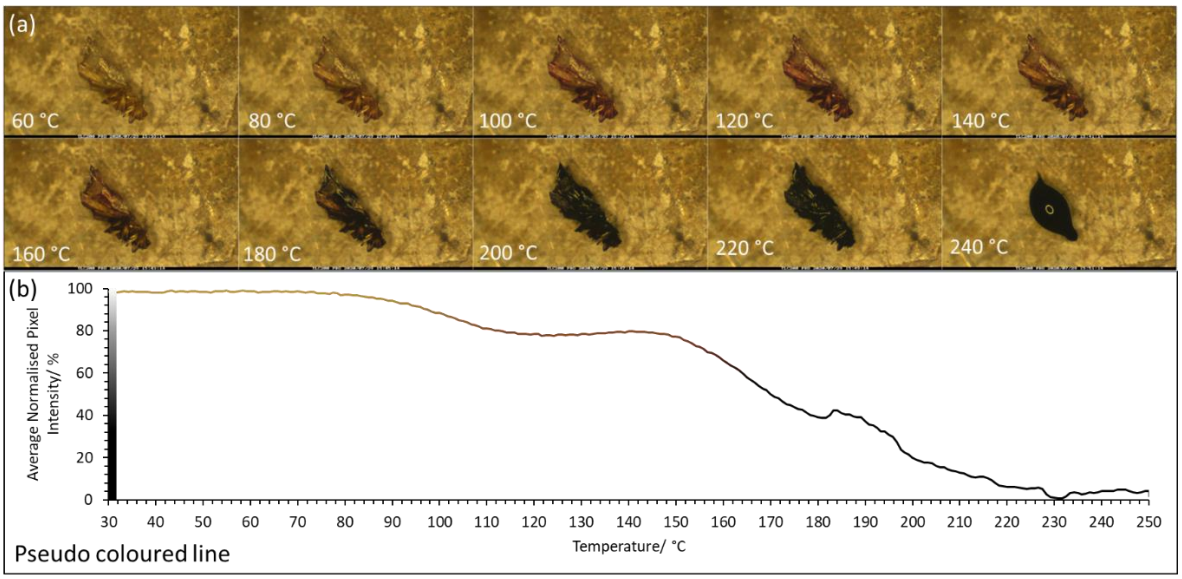

*Figure 40. (a) Montage at 2-minute intervals of a (**D1·unsolv**) crystal cluster at a heating rate of 10 °C/min (b) Reflectivity measurement of (**D1·unsolv**) with average normalised pixel intensity plotted as a function of temperature.*

A cluster of (D1·unsolv) crystals can be seen in Figure 40a, heating at a constant 10 °C/min rate. As before, reflectivity data were extracted and plotted as a function of temperature, Figure 40b. The reflectivity curve shows a minor colour change at ≈100 °C and then a significant colour change initiating at 150 °C. The minor colour change initiated at 100 °C is of unknown origin, however, this was observed as a surface change only and not concurrent with the solid-state switching observed in the other solvatomorphs in which the whole crystal changes.

There could be a variety of explanations for this surface change: the crystal has interacted with the humidity in the air and become hydrated; upon crystallisation, a non-crystalline film coated the crystals and was invisible to diffraction methods yet exhibits solid-state switching; perhaps solid-state switching does occur in this sample, but there is only enough molecular mobility on the surface of the crystal to allow this whilst the vacation of solvent from other crystals allows the change to occur throughout the crystal. However, in the absence of further investigation, all suggestions here remain speculative.

The average crystallite size of (**D1·unsolv**) is much smaller than that of (**D1·1.5H$_2$O**), and so inhomogeneous thermal diffusion is a less significant variable when interpreting thermal analysis.

3.2.2 TGA & DSC

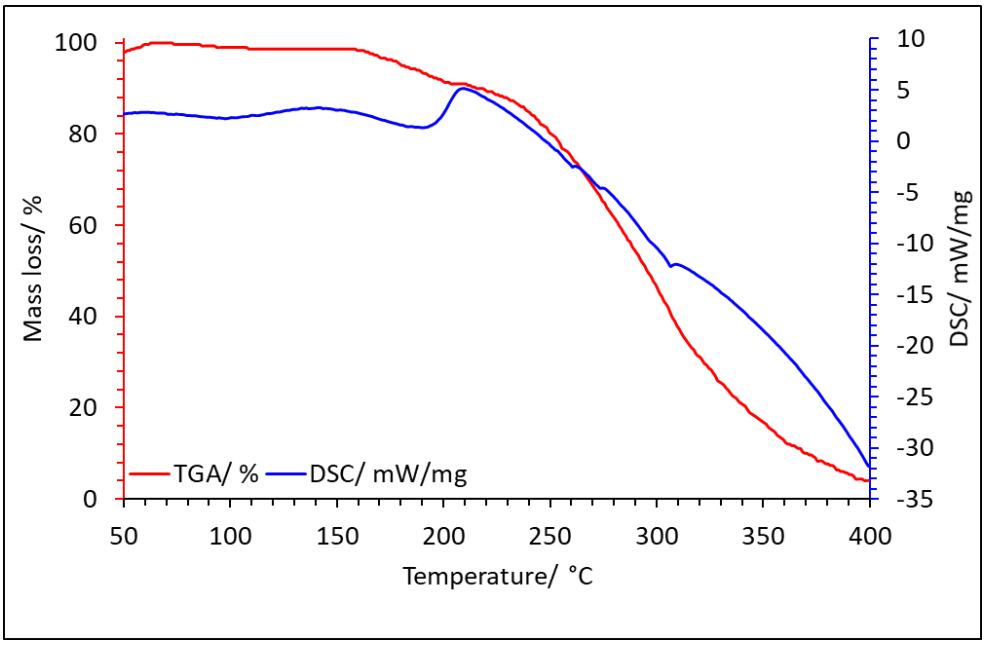

*Figure 41.Thermogravimetric analysis and differential scanning calorimetry of (**D1·unsolv**) powder under a flow of air with a ramp rate of 10 K/min.*

The TGA & DSC analysis for (**D1·unsolv**) is shown in Figure 41 and displays a two-step mass loss event. This initiates at 170 °C, with the second step occurring at 214 °C. The DSC shows a small exothermic event centred at 150 °C with a second larger exothermic event centred at 214 °C. There is no mass loss associated with the first exothermic process, but the second is likely the result of the sample melting and thermal degradation of the wholly organic components.

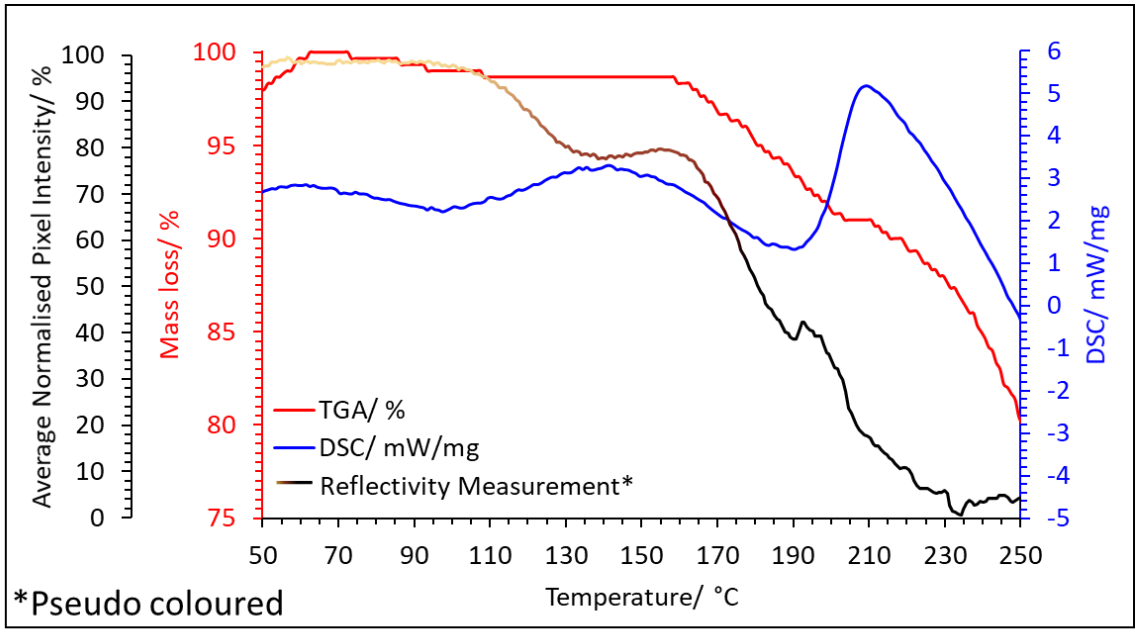

*Figure 42. Thermogravimetric analysis and differential scanning calorimetry data (Figure 41) overlaid with the reflectivity data (Figure 40b) all from (**D1·unsolv**) samples.*

The relationship between the thermal processes and colour change can be correlated by isolating a specific data range from Figure 41 and overlaying reflectivity data (Figure 40b). The initiation of the first exothermic process at 100 °C coincides with the initiation of the minor colour change and is centred on its completion at 150 °C. The sample's mass then starts to decrease slightly as the first step of the mass loss event, before being followed by the bulk of the sample melting at 214 °C observed from the exothermic process on the DSC curve and then the thermal degradation.

This brings into question the phase purity of the sample; the crystals were formed by complete slow evaporation and due to size and low abundance, unable to be washed. This could mean an amorphous non-crystalline trace impurity of **D1** is present within the sample and undergoes a colour change, and subsequently degrades at a slightly lower temperature than the crystalline form. The basis for this idea is that there is no mass loss detected before the event at 170 °C, and so possible causes for the surface colour change of the crystal would be those that only involve energy changes, observable by DSC. This suggests a thin switchable amorphous layer partially coating the crystal, being the likely cause for the surface colour change. This is purely speculation, and further analysis would be required to confirm this.

3.2.3 Crystal packing; SCXRD with complimentary Hirshfeld Surface Analysis

SCXRD confirms there was no solvent present within the (**D1·unsolv**) crystal structure. The asymmetric unit can be seen in Figure 43. The lack of solvent in this structure is likely the reason crystalline samples do not exhibit solid-state switching through the bulk of the material.

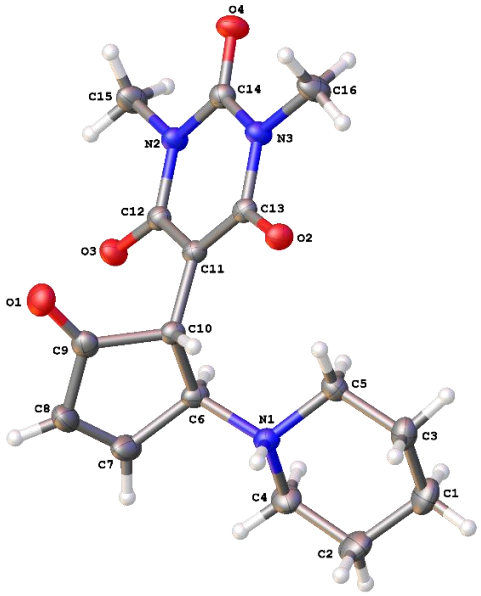

*Figure 43. The asymmetric unit of (**D1·unsolv**) at 150 K.*

The intermolecular interactions in this crystal and how it packs without solvent are fundamental in understanding the different properties between these solvatomorphs. The lack of solvent in this sample structure means that the crystal packing will be different from that of the previously discussed phase (**D1·1.5H$_2$O**), with the intermolecular interactions that govern the structure different too. The cyclised DASA stacks together in a head to tail fashion by hydrogen bonding, with nitrogen (N1) cation acting as a donor and barbituric acid oxygen (O2) acting as an acceptor. The dimers formed are symmetrical with an inversion centre in the middle. Hydrogen bonding occurs within the dimers of **D1**, but O-H/H-O contacts are also prevalent between dimers. Figure 44, shows the direction of these interactions extending along the *a*-axis. Detailed information regarding these bonding interactions is displayed in Table 8.

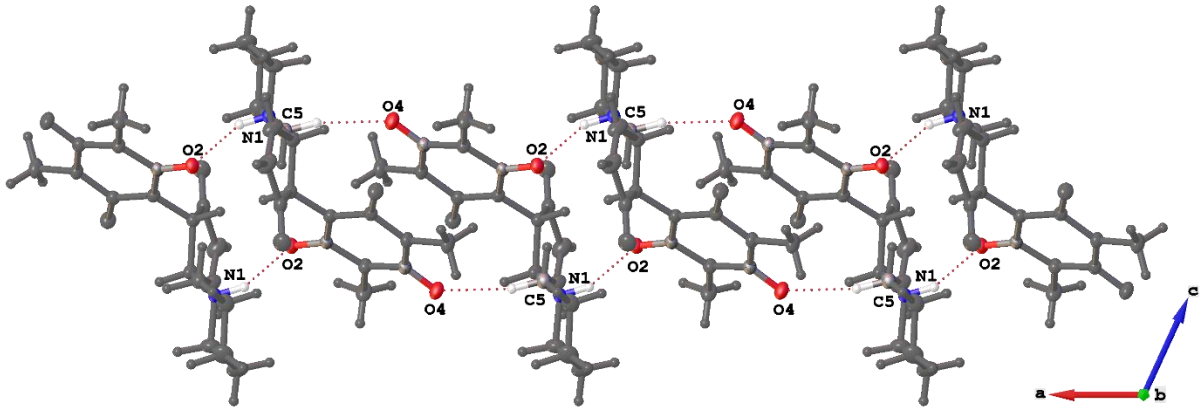

Figure 44. The inter/intra dimer hydrogen bonding along the a-axis at 150 K.

Table 8. A summary of values associated with hydrogen bonding in D1·unsolv at 150 K

Bond	H-acceptor distance/ Å	Donor-acceptor distance/ Å	Bond angle/ °
O2 ··· H – N1	1.88458(6)	2.7194(8)	153.0850(18)
O4 ··· H – C5	2.30193(7)	3.23166(10)	160.4084(8)

The dimers are held together by two symmetrically equivalent hydrogen bonds. These bonds are much shorter than those that extend between dimers suggesting that the dimerisation, which is a common driving force for crystallisation,[139] is stronger than the forces between them. The shortest intermolecular interaction within the (**D1·unsolv**) system is this hydrogen bond between the dimers, whilst the (**D1·1.5H_2O**) system has shorter and more linear hydrogen bonds resulting in larger, more stable crystals.

Although unlikely to be considered a hydrogen bond, this (O4···H – C5) interaction between dimers causes the formation of these dimer columns that extend in the *a*-direction. Controversy[88] lies with whether an O-H-C contact can be labelled as a hydrogen bond, and although this carbon is bonded to nitrogen (O···H-CN), the validity of such classification is still disputed, as discussed in section 1.3.2 of the introduction. Regardless, this contact is a significant interaction between the dimers and can be observed as a close contact using Hirshfeld surface analysis.

Figure 45 shows a (**D1·unsolv**) dimer formed by hydrogen bonds crosslinking the molecules in a head to tail fashion. These interactions' significance is indicated by the shortness of this contact depicted

by the dark red spots on the Hirshfeld d_{norm} surface, along with the sharp features representing the OH contacts on the fingerprint plot.

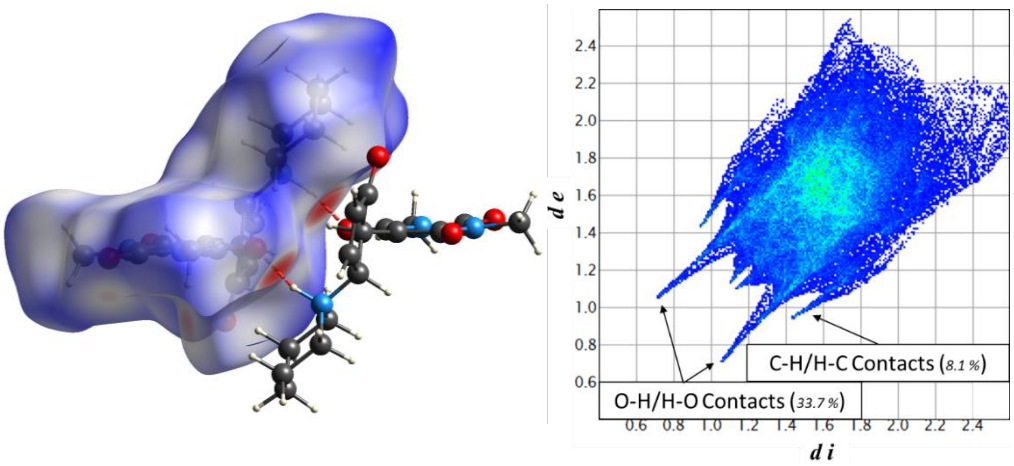

Figure 45. the Hirshfeld surface analysis of the unsolvated form and a fingerprint plot summarising the surface interactions displayed by the surface.

Inspection of the fingerprint plot reveals numerous O-H/H-O contacts implied by the short distance of these contacts and their abundance in the system (33.7 %) represented by the lighter blue colour on the plot. This suggests that these interactions are the governing forces holding these molecules together with the weaker dispersive H-H interactions that make up 53.3 % of the surface contacts. The forces between the two molecules in the dimer are seemingly apparent due to their high strength. By modelling the interactions between the dimers instead of individual molecules, interactions exclusively between dimers can be observed without being overshadowed by the strong, obvious hydrogen bonding within the dimer.

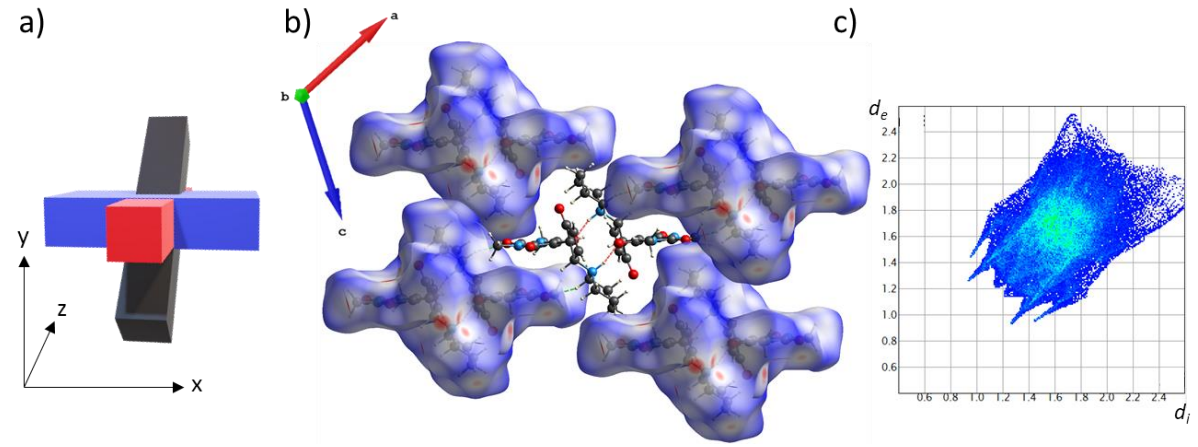

*Figure 46. a) The simplified structure of a (**D1·uslov**) dimer with the barbituric acid rings in blue, cyclopentanone group in red, and piperidine ring in black. b) Hirshfeld surfaces (d_{norm}) around the dimers illustrating interdimer contacts and packing of the ab-plane of (**D1·unsolv**) with contacts summarised in c) a fingerprint plot.*

The dimers resemble 3D plus(+) signs, known for having good packing density considering their aspherical shape. [140,141] With an inversion centre at the centre of the dimer, barbituric acid groups, form a horizontal x-plane with a vertical y-plane made up of piperidine rings and z-plane from cyclopentanone rings. The dimer can then pack along crystallographic planes using interactions between each of these groups.

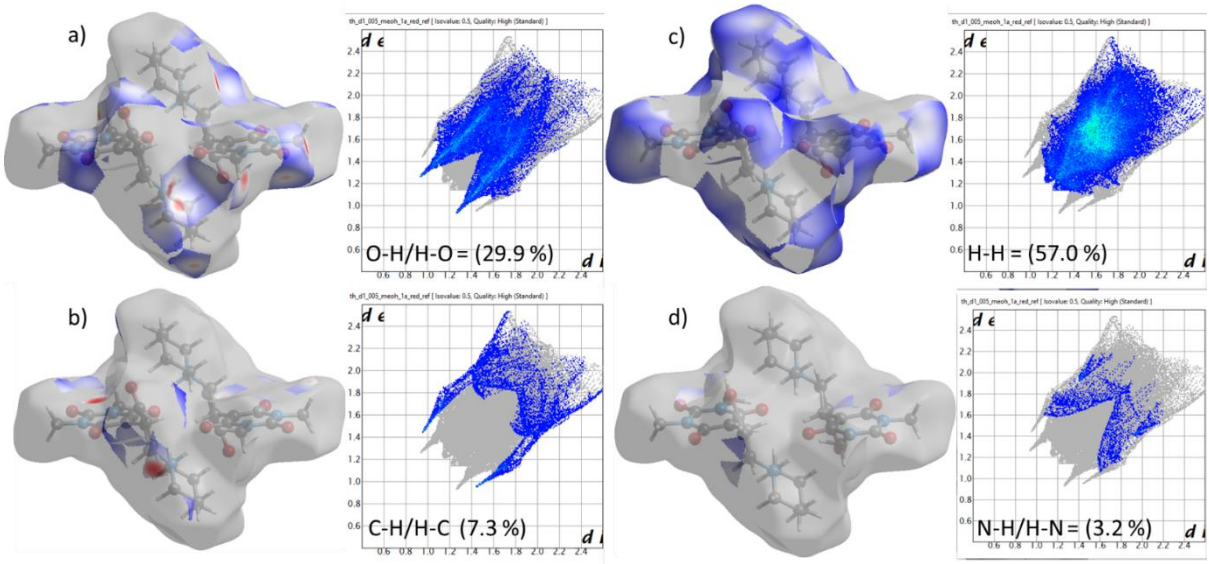

Figure 47. Filtered d_{norm} surfaces and fingerprint plot showing the contacts for a) OH/HO b) C-H/H-C c) H-H and d) N-H/H-N.

Figure 47a shows the H-O contacts and reciprocal contacts between the dimers, between the oxygen (O4) on the barbituric acid ring and the hydrogen-bonded to the carbon (C5) on the piperidine ring. This is also displayed in Figure 44, showing how the dimers pack along the *a*-direction. The fingerprint

plot colour shows that O-H contacts and their reciprocals are prevalent within this structure, second only to H-H interactions.

The d_{norm} surface also shows a slightly longer contact between the oxygen (O1) on the cyclopentanone with hydrogens bonded to carbon (C4) on the piperidine ring and the carbon (C7) on the cyclopentanone. The oxygen (O3) on the barbituric ring is also able to form O-H-C contacts, along with the nitrogen (N2), resulting in a range of (O1/O3/N2···H-C4/C7) contacts. Interestingly, the hydrogen bonded to the carbon (C7) has a shorter contact distance to the carbon (C12) than to its neighbouring oxygen (O3) and nitrogen (N2) atom on the barbituric ring and can be observed as a red region on the Hirshfeld surface, Figure 47b. This is significant as the hydrogen atom is preferentially in contact with a carbon atom rather than an oxygen atom. This contact is also the same interatomic distance (within ESD) as the (O1···H-C7/C4) contacts. The (C12···H-C7) contact is also the second shortest C-H/H-C contact after the previously discussed (O4···H-C5) contact.

This hydrogen (C7) proximity to a heavily polarised sp^2 hybridised carbon (C12) – stemming from it being part of a conjugated ring adjacent to electronegative elements - is likely why this interaction occurs. This produces a (C12···H-C7) contact commensurate with the (C7···H-O1/O3) contact suggesting it is more of an interaction than just proximity. This could also possibly be stabilised and strengthened by the combined intermolecular contacts able to be formed with local oxygen (O1) atoms. This is shown in Figure 48 with associated information concerning intermolecular forces in Table 9.

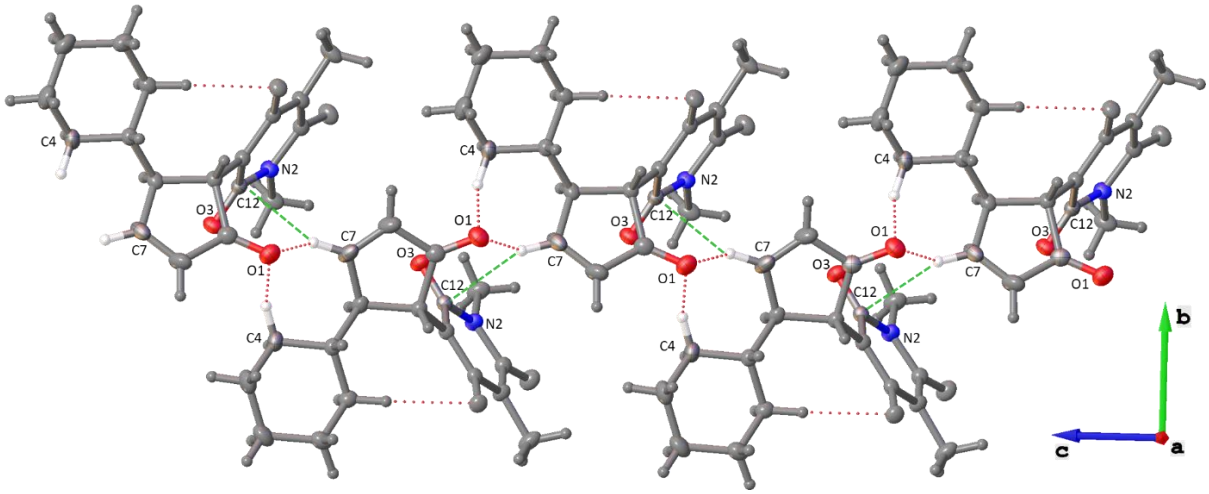

*Figure 48. Intermolecular interactions between **D1** dimer halves extending the structure along the c-direction.*

Table 9. Interatomic distances and angles at 150 K

Atom labels	Intermolecular bond distance/ Å	Donor-acceptor distance/ Å	Angle/ °
C12 ··· H – C7	2.49(2)	3.3666(18)	149.2(15)
O1 ··· H – C7	2.447(19)	3.1180(17)	125.9(15)
O1 ··· H – C4	2.491(18)	3.2844(18)	137.0(14)
O3 ··· H – C7	2.753(19)	3.6503(17)	153.6(15)
O3 ··· H – C4	2.627(18)	3.4721(16)	143.6(14)
N2 ··· H – C7	2.740(19)	3.3140(12)	118.3(14)

The (C12···H-C7) contact is one of the most linear but does not have the longest donor-acceptor distance, again suggesting that all three of these interactions are of comparable significance to the overall packing. This is notable when comparing the fingerprint plot for the dimer interactions, Figure 46b, against the fingerprint plot for a single **D1** molecule, Figure 45b. Looking at both reciprocal O-H and C-H contacts, the $d_{i/e}$ values are similar for the dimer, whilst for the molecule, the O-H contacts dominate.

The carbons (C4, C7) also form interactions with the oxygen (O3) neighbouring the carbon (C12), part of the barbituric ring. It would be expected that these contacts would be shorter due to the fact that oxygen is more electronegative than carbon. Both contacts concerning the oxygen (O3) are significantly longer than the (O1···H-C7/C4) and (C12···H-C7) contacts and so, although present and contributing to the total percentage of contact types, these interactions can be considered weaker.

The dimers also pack along the *b*-direction. An inverted symmetrical equivalent of Figure 48 can be layered above and below it to complete the dimers and extend the structure along the *b*-direction. From the inversion centre in the middle of the dimer, this alternation results in layers of **D1** molecules, producing planes of parallel barbituric acid rings along the *a*-axis with the alternating layers rotated 115 ° around the *a*-axis, as seen in Figure 49.

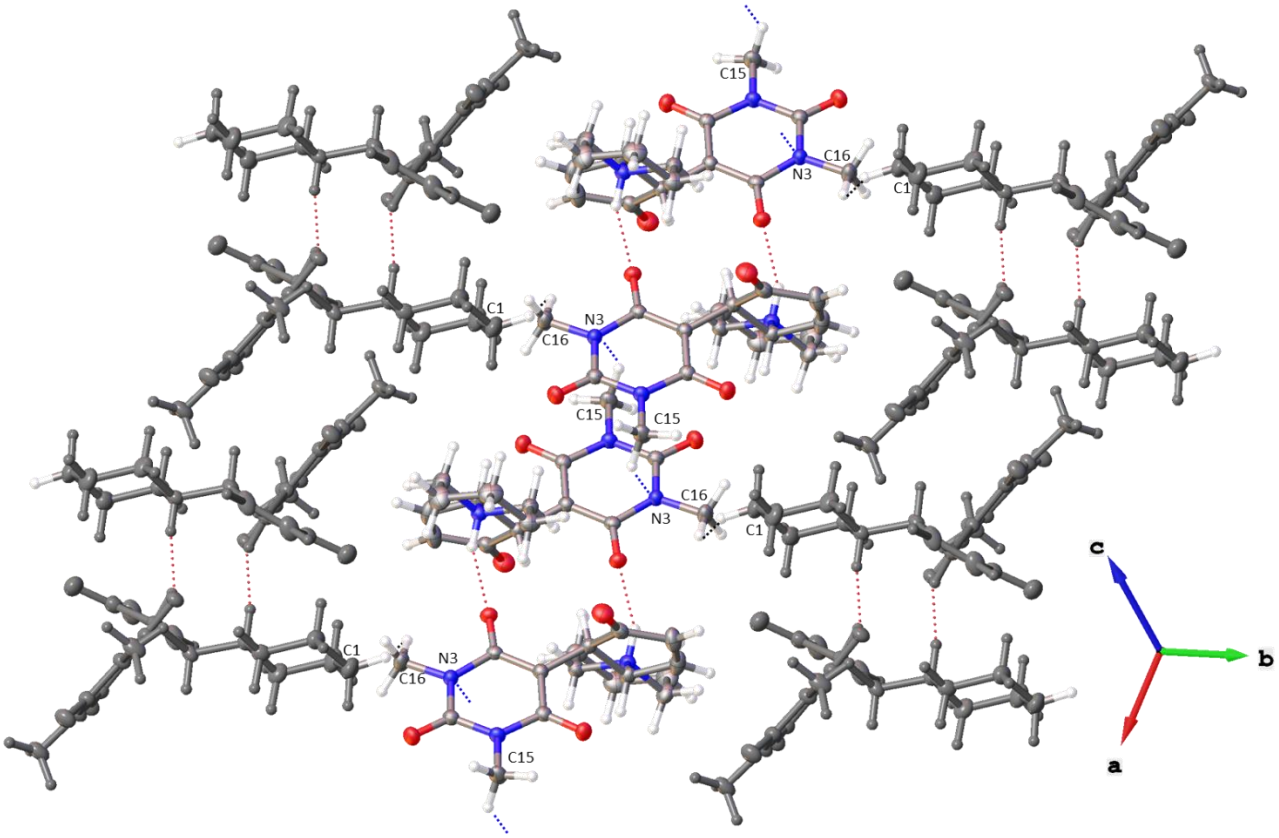

*Figure 49. A view of the packed crystal structure of (**D1·unsolv**) along the (111) direction at 150 K showing the alternating dimer layers within the lattice with sites of short H-H contacts between layers.*

Table 10. Interatomic distances and angles for intermolecular interactions between (D1·unsolv) dimers at 150 K

Atom labels	Contact Distance/ Å	Donor-Acceptor Distance/ Å	Angle/ °
N3 ··· H – C15	2.944(19)	3.5960(16)	124.9(15)
C1 – H ···H – C16	3.17(15)	N/A	N/A

With dimers packing along the *a*-axis, Figure 44, from the dimerization and (O4···H-C5) contact, this gives a slight overlap of the barbituric rings between the dimers. Looking at the Hirshfeld surface, there are no significant interactions exclusively between the barbituric acid rings other than N-H contacts, Figure 47d. There are some dispersive N-C interactions, but these constitute <1 % of the total

number of interactions and, at ~3.5 Å, are likely only a few weak van der Waals interactions. The (N3···H-C15) contact between one nitrogen (N3) and one of the methyl (C15) groups on the barbituric ring is an additional interaction along the *a*-axis.

The intermolecular interactions between the rings include van der Waals interactions between them but also because there is a degree of polarisation from the electronegative nitrogen, which could induce a semi-permanent dipole in the form of N-H contacts. This would make the intermolecular forces between these rings stronger than if there were only van der Waals forces. N-H contacts only make up 3.2 % of the surface contacts, as shown by Figure 47d, including these inter-ring contacts, along with the previously discussed (N2···H-C7) contacts.

The H-H interactions from the methyl (C16) groups of the barbituric acid seem to be the shortest cross-layer interaction at 3.17(15) Å, interacting with the hydrogens (C1) on the piperidine ring, the black dotted lines on Figure 49. These interactions are what constitute the wing-like features of the fingerprint plot in Figure 47c. Although the H-H contacts are not the shortest, they are the most numerous in the structure at 57.0 % and so are considered one of the governing forces for the packing of this crystal structure. However, due to their discursiveness, they have no considerable directionality, unlike other contact types, except for the cross-layer interactions.

In summary, in the absence of solvent molecules in the lattice, the **D1** molecules dimerise in a head to tail fashions via strong hydrogen bonding and pack along the *a*-direction via C-H contacts forming columns. These columns then pack in alternating layers along the *bc*-plane at ~115 °(β) to each other. This results in a close packing with extensive intermolecular interactions holding it together.

3.2.4 Variable temperature studies

Figure 50 shows the non-uniform expansion of the (**D1·unsolv**) unit cell with detailed information in **Error! Not a valid bookmark self-reference.**. This crystal has the lowest percentage thermal expansion of all the solvatomorphs. With the hydrogen bond (O2···H-N1) between the dimer almost parallel to the *c*-direction, it is no surprise that this is the direction that has the least thermal expansion due to this intermolecular interaction being the strongest in the system. The *b*-direction mostly relies on dispersive interactions, with the most substantial interactions in that direction being (O1/O3···H-C4) with the (C12···H-C7) contact having an equal effect on both the *b* and *c*-direction. The *c*-direction also has the (O1/O3···H-C7) which are similar in strength to those in the *b*-direction along with intermolecular forces between adjacent barbituric acid rings. The strong hydrogen bonding within the dimer does also affect the *a*-direction, but where this direction expands will be the (O4···H-C5) contact, which when not considering hydrogen bonding, is the strongest intermolecular force in the crystal.

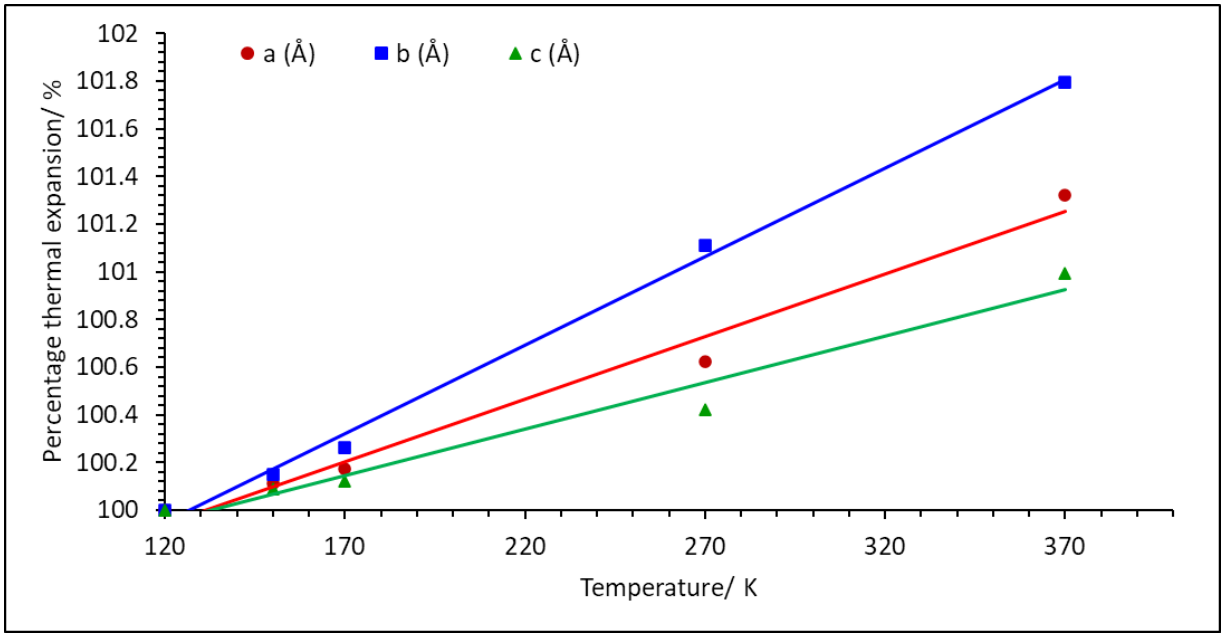

*Figure 50. The percentage change in unit cell parameters with increasing temperature for (**D1·unsolv**).*

Table 11. The unit cell parameters for (D1·unsolv) with varying temperature obtained through SCXRD

Collection temperature/ K	a/ Å	b/Å	c/ Å	β/ °	Cell volume/ Å^3
120	10.2423	13.8721	11.9886	114.472	1550.3
150	10.2539	13.8928	11.9994	114.639	1553.75
170	10.2602	13.9086	12.0031	114.584	1557.6
270	10.3063	14.02616	12.0393	114.881	1578.3
370	10.3778	14.1209	12.1078	115.139	1606.3

Table 12 shows the changes in the intermolecular distance with increasing temperature. The first observation is that the two strong hydrogen bond (O2···H-N1) lengths between the dimers are all equivalent within error for all temperatures. This means the dimers continue to stay intact, and any expansion of the crystal occurs through the lengthening of other interdimer contacts. Looking at the (O4···H-C5) contact, along the *a*-direction, an increase of 1.15 % is observed, which is in line with the observation for the unit cell parameters in Figure 50.

Table 12. changes in the bond lengths and angles of intermolecular contacts with temperature for (D1·unsolv)

Collection Temperature/ K	O2···H-N1 /Å	O2···H-N1 /°	O4 ··· H-C5 /Å	O4 ··· H-C5 /°
120	2.719(3)	146.46(17)	3.226(4)	156.4(2)
150	2.7195(13)	153.1(14)	3.2317(15)	160.4(13)
170	2.719(3)	147.72(14)	3.236(3)	157.11(18)
270	2.723(3)	150.28(16)	3.250(4)	158.8(2)
370	2.717(4)	153.49(18)	3.263(4)	160.6(3)

With no solvent in the crystal to disrupt the crystal packing before melting occurs, no solid-state switching was observed in (**D1·unsolv**). Due to minimal sample yields from this crystallisation, bulk sample properties were unable to be characterised thoroughly by means of PXRD, grinding experiments and humidity experiments.

Production of solid-state thin films produced from the evaporation of **D1** from methanol did appear to switch in the solid-state in response to light, as can be seen qualitatively in Figure 51. This shows a film produced by the evaporation of a **D1** solution in methanol on a glass substrate and then thermally switched in the oven at 80 °C. The film was then placed under white light in ambient conditions for

~72 hours, and decolouration was observed for the thinner regions of the inhomogeneous film. This was further observed to be thermally reversible. Unfortunately, there was no time to explore this path further but would definitely be a focus on future work. Developing the production of these films via spin or dip coating for homogenous thickness and observing any changes in surface morphology with switching via scanning electron microscopy. This could open avenues to applications similar to the amorphous films of diarylethenes that have been used as high-density optical storage devices.[142]

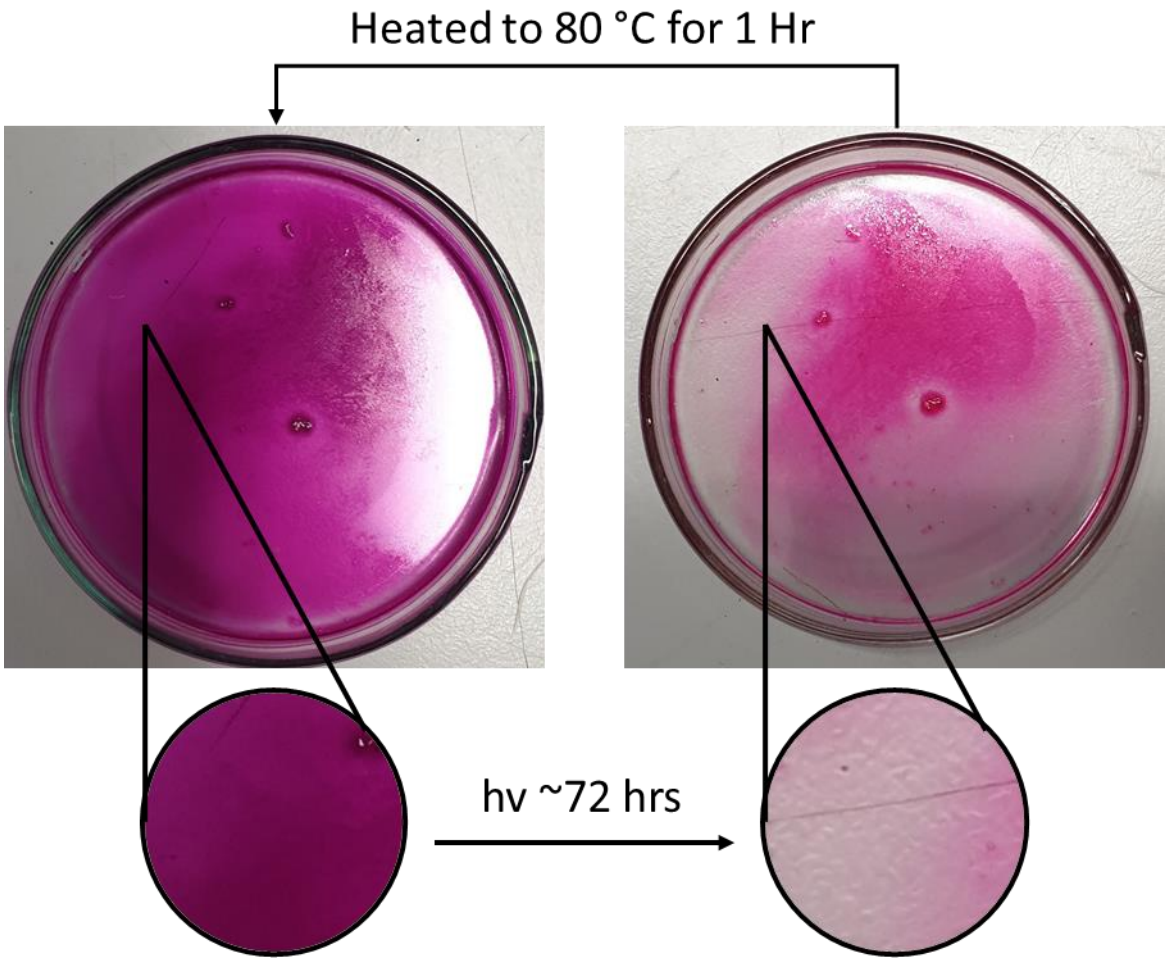

*Figure 51. A thin film of **D1** produced via evaporation of a **D1** solution in methanol. After ~72 hours under white light, decolouration was observed, which was thermally reversible by placing the film in the oven at 80 °C for 1 hour.*

3.3 Dichloromethane Solvates; (**D1·1.5DCM**)

The samples crystallised from dichloromethane were smaller than the (**D1·1.5H_2O**) crystals but larger than the (**D1·unsolv**) crystals. The sample produced from DCM was not stable in ambient conditions, as it disintegrated to a purple solid after several days. An example of this is shown in Figure 52, where

the formation of cracks in the crystal appears in ambient conditions, turning purple at the freshly exposed surfaces throughout the crystal. If left long enough, the crystal completely switches from colourless to purple, with cracks in the crystal becoming visible. Due to this instability at room temperature, it was impossible to perform analyses such as TGA & DSC and PXRD.

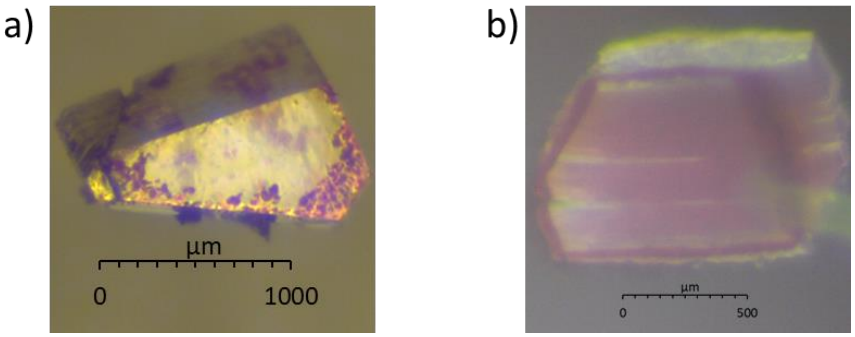

*Figure 52. Solid-state switching of (**D1·1.5DCM**) in ambient conditions, with a) a fresh, clear colourless crystal starting to crack and b) a different single-crystal that has completely degraded to a purple solid after removal from the mother liquor for a few days.*

3.3.1 Crystal packing; SCXRD with complimentary Hirshfeld Surface Analysis

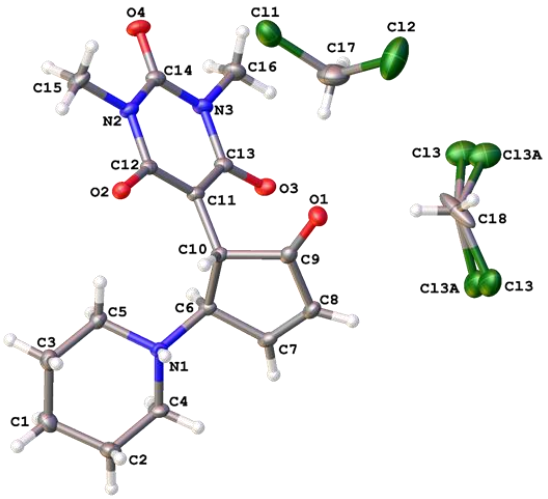

*Figure 53. The asymmetric unit of (**D1·1.5DCM**) at 120 K.*

The asymmetric unit of (**D1·1.5DCM**) is shown in Figure 53. The presence of dichloromethane molecules in this crystal structure is a key difference between this solvatomorph and those previously discussed. The sample crystalised in the same space group as the (**D1·1.5H_2O**) sample, and the empirical formula has the same ratio of DCM molecules to **D1** molecules, but the crystal structures are not isostructural. Interestingly, the **D1** isomer that crystalises from the chlorinated solvent is the cyclised zwitterionic form even though the solvatochromism of first-generation DASAs heavily favours

the linear triene form in these solvents, with limited photoswitching occurring. The solvent disorder was modelled for DCM (C18) but not for DCM (C17) due to the complexity of the disorder and its negligible effects on the crystal packing. This was due to the low occupancy of the alternative position, so ADPs were deemed as appropriate in handling this aspect of the model.

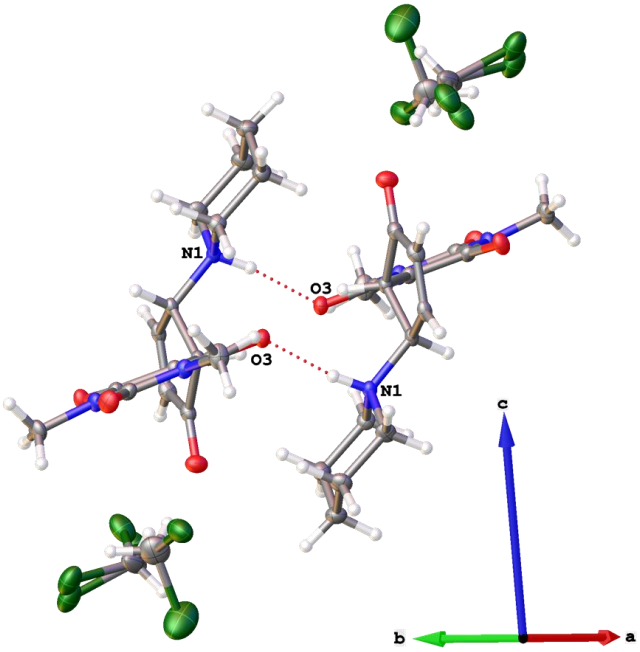

*Figure 54. Dimers of (**D1·1.5DCM**) at 120 K viewed down the (1 1 1) direction with inter-dimer hydrogen bonding highlighted.*

Like the (**D1·unsolv**), this solvatomorph forms dimers with strong hydrogen bonds linking the **D1** zwitterions in a head to tail fashion. This gives the same shape dimer as before with the inversion centre in the middle, resulting in a plane of barbituric acid rings with perpendicular planes of piperidine rings and cyclopentanone rings. The key difference here is the presence of DCM surrounding the dimer.

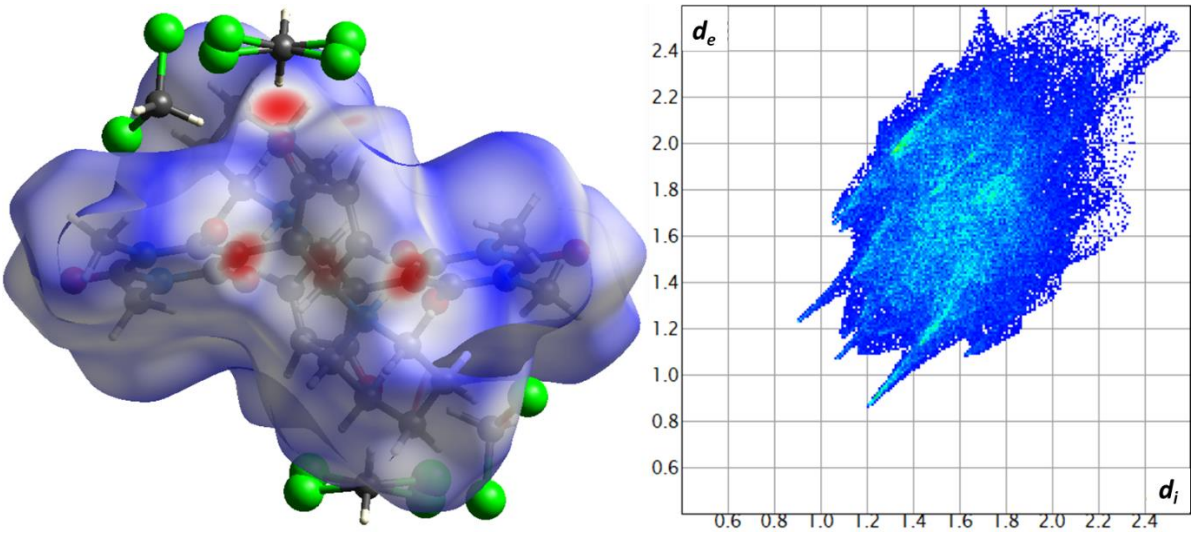

*Figure 55.The Hirschfeld d_{norm} surface of the (**D1·1.5DCM**) dimer at 120 K and accompanying fingerprint plot.*

The d_{norm} Hirshfeld surface was modelled for the dimers of **D1** in this structure to observe the interactions between dimers and between solvent and dimers; this is displayed in Figure 55 with the complimentary fingerprint plot summarising the surface contacts. This is different from fingerprint plots seen before as it is not symmetrical across the diagonal. The pseudo-symmetry of these plots is a consequence of the assumption that the crystals looked at via this method only contain a single molecule.[126] Here, the introduction of the dichloromethane means that d_e(Cl)-d_i contacts can occur and distances can be calculated, but d_e-d_i(Cl) contacts cannot exist because there are no chlorine atoms present within the DASA dimer. The Hirshfeld surface is filtered to discriminate between individual contact types with their locations upon the surface displayed along with the total percentage of the surface such interactions cover, this is shown in Figure 56.

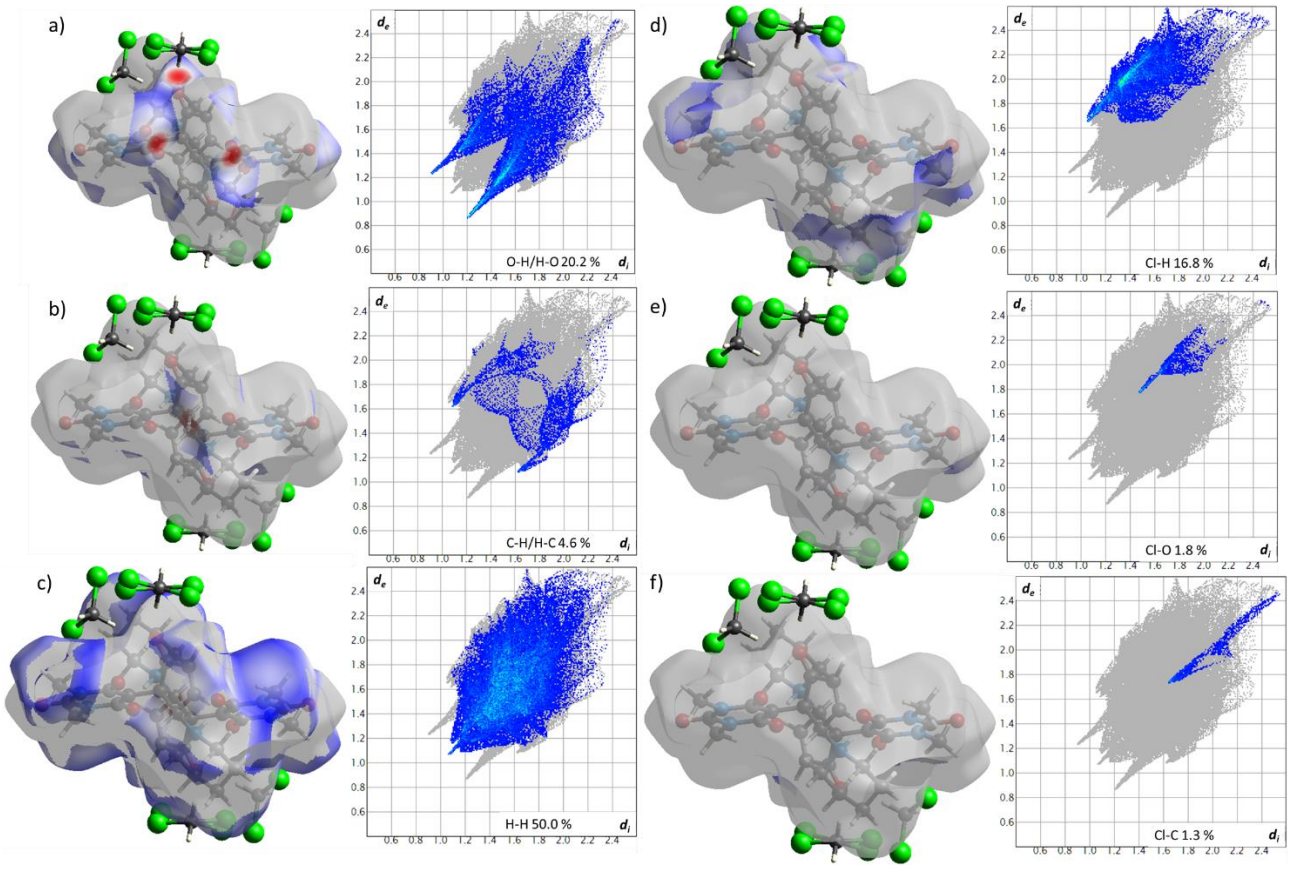

*Figure 56. Filtered Hirshfeld surfaces to show individual contact types between (**D1·1.5DCM**) dimers and solvent at 120 K.*

The O-H/H-O contacts locations shown in Figure 56a and represented by sharp features on the fingerprint plot are the shortest contact types of all the intermolecular contacts present. By looking at the colour of the lower sharp feature of this plot, the colour is a much lighter blue indicating d_e(H)-d_i(O) are more frequent than d_e(O)-d_i(H). This asymmetry suggests that the dimer forms O-H contacts from non-dimer hydrogen atoms, which is likely as looking at the surface, red spots between the oxygen (O1) on the cyclopentanone group and the hydrogens bonded to DCM carbons (C17, C18) are visible. By extending these contacts, we see that the dimers are bridged together via one of the DCM (C18) environments. This crystallographic environment is also situated on a symmetry element and shared between two dimers, so is the reason the empirical formula is not an integer. The second DCM (C17) environment coordinates to the same oxygen (O1) atom, which is chemically sensible as the oxygen (O1) atom is sp^2 hybridised, π-bonded to the adjacent carbon (C9), with two lone pairs able to form intermolecular interactions at the observed geometries. The extension along the *c*-direction is displayed in Figure 57, with detailed information for O-H/H-O contacts presented in Table 13.

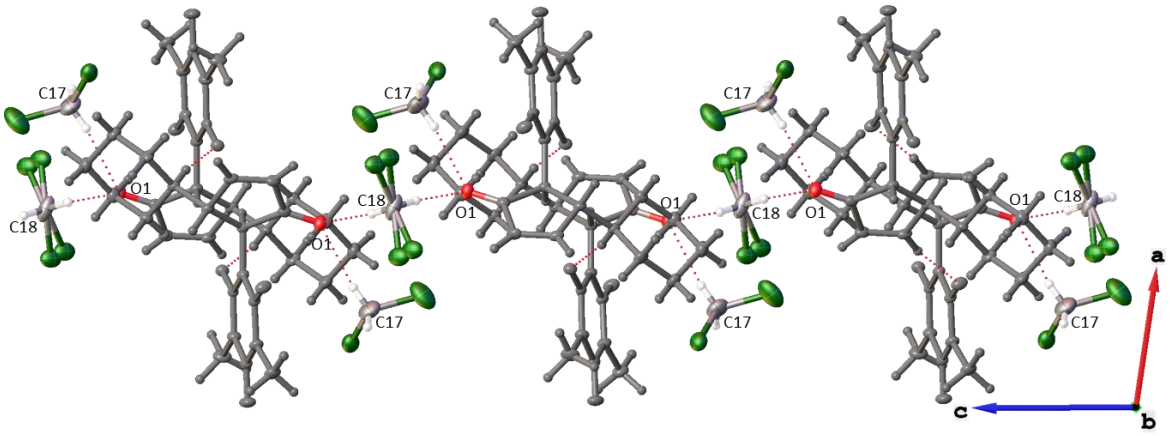

*Figure 57. The crystal Packing of (**D1·1.5DCM**) along the c-direction at 120K.*

Table 13. (D1·1.5DCM) interatomic distances between oxygen and hydrogen at 120 K

Atom labels	Distance/ Å	Donor-acceptor distance/Å	Angle/ °
O2 ··· H – N1	1.81(3)	2.6936(17)	169(2)
O1 ··· H – C18	2.26(3)	3.170(2)	173(3)
O1 ··· H – C17	2.30(4)	3.163(3)	170(3)
O3 ··· H – C7	2.30(2)	3.2190(18)	170.5(18)
O3 ··· H – C4	2.67(2)	3.350(2)	128.6(16)
O4 ··· H – C8	2.80(2)	3.5325(19)	135.8(16)

Both O1···H-C17/C18 contacts are equivalent within error and are short and linear enough to be considered intermolecular bonding interactions. This, coupled with the fact the hydrogen is bonded to carbon with two large electronegative elements bonded to it, suggests that there is sufficient polarisation for this to be the case. The donor-acceptor distance is slightly shorter for DCM (C18), and since this is the solvent molecule bridging two dimers together, then it is considered that this solvent molecule is more tightly held within the crystal structure. This is because it forms two O···H-C contacts whilst the DCM (C17) only seems to form one. Table 13 also includes the hydrogen bond within the dimer, which, as expected, is short and linear, so considered a strong hydrogen bonding interaction.

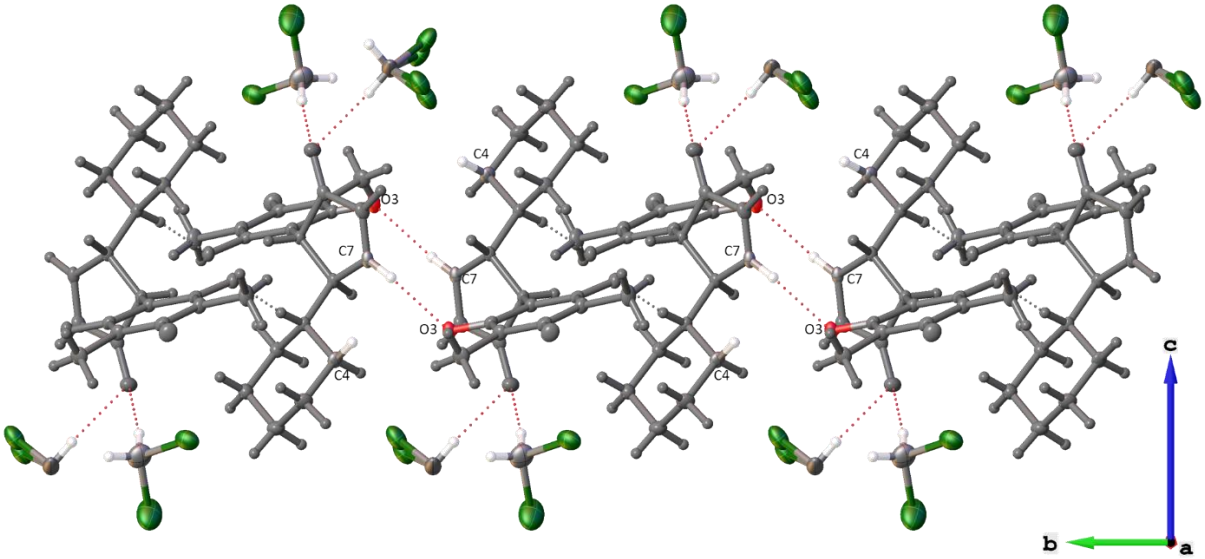

*Figure 58. A view of (**D1·1.5DCM**) interdimer contacts along the b-direction at 120 K.*

Similar to the (**D1·unsolv**) structure, the dimers fit together by forming symmetrically equivalent contacts between the oxygen (O3) on the barbituric ring and a hydrogen bonded to carbon (C7) on the cyclopentanone core. This bond is of the same strength and linearity as the bonding interactions between the dimer and the DCM solvent molecules. Again, a potential driving force for this interaction to occur could be the extension of the conjugation, considering both donor and acceptor groups are involved in π-bonding. Unlike the (**D1·unsolv**) structure, there is no (C12···H-C7) contact present in (**D1·1.5DCM**) crystal packing, and there is little competition from the carbon (C4) on the piperidine ring with the contact (O3···H-C4) distance being considerably longer than the (O3···H-C7) contact. Through these (O3···H-C7) contacts, the crystal structure extends along the *b*-direction.

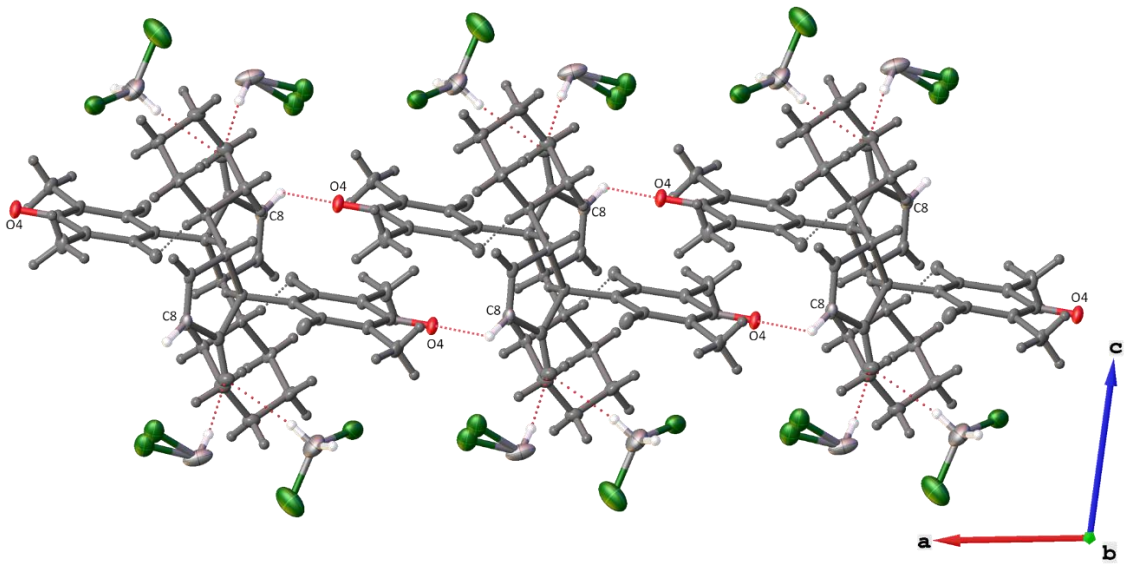

*Figure 59. Intermolecular contacts showing the packing of (**D1·1.5DCM**) along the a-direction.*

Table 14. (D1·1.5DCM) non-hydrogen bonding intermolecular interaction at 120 K

Atom labels	Distance/ Å	Donor-acceptor distance/Å	Angle/ °
C12 ··· H – C16	2.83(3)	3.718(2)	152(2)
C1 – H ··· H – C1	2.28(5)	3.710(4)	N/A
C15 – H ··· H – C7	2.40(3)	3.704(2)	N/A
Cl3 ··· H – C8	2.86(2)	3.680(2)	148.1(16)

The dimers stack with slight ring overlap along the *a*-axis with O-H contacts observed between the oxygen (O4) on the barbituric acid ring and the hydrogen bonded to carbon (C8) from the cyclopentanone group. From Table 13, it can be seen that this (O4···H-C8) contact compared to the others previously discussed is the weakest with the longest donor-acceptor distance and are relatively non-linear.

There are interactions between the rings, presented in Table 14, corresponding to strong van der Waals interactions observable through C-H contacts between the methyl (C16) group and carbon (C12) from partially facing barbituric rings. These interaction types are few in this system, though, at only 4.6 %, as shown in Figure 56b, but this will give stability and strength to the dimer layers along the *a*-axis.

The dispersive van der Waals interactions with the dimers are also fewer than in previously discussed solvatomorphs but still the dominating interaction in terms of frequency. At 50 %, the shortest interaction is between the hydrogens bonded to the carbon (C1) on the piperidine ring tail, furthest from the dimer centre. These bond the dimer *ab*-layers through the solvent layer along the *c*-axis, as well as the DCM (C18) bridges. As this is a short symmetrical intermolecular contact, the fingerprint plot shows this as a sharp feature centred on the diagonal of the plot of Figure 56c.

The other sharp feature on this plot, either side of the centre, corresponds with an H-H contact where one hydrogen is a member of the methyl (C15) group and the other bonded to carbon (C7), part of the cyclopentanone. This interaction is slightly longer than the previous (C1/C15-H···H-C1/C7) contacts discussed. The hydrogen (C7) has also already been established to be involved in an O-H contact with the oxygen (O3). From this, it is possible that the proximity of these hydrogen atoms is either a result of the O-H interaction or offers additional stabilisation for the interaction; the former is much more likely. This is one of the limitations to Hirshfeld surface analysis as not all close contacts can be immediately assumed as bonding interactions.

DCM forms contacts with the dimers, the most prevalent after the O-H are Cl-H contacts that are between the chlorine (Cl3) on the DCM (C18) and the hydrogen (C8) bonded to the cyclopentanone ring. This contact is represented by a faint red spot on the Hirshfeld surface, Figure 56d, and looking at the fingerprint plot; this contact type constitutes 16.8 % of the surface contacts. This is likely because of the electronegativity of the chlorine atoms allowing them to interact with hydrogens by inducing a dipole easily. Chlorine does have some longer contacts with carbon and oxygen, Figure 56e/g, but these do not seem to be anything more significant than directional van der Waals interactions or caused by the atom of proximity from other stronger contacts.

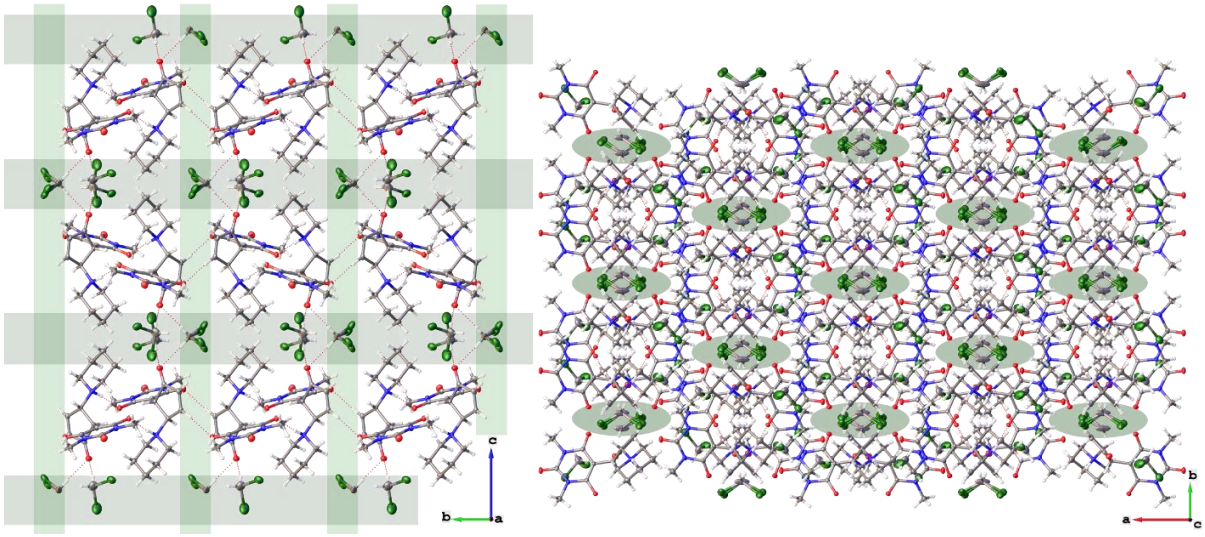

*Figure 60. (**D1·1.5DCM**) at 120 K showing; a) the bc-plane; solvent-dimer layers with alternating rotation of the dimers. Solvent ab-planes are highlighted in green for DCM (C17, C18) along the b-direction and DCM (C18) discrete solvent channels along the c-direction; b) the fully packed crystal structure viewed down the c-axis with the discrete solvent channels highlighted in green.*

Combining the extensions of the crystal structure along the *c*-direction and *b*-direction, the *bc*-plane can be observed, Figure 60a, consisting of layered rows of dimers and solvent. The layering of solvent and alternating dimers forms planes of DCM along *ab*-plane and thinner discrete channels of DCM along the c-direction. These channels are formed when the *bc*-planes stack on top of each other along the *a*-direction, completing the packing of the crystal to give the view displayed by Figure 60b.

3.3.2 Variable temperature analysis

Table 15. Unit cell parameters of (D1·1.5DCM) with varying temperature

Temperature/ K	***a/ Å***	***b/ Å***	***c/ Å***	***β/°***	***Volume/ Å³***
120	18.3955(2)	10.37816(12)	21.8455(3)	98.7826(12)	4121.65(9)
150	18.4119(4)	10.4172(2)	21.8817(6)	98.928(2)	4146.07(17)
170	18.43060(19)	10.38989(11)	21.9975(2)	98.9810(11)	4160.70(8)
220	18.4748(2)	10.40097(12)	22.1655(3)	99.2192(12)	4204.20(9)
270	18.5316(2)	10.41390(13)	22.3542(3)	99.4679(14)	4255.3(1)
280	18.5479(3)	10.41821(15)	22.3903(4)	99.5250(15)	4266.98(11)
290	18.5658(3)	10.42260(18)	22.4303(5)	99.6266(19)	4279.24(14)
300	18.5879(7)	10.4303(5)	22.4795(8)	99.674(4)	4296.3(3)

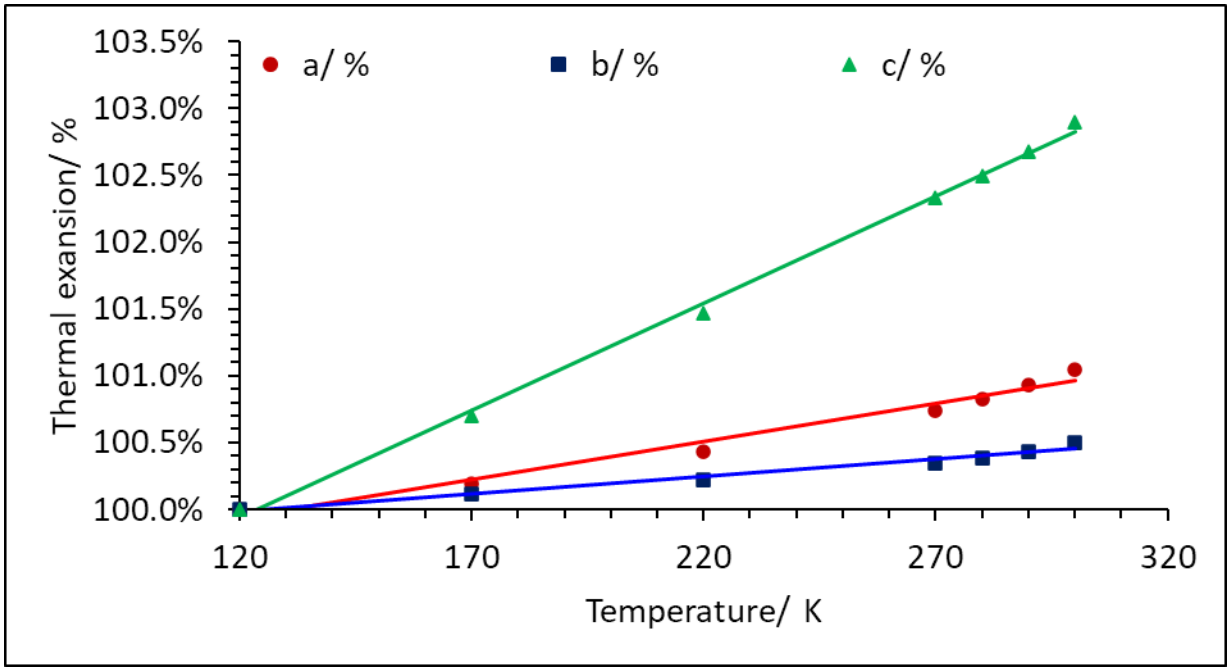

*Figure 61. The non-uniform thermal expansion of the (**D1·1.5DCM**) unit cell.*

The thermal expansion of the unit cell is summarised in Figure 61 from the data in Table 15. This unit cells thermal expansion is the largest observed of all the solvates, with the *c*-direction extending 2.90 %, with the other phases barely reaching half this amount at similar temperatures. The solvent and dimer layers are along the *bc*-plane so extending along the *c*-axis indicates that the distance between the layers increases. This is expected as it is only H-H contacts holding the dimer layers together with DCM (C18) bridges. This could be why, even though the DCM molecules are bonded within the layers and channels, the accessibility throughout the crystal structure means it is easier for the whole crystal to desolvate, as it can do this along all three unit cell directions.

Table 16. Hydrogen bonding within (D1·1.5DCM) at varying temperatures.

Atom labels	*Temperature/ K*	*H-A distance/ Å*	*D-A Distance/ Å*	*D-H-A angle/ °*
O3-H-N1	120	1.81(3)	2.6936(17)	169(2)
O3-H-N1	150	1.77(4)	2.698(2)	169(3)
O3-H-N1	170	1.81(3)	2.6938(18)	169(2)
O3-H-N1	220	1.812719(15)	2.69407(2)	169.10921(19)
O3-H-N1	270	1.796925(17)	2.69262(3)	168.8499(2)
O3-H-N1	280	1.811883(19)	2.69266(3)	170.5642(2)
O3-H-N1	290	1.81988(2)	2.69441(4)	170.2646(3)
O3-H-N1	300	1.81246(6)	2.69642(8)	173.5846(4)

The data in Table 16 for the hydrogen bonding changes within the dimers is minimal compared to the thermal expansion of the unit cell along the *ab*-axes. This must mean that the expansion is due to interactions lengthening between the dimers of the DASA molecules.

If TGA & DSC analysis were able to be performed on this sample, two mass loss events would be expected. The first would be the DCM (C17) environment which has a single strong bonding interaction and two crystallographic directions to vacate the structure (a*b*-plane). A second mass loss would be from the other DCM (C17) environment with two strong intermolecular bonding interactions with **D1** but three directions in which it could vacate the crystal structure by means of the ab-plane and the channels along the *c*-direction. Either of these events could trigger the solid-state switching of the material similar to that of the (**D1·1.5H$_2$O**) solvatomorph.

3.4 Chloroform Solvate; (**D1·1CHCl$_3$**)

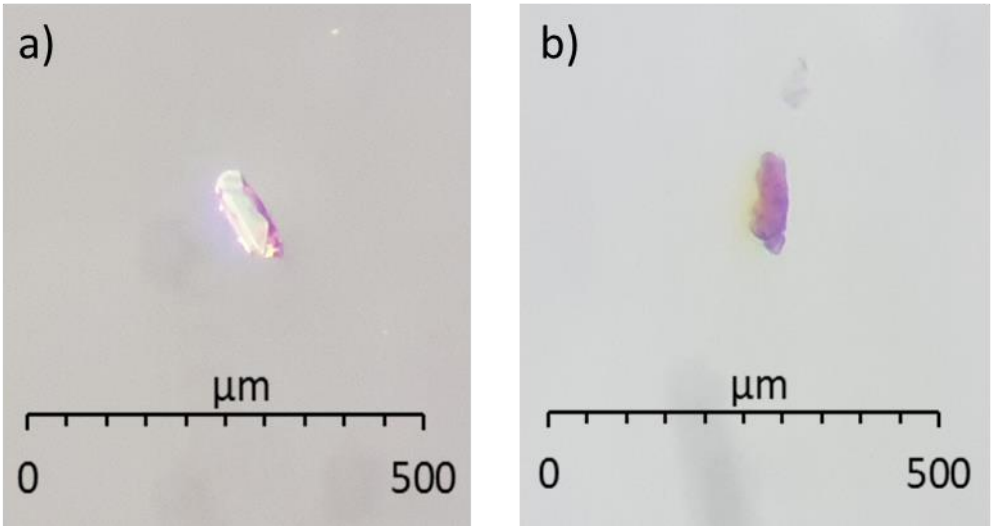

*Figure 62. Images of a (**D1·CHCl$_3$**) single-crystal a) at room temperature pre variable-temperature X-ray diffraction analysis and b) post X-ray diffraction analysis at heights of 300 K.*

Figure 62a shows a clear colourless single-crystal of (**D1·CHCl$_3$**) at room temperature prior to variable temperature X-ray diffraction analysis. The faint pink hue around this crystal's surface should be noted, suggesting the switching process has begun, an indication of the crystal's instability at ambient temperatures and vapour pressures. Figure 62b shows the same crystal after being cooled to 120 K and then slowly ramped to 300 K over a period of 48 hours. This was the temperature limit observable

diffraction data for this crystal could be collected and, on removal from the diffractometer, was observed to have partially disintegrated and switched to a dark pink colour. This is a good demonstration of the solid-state switching of (**D1·CHCl$_3$**).

As with (**D1·1.5DCM**), the stability of this sample in ambient conditions, as well as crystal size and sample a quantity (along with time constraints), imposed limitations on the techniques available for sample analysis. As such, TGA & DSC, reflectivity and PXRD were unable to be obtained for this solvatomorph. Therefore, analysis of this phase is purely crystallographic with complimentary Hirshfeld surface analysis.

3.4.1 Crystal packing; SCXRD with complimentary Hirshfeld Surface Analysis

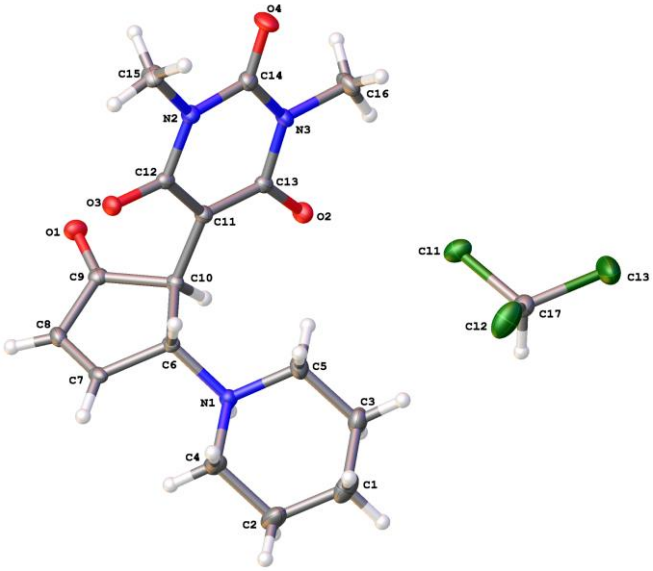

*Figure 63. The asymmetric unit of (**D1·1CHCl$_3$**) at 120 K.*

The asymmetric unit of (**D1·CHCl$_3$**) can be seen in Figure 63, showing the 1:1 ratio of **D1** molecules to chloroform molecules. As with previous phases, the **D1** molecules dimerise, but this crystal structure is not isostructural to any of the other solvatomorphs. Crystallising in the primitive *P-1* space group, the low symmetry, triclinic crystal structure is discussed in-depth, with complimentary Hirshfeld surface analysis shown in Figure 64 and filtered to show individual contact types.

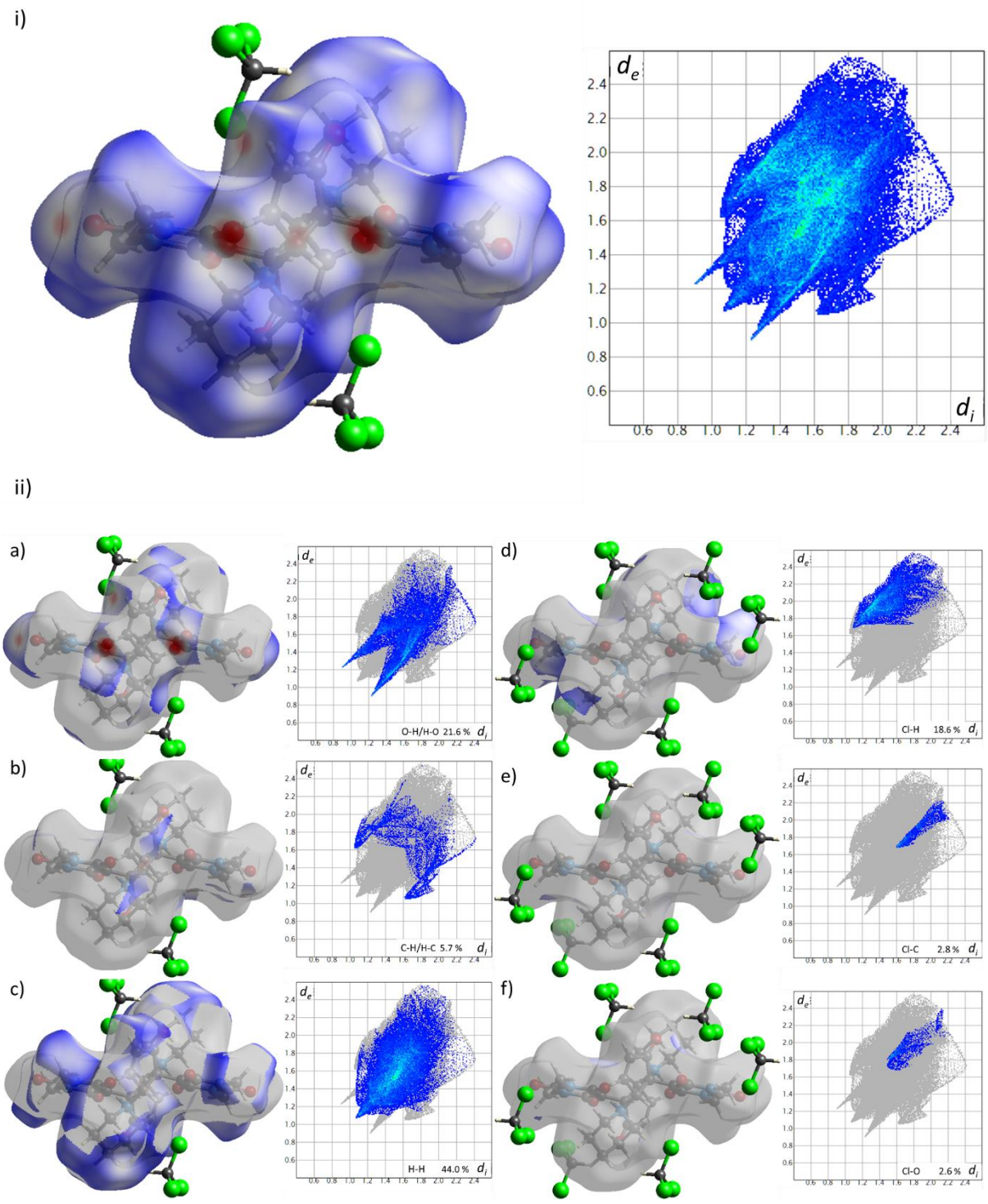

*Figure 64. i) Hirshfeld surface analysis for the (**D1·CHCl$_3$**) dimer with accompanying fingerprint plot. ii) individually filtered surfaces and fingerprint plots showing specific contact types: a) H-O/O-H; b) H-C/H-C; c) H-H; d) Cl-H; e) Cl-C and f) Cl-O.*

The **D1** zwitterions form strong hydrogen bonds between the oxygen (O2) on the barbituric ring and the hydrogen bonded to the nitrogen (N1) cation. The dimers formed then interact via the opposite oxygen (O3) on the barbituric acid ring with the hydrogen bonded to carbon (C7) in the cyclopentanone core of an adjacent dimer. These interactions extend the crystal structure along the

c-axis, as shown in Figure 65, and are among the strongest intermolecular interactions present in the crystal. Detailed information regarding the length and angles of all oxygen-containing contacts is presented in Table 17.

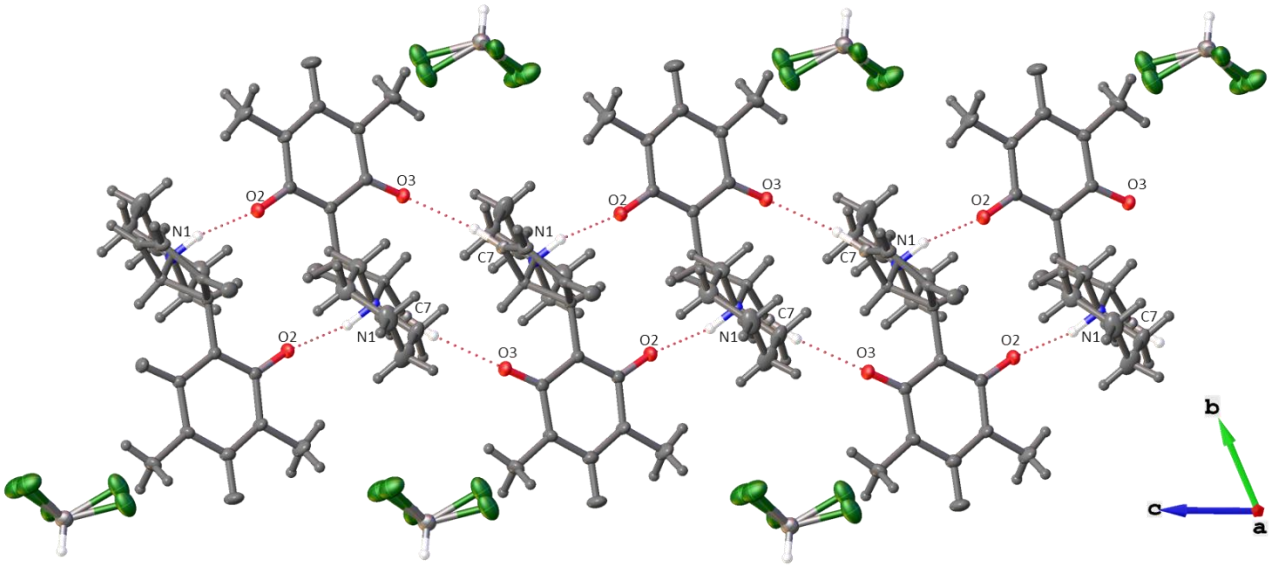

*Figure 65. A view of (**D1·CHCl$_3$**) displaying O-H/H-O interactions along the c-axis.*

Table 17. Interatomic distances and angles for the O-H/H-O interactions between dimers and solvent at 120 K

Atom labels	Distance/ Å	Donor-acceptor distance/Å	Angle/ °
O2 ··· H – N1	1.7454(11)	2.6927(18)	161.48(8)
O3 ··· H – C7	2.3025(11)	3.211(2)	165.42(10)
O1 ··· H – C17	2.3302(12)	3.100(2)	134.81(5)
O4 ··· H – C8	2.5222(12)	3.225(2)	132.60(11)

The O-H contacts also extend the crystal along the *a*-axis, Figure 66, through the oxygen (O1) from the cyclopentanone to the hydrogen on the chloroform (C17). The carbon (C17) is bonded to three electronegative chlorine atoms giving the solvent molecule a dipole with a partial positive charge centred on the carbon (C17). Although the donor-acceptor distance for this interaction is shorter than the interdimer contacts along the *c*-axis (O3···H-C7), the linearity is drastically less, suggesting that this bonding interaction may be weaker than initially perceived.

The O-H/H-O contacts for this system make up 21.6 % of the total contacts between the dimers with a higher number of H-O (13.3 %) than O-H (8.3 %) visualised by the lighter blue colour on the right-

hand side of the fingerprint plot, Figure 64a. This is because the H-O contact from the chloroform can only be formed via external hydrogen to internal oxygen, resulting in the fingerprint plot's asymmetry, as with other solvatomorphs.

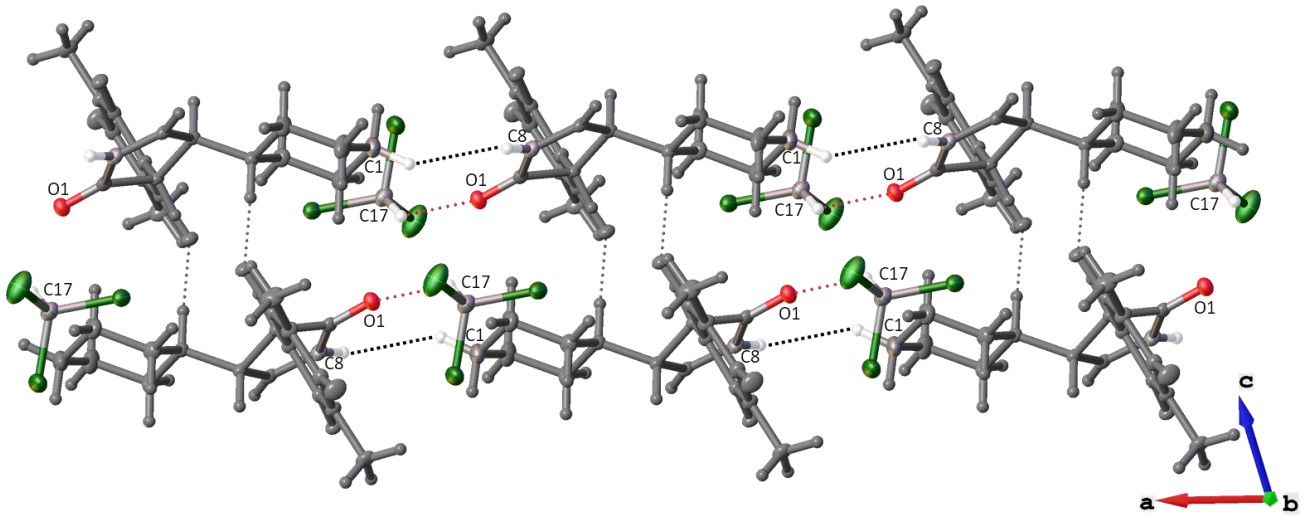

*Figure 66. A view of (**D1·CHCl$_3$**) extending along the a-axis at 120K.*

Using the Hirshfeld surface analysis, Figure 64c, it can be seen that there is an H-H contact extending along the *a*-axis too. This contact type is like that of the previous (**D1·1.5DCM**) crystal structure; it is identifiable on the fingerprint plot and resembled by a dispersive cloud of interactions of various lengths. These are the dominating contacts in terms of frequency, with the shortest contact being a symmetrical (C1-H···H-C1) contact along the *c*-direction. The asymmetric contact between hydrogens attached to carbon (C1) and carbon (C8) extends the structure along the *a*-axis, visible in Figure 66, and are of a shorter donor-acceptor length to the short (C1-H···H-C1) contacts. Details of non-oxygen-containing contacts are displayed in Table 18.

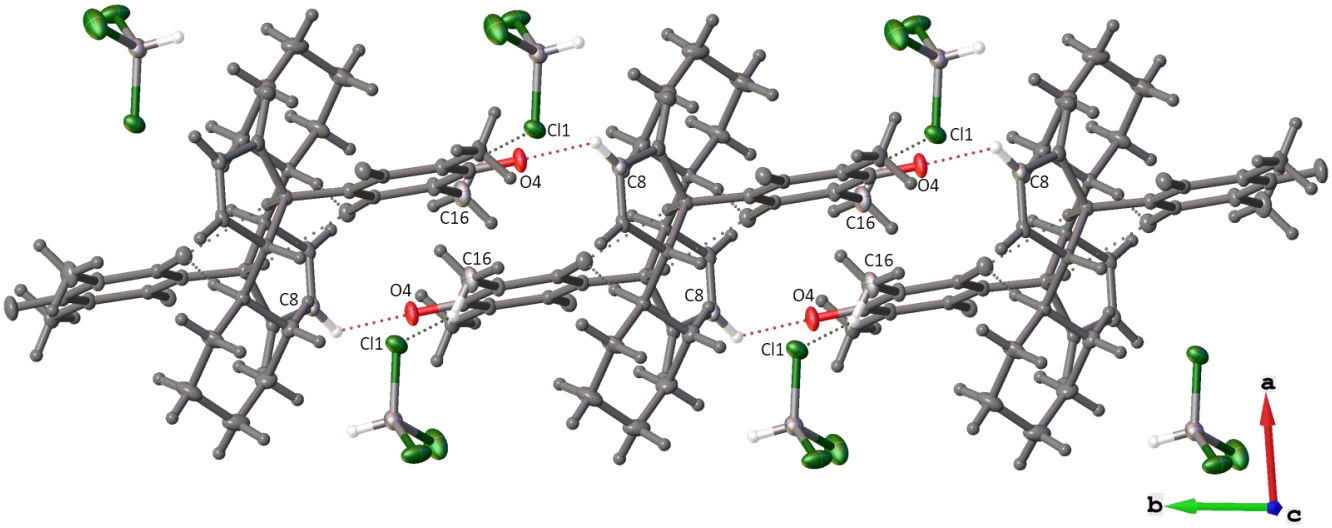

*Figure 67. A view of (**D1·CHCl₃**) extending along the b-axis at 120 K.*

Table 18. Interatomic interactions data for non-oxygen containing contacts within a single-crystal of (D1·CHCl₃) at 120 K.

Atom labels	Distance/ Å	Donor-acceptor distance/Å	Angle/ °
C1 – H···H – C1	2.3627(3)	4.140(4)	N/A
C1 – H···H – C8	2.4309(3)	3.963(3)	N/A
C13 ··· H – C15	2.8121(16)	3.673(3)	149.77(11)
Cl1 ··· H – C16	2.8943(5)	3.5766(19)	128.95
Cl2 ··· H – C15	2.9965(6)	3.6620(19)	127.59
Cl3 ··· H – C1	3.0397(8)	3.713(2)	127.66(12)

The structure extends along the *b*-axis via O-H contacts between the oxygen (O4) on the barbituric ring and the hydrogen bonded to the carbon (C8). This hydrogen (C8) is much more likely to be involved in this interaction than the previously discussed van der Waals interaction (C1-H···H-C8). This O-H contact is the longest of those presented in Table 17. There are other contacts that play a part in the extension along the *b*-direction as the barbituric rings partially overlap like other solvatomorphs. This results in C-H contacts from the hydrogen on the methyl group (C15) interacting with the π-bonded carbon (C13) in the barbituric acid ring. This is the shortest C-H contact type and the most significant signified by the fingerprint plot's sharper features, with others being longer dispersive interactions, displayed in Figure 64b.

The interactions between the solvent and the dimers will be a dictating factor when investigating this crystal structure's desolvation. The strongest intermolecular interaction between the chloroform and

the **D1** dimer is the (O1···H-C17) contact, but unlike the (**D1·1.5DCM**) phase, the chloroform cannot bridge the dimer layers due to only having one hydrogen. The shortest interactions between chlorine and the dimers are Cl-H interactions shown in Figure 64d, with longer interactions between carbon and oxygen shown in Figure 64e-f. These chlorine hydrogen interactions are what hold the dimer layers together along the *a*-axis with contributions from the van der Waals interactions (C1-H···H-C1). This structure can be seen clearly in Figure 68.

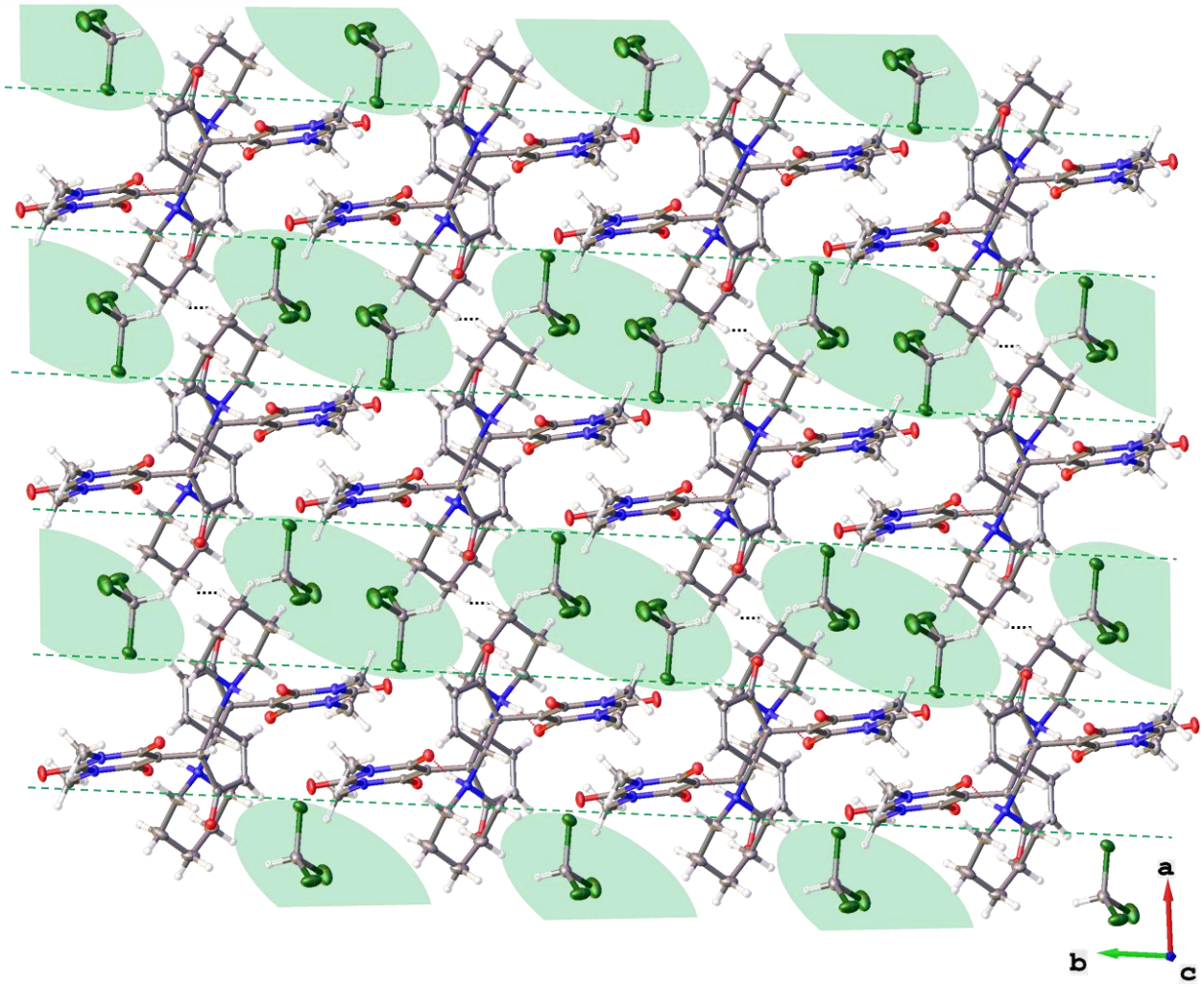

*Figure 68. The ab-plane of the crystal structure of (**D1·CHCl$_3$**) at 120 K with the chloroform layers highlighted and van der Waals interactions between layers identified.*

3.4.2 Variable temperature studies

Table 19. Unit cell parameters of (D1·$CHCl_3$) obtained from variable temperature single-crystal x-ray diffraction experiments.

Temperature/ K	*a/ Å*	*b/ Å*	*c/ Å*	*α/°*	*β/°*	*γ/°*	*Volume/ Å³*
120	10.3490(11)	10.3748(9)	10.6293(10)	63.611(10)	70.16(1)	77.068(8)	958.04(19)
150	10.3622(7)	10.3852(6)	10.6390(6)	63.752(6)	70.317(6)	76.982(5)	962.89(12)
170	10.3743(7)	10.3961(6)	10.6498(7)	63.838(6)	70.404(6)	76.984(5)	967.15(12)
220	10.4085(9)	10.4252(10)	10.6694(11)	64.137(10)	70.694(9)	76.821(8)	978.40(18)
250	10.4407(11)	10.4650(13)	10.6858(14)	71.038(12)	64.277(11)	76.719(10)	989.4(2)
270	10.4617(18)	10.528(2)	10.7048(15)	71.340(17)	64.385(16)	76.515(16)	1001.0(3)
300	10.476(2)	10.598(3)	10.693(3)	71.72(3)	64.66(2)	76.40(2)	1011.7(5)

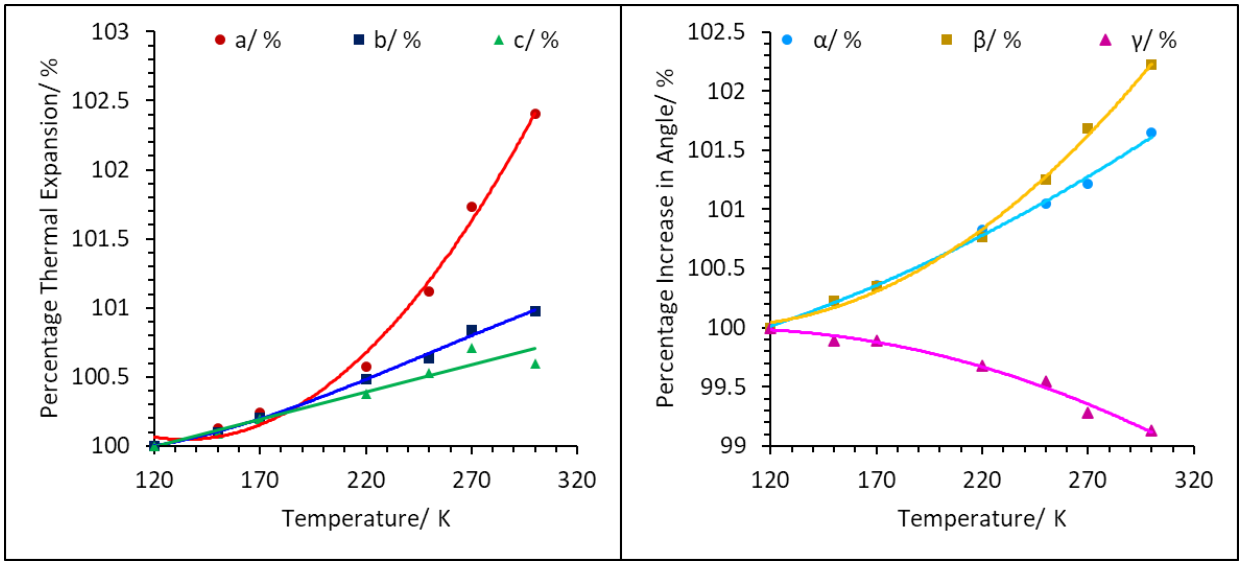

*Figure 69.The change in unit cell parameters with temperature for (**D1·$CHCl_3$**) collected by variable temperature single-crystal x-ray diffraction.*

The weak interactions between the dimer layers are further evidenced by the variable temperature SCXRD data, displayed in Table 19 and summarised in Figure 69. The unit cell's asymmetric expansion, coupled with its distortion, suggests that the intermolecular interactions along each axis are inequivalent in strength. With increasing temperature, the crystal expands preferentially along the *a*-axis. The chloroform molecules reside within the layers perpendicular to the *a*-axis of the crystal structure; this expansion is likely the result of the desolvation or its cause in the first place. This stems from the lack of strong interactions along the *a*-axis, and the fact that the chloroforms are unable to bridge the layers, results in less stable crystals with a likely lower switching temperature.

In summary, the dimers pack in a simple way, with an inversion centre between dimers rather than in the middle of them, which means there are no alternating layers of different dimer orientations like in (**D1·1.5DCM**). The chloroform occupies regions between the dimers co-ordinated to them via a single (Cl_3C-H···O1) interaction and Cl-H and H-H interactions holding the dimer layers together along the *a*-axis. If TGA & DSC analysis were possible, a single mass-loss event would likely occur prior to melting, with the single chloroform environment vacating the crystal structure and initiating the solid-state switching of the material, as seen with the other solvatomorphs.

3.5 Comparison of Solvatomorphs

3.5.1 Void Space Analysis

The switching of the material is a substantial structural change for the solid-state, especially when compared to diarylethenes, and so looking at the available space for such a change to occur in the crystal structure is desirable.

The 18 cubic angstrom rule assumes all atoms are spherical and of equal mass and calculates the average volume of all non-hydrogen atoms within a unit cell to be approximately 18 $Å^3$. This can be used to gain a rough estimate for space within each solvate. This is calculated, by Equation 1, using experimentally determined values from SCXRD. The results for each solvate are displayed in Figure 70.

Equation 1. The 18 cubic angstrom rule, with z being the number of formula units per unit cell.

$$Average\ Atom\ Volume = \frac{Unit\ Cell\ Volume}{Number\ of\ NonH\ Atoms\ \times Z} \approx 18\ Å^3$$

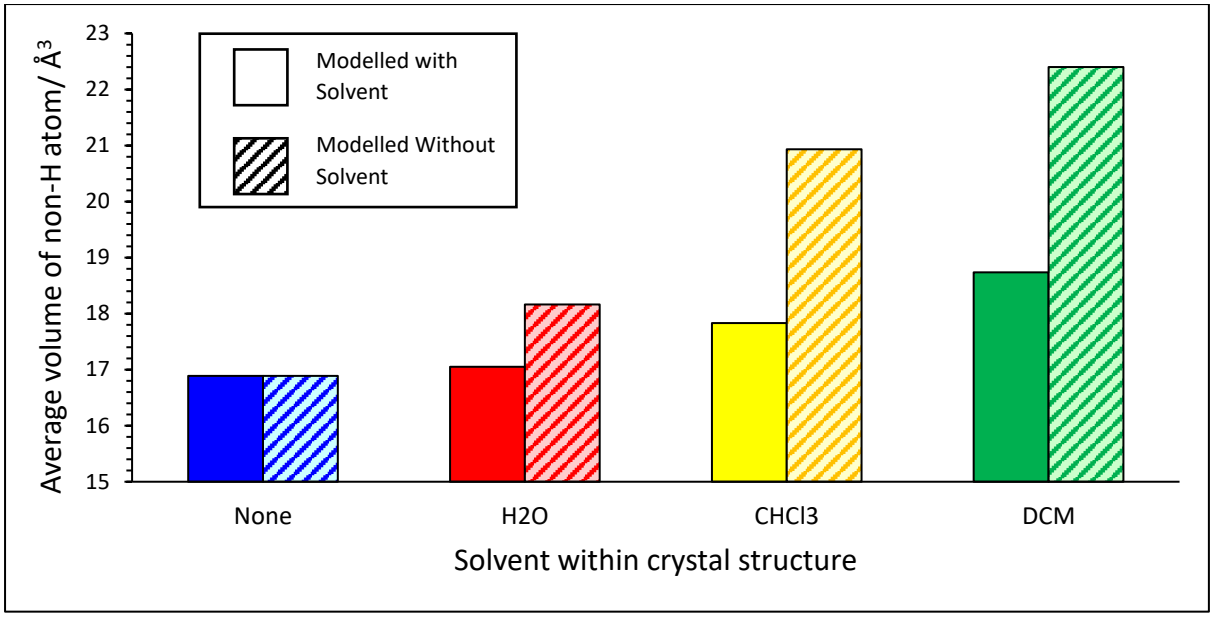

*Figure 70. A comparison of average atomic volume across the **D1** solvatomorphs modelled with and without a solvent present to give an idea of the amount of space within the crystal structure.*

This method provided only an estimate for the void space within the crystal structures. More sophisticated computational analysis was then employed to look at the amount of void space in the crystal structures. Using crystal explorer, crystal voids are calculated and visualised in Figure 71, with data presented in Table 20. This method uses the crystallographic data collected, but rather than modelling the procrystal electron density;[143] the opposite is employed, using the modelled nuclear positions to identify areas where the electron density is lowest.[123]

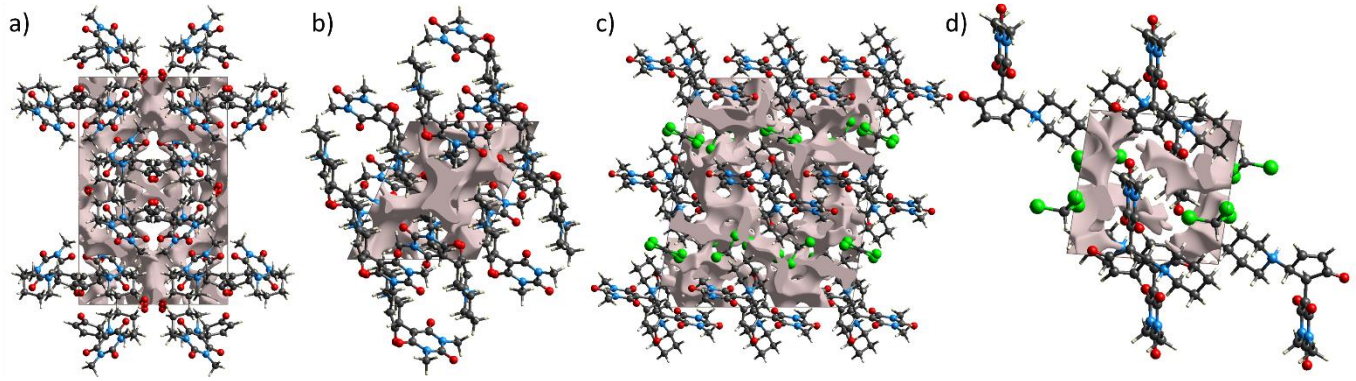

*Figure 71 – Crystal voids calculated for each solvatomorph unit cell at 120 K and visualised as grey surfaces for a) (**D1·1.5H$_2$O**), b) (**D1·unsolv**), c) (**D1·1.5DCM**), and d) (**D1·CHCl$_3$**). All are viewed along the b-axis apart from a), which is viewed along the c-axis.*

Table 20. Crystal voids data for each of the solvatomorphs per unit cell at 120 K calculated using crystal explorer with an isovalue of 0.002 e au^{-3}.

Solvatomorph	*Crystal Voids Volume/ Å³*	*Crystal Voids Surface Area/ Å²*	*Unit Cell Volume/ Å³*	*% Voids of Unit Cell Volume*	*Surface Area: Volume Ratio*
(D1·1.5H_2O)	290.20	1085.27	3319.17(8)	8.74 %	1: 2.79
(D1·unsolv)	200.13	581.79	1552.1(4)	12.89 %	1: 2.32
(D1·1.5DCM)	465.89	1405.28	4121.65(8)	11.30 %	1: 2.60
(D1·$CHCl_3$)	90.47	302.91	958.04(19)	9.44 %	1:2.86

This data shows that the crystal packing is most efficient in the hydrated structure, with crystal voids forming 8.74 % of the crystal volume. This is closely followed by (**D1·$CHCl_3$**) and then (**D1·1.5DCM**) with (**D1·unsolv**) having the least efficient packing with 12.89 % of the unit cell volume being void space. By looking at how these values change with temperature in Figure 72a/b, as temperature increases towards the switching temperature for each material, the void space increases whilst the surface area to volume ratio of the crystal decreases. This is expected as the crystal is being heated, but this method does not take into account the decreasing occupancy of the solvent sites in the structure with increasing temperature, and so the slope associated with each solvatomorph other than the unsolvated phase is likely much sharper in reality. A good way to gauge this would be to repeat and compare this experiment to a structure model where solvent molecules have been removed, but due to time constraints, this couldn't be completed.

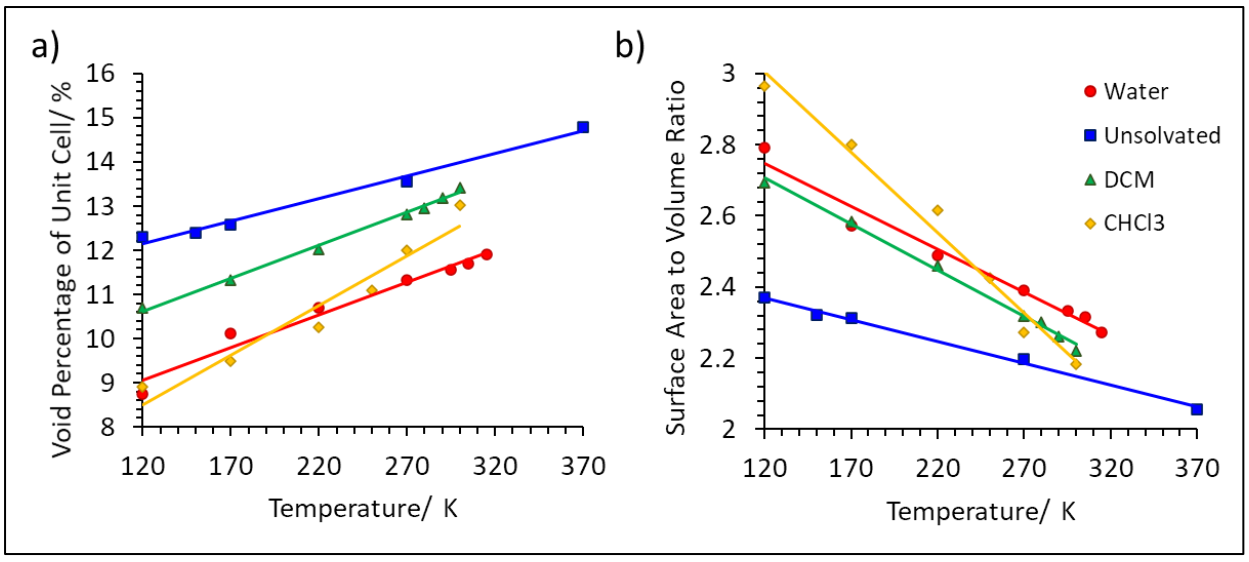

Figure 72. The effect of temperature on a) percentage crystal void volume for each solvatomorph and b) surface area to volume ratio of each solvatomorph.

4 Conclusions

The isolated solvatomorphs have given a good overview of the switching properties for this DASA. All solvated DASA crystals exhibit solid-state switching, with the switching temperature related to the material's crystal packing. Through solvent planes and channels, solvent molecules can escape the bulk of the crystal, either initiating or, as a result of, the solid-state switching of the material and disintegration of the crystal. In the absence of solvent, there is no temperature-induced switching implying the solid-state property, in these materials at least, is solvent-mediated.

In general, all **D1** molecules pack as dimers except in the hydrated crystal (**D1·1.5H_2O**), where stronger hydrogen bonds can be formed with the water molecules. This disruption of the dimerization gives the more stable crystals of the hydrated solvatomorph a higher switching temperature of 81 °C, which can be used for the production of proof-of-concept devices.

Table 21. Differences in switching temperatures between solvatomorphs and their contributing factors.

Property	(**D1·1.5H_2O**)	(**D1·unsolv**)	(**D1·1.5DCM**)	(**D1·$CHCl_3$**)
Switching Temperature/ °C	81	N/A	<25	<25
Number of crystallographic directions along which solvent channels/planes extend	1	0	3	2

From this study, we have determined, through commonalities between solvatomorphs, that the solid-state switching of DASA solvatomorphs is linked to the crystal structures' desolvation by way of solvent channels traversing the crystal. The desolvation either triggers the switching or the switching triggers desolvation. The switching temperature has been determined to be dictated by structural differences in the crystal packing of the solvatomorphs. The number of directions along which solvent channels extend likely influences the switching temperature of the solvatomorph. Increasing the number of directions along which solvent channels extend increases the probability that a solvent molecule will leave the structure (If there are more directions the solvent can leave, then the likelihood of the

solvent escaping the crystal increases). This, combined with the deviations in the intermolecular bond strengths between **D1** and the solvents, dictates the switching temperatures.

The material is multi-responsive, responding to light and temperature and humidity and mechanical force. The solid-state switching is also not isolated to the single-crystalline phase, with the material continuing to switch post disintegration or as thin films. DASAs share many properties with other molecular photoswitches and are still only in their infancy. This is the first study to look at the solid-state behaviour of DASAs extensively by in-depth structural analysis. In understanding these fundamental principles, it is expected that DASAs can be developed to rival and surpass other molecular photoswitches for real-world applications. This work lays the foundations for DASAs as switchable solid-state materials where they were previously limited to solution-state. The study's implications could see DASAs being used as sensors, dopants in smart composite materials, molecular logics in circuitry, as memory devices, in the production of mechanically active materials for use in soft robotics and molecular motors as photoactuators and others yet to be established.

4.1 Future Work

Due to university closure caused by the COVID-19 pandemic, only *ca.* 3 months of experimental work was possible, and so detailed structural analysis became more of a focus. During this time, working from home was achieved by using a shared desktop PC and desk space (limited access), to do data analysis and to run the project-specific programs (Crysalis Pro, Olex2, crystal explorer, image J). A personal laptop was used for more general use, plotting and reading literature. Without the ability to collect new data or perform further crystallisations on solvent mixtures, the computational methods of analysing crystallographic data were adopted. Upon re-opening of the university, the aim was to collect any missing data to complete a cohesive narrative for this thesis, so other research avenues had to be neglected.

Future work would include characterisation of the solvatomorphs from halogenated solvents (where possible), including reflectivity and physical characterisations, as well as the crystallographic analysis.

This could also include a more explicit determination of the switching temperature for the (**D1·1.5DCM**) and (**D1·$CHCl_3$**) solvatomorphs. Spectroscopic analysis of the material could also be developed as FTIR, Raman, and solid-state fluorometry were attempted on (**D1·1.5H_2O**) but gave inscrutable results. The spectra produced from the FTIR spectroscopy were inconclusive, showing wide, overlapping peaks, potentially due to residual solvent impurities in the samples. It was hoped these could be used to quantify the switching with humidity, but need much further development; results can be viewed in the appendix Figure G.

Raman spectroscopy was attempted to understand the solid-state switching of **D1,** but, surprisingly, it was found that the material fluoresces. This fluorescence was measured using solid-state fluorometry with an optimum excitation wavelength of 350 nm (UV) to produce strong emissions around 700 nm (red). This fluorescence could not be observed visually by irradiating with a UV lamp, and so it is assumed that the emission is either just beyond the visible spectrum or too weak to be observed. The spectra of this analysis can be viewed in the appendix Figure F. Unfortunately, due to constraints on laboratory access from the COVID-19 pandemic, this project route was deprioritised and could not be explored further, and so further work in this area is needed. This work includes the recollection of the fluorescence data to provide a spectrum that intensity has not gone beyond the measurable scale from overwhelming the detector.

The pursuit of mixed solvate phases is also a short-term direction of future investigation to provide the ability to control the switching temperature. A sample of (**D1·1DCM0.2H_2O**) was crystalised from wet DCM but unable to be investigated due to time constraints. In this case, water was a minor impurity with low occupancy, but the existence of water molecules and DCM within the crystal may result in a switching temperature between (**D1·1.5DCM**) and (**D1·1.5H_2O**), so above room temperature. The idea was to perform another solvent screening similar to Figure 16 but using mixtures of solvents and anti-solvents to crystalise samples via vapour diffusion methods. This may have caused some of the anti-solvent to crystalise in the structure, too, producing a different

solvatomorph or may have given access to new solvatomorphs that precipitated from other solvents too quickly in the initial screening. This was deprioritised, however, due to available lab time.

Future work is required to understand the mechanism by which these materials isomerise in the solid-state, whether it be induced or assisted by desolvation or whether the desolvation is a consequence of the switching. Development of the void space analysis of each of the solvatomorphs would help understand how these materials switch in the solid-state and the amount of space afforded to the DASA molecules upon desolvation. This could aid further studies into the role of crystallite size and its relationship to the switching temperature and the discrepancies between larger single-crystals and powders in the thermal studies.

Investigations into the DASA thin films on glass substrates are another avenue to explore, along with quantitative analysis of the hygrochromism and mechanochromic properties of **D1**. Understanding the amorphous form of the DASAs would aid with this and could include the use of solid-state NMR facilities to study the local structure of the DASA molecules in their linear form in the solid-state.

The thin films of the DASA material are an interesting area of development and come with an associated host of benefits when considering applications. These include the rapid synthesis associated with DASAs, and the ability to deposit these materials over a large area means that any devices are easily manufacturable. The key reagent in DASA manufacture – furfural – is also a by-product of the food industry so abundantly available at reasonable commercial prices. These have been shown to be multi-responsive with light, humidity and mechanical force heightening them above other smart molecular materials that usually rely on mixtures of smart materials – like the application for anti-counterfeiting or photopatterning.[8,103] Potential challenges to overcome could surround the leaching of the thin films as the DASA remains very water-soluble, but this could be overcome by coating them with protective transparent layers like plastics or glass, but what effect this would have on their multi responsiveness could only be found by experimentation. The DASAs multi responsive behaviour could be perceived as a limitation, too, as it means that they may only switch when exposed

to a very select set of conditions. This is why the ability to tune these conditions, potentially with mixed solvatomorphs, is exciting, as it could lead to the production of very selective sensors. The production of these films as proof-of-concept devices is foreseeably a more accessible steppingstone than integrating single-use multi-responsive single-crystals into such devices, and so this is the long-term direction that the research area will likely progress.

This is the first study of solid-state switching in DASAs with no observation of this previously recorded. The study focuses on a single first generation DASA molecule, but these switches are a vast family that can easily be modulated, and so it is likely that this behaviour will be observed for others. By having a thorough understanding of one case in which the DASA switches in the solid-state, the characterisation of any future observations in the field will be more accessible. It may be that other functionalised DASAs form crystals that do not disintegrate on transition, allowing for *in-situ* diffraction studies. These observations may not be limited to primary DASAs but second generation and third generation too, so having an understanding of one will aid the future progression of this field.

Acknowledgements

This Masters project was made possible by the support of Dr Helena Shepherd as principal investigator, offering academic guidance and advice. I am grateful for the help and support of Mr Sean Connolly, who was also invaluable, along with the rest of the Shepherd group. I would like to thank the Supramolecular Interfacial and Supramolecular Chemistry (SISC) group for the sense of community and the development opportunities. I would like to thank the School of Physical Sciences at the University of Kent for providing the facilities to carry out this project and providing access to the instrumentation used. I would also like to acknowledge the emotional support of Joshua Pearce, Dr. Helena Shepherd, and the Shepherd group, especially during the March – June closures due to the COVID-19 pandemic. Without this support, the project would not have been possible – thank you.

References

1 M. Irie, Y. Yasushi and S. Takahiro, *New Frontiers in Photochromism*, Springer Japan, 1st edn., 2013.

2 Y.-D. Cai, T.-Y. Chen, X. Q. Chen and X. Bao, Multiresponsive Donor–Acceptor Stenhouse Adduct: Opportunities Arise from a Diamine Donor, *Org. Lett.*, 2019, **21**, 7445–7449.

3 H. Zeng, O. M. Wani, P. Wasylczyk and A. Priimagi, Light-Driven, Caterpillar-Inspired Miniature Inching Robot, *Macromol. Rapid Commun.*, 2018, **39**, 1700224.

4 H. Huang, T. Orlova, B. Matt and N. Katsonis, Long-Lived Supramolecular Helices Promoted by Fluorinated Photoswitches, *Macromol. Rapid Commun.*, 2018, **39**, 1700387.

5 M. Manti, V. Cacucciolo and M. Cianchetti, Stiffening in soft robotics: A review of the state of the art, *IEEE Robot. Autom. Mag.*, 2016, **23**, 93–106.

6 L. Pfeifer, M. Scherübl, M. Fellert, W. Danowski, J. Cheng, J. Pol and B. L. Feringa, Photoefficient 2nd generation molecular motors responsive to visible light, *Chem. Sci.*, 2019, **10**, 8768–8773.

7 H. Zhao, X. Qin, L. Zhao, S. Dong, L. Gu, W. Sun, D. Wang and Y. Zheng, Invisible Inks for Secrecy and Anticounterfeiting: From Single to Double-encryption by Hydrochromic Molecules, *Cite This ACS Appl. Mater. Interfaces*, 2020, **12**, 8960.

8 A. Abdollahi, K. Sahandi-Zangabad and H. Roghani-Mamaqani, Rewritable Anticounterfeiting Polymer Inks Based on Functionalized Stimuli-Responsive Latex Particles Containing Spiropyran Photoswitches: Reversible Photopatterning and Security Marking, *ACS Appl. Mater. Interfaces*, 2018, **10**, 39279–39292.

9 S. Singh, K. Friedel, M. Himmerlich, Y. Lei, G. Schlingloff and A. Schober, Spatiotemporal Photopatterning on Polycarbonate Surface through Visible Light Responsive Polymer Bound DASA Compounds, *ACS Macro Lett.*, 2015, **4**, 1273–1277.

10 F. Y. Tang, J. N. Hou, K. X. Liang, Y. Liu, L. Deng and Y. N. Liu, A facile way to achieve all-photonic logic functions and photo-printing based on a donor-acceptor Stenhouse adduct, *New J. Chem.*, 2017, **41**, 6071–6075.

11 A. Natansohn, P. Rochon, M. Pézolet, P. Audet, D. Brown and S. To, Azo Polymers for Reversible Optical Storage. 4. Cooperative Motion of Rigid Groups in Semicrystalline Polymers, *Macromolecules*, 1994, **27**, 2580–2585.

12 S. Aiken, R. J. L. Edgar, C. D. Gabbutt, B. M. Heron and P. A. Hobson, *Dye. Pigment.*, 2018, 149, 92–121.

13 F. M. Raymo, Digital processing and communication with molecular switches, *Adv. Mater.*, 2002, **14**, 401–414.

14 U. Pischel, J. Andréasson, D. Gust and V. F. Pais, Information processing with molecules - Quo vadis?, *ChemPhysChem*, 2013, **14**, 28–46.

15 H. M. D. Bandara and S. C. Burdette, Photoisomerization in different classes of azobenzene, *Chem. Soc. Rev.*, 2012, **41**, 1809–1825.

16 M. Irie, T. Fukaminato, K. Matsuda and S. Kobatake, Photochromism of Diarylethene Molecules and Crystals: Memories, Switches, and Actuators, *Chem. Rev.*, 2014, **114**, 11863–12430.

17 Y. Yokoyama, Fulgides for Memories and Switches, *Chem. Rev.*, 2000, **100**, 1717–1739.

18 H. E. A. Kramer, in *Photochromism: Molecules and Systems*, Elsevier Inc., 2003, pp. 654–684.

19 R. Klajn, *Chem. Soc. Rev.*, 2014, 43, 148–184.

20 D. Bløger, S. Hecht, D. Bløger and S. Hecht, Visible-Light-Activated Molecular Switches, *Angew. Minireviews*, 2015, 11338–11349.

21 I. PerkinElmer informatics, .

22 S. Swansburg, E. Buncel and R. P. Lemieux, Thermal Racemization of Substituted Indolinobenzospiropyrans: Evidence of Competing Polar and Nonpolar Mechanisms, , DOI:10.1021/ja0001613.

23 I. J. Turchi and M. J. S. Dewar, *The Chemistry of Oxazoles*, .

24 C. K. Johnson, Ed., *Spectroscopy and Dynamics of Single Molecules*, Elsevier, 2019.

25 K. Stranius and K. Börjesson, Determining the photoisomerization quantum yield of photoswitchable molecules in solution and in the solid state, *Sci. Rep.*, 2017, **7**, 1–9.

26 M. Herder, B. M. Schmidt, L. Grubert, M. Pätzel, J. Schwarz and S. Hecht, Improving the fatigue resistance of diarylethene switches, *J. Am. Chem. Soc.*, 2015, **137**, 2738–2747.

27 V. Heines, Peter Griess—Discoverer of diazo compounds, *J. Chem. Educ.*, 1958, **35**, 187.

28 G. S. Hartley, *Nature*, 1937, 140, 281.

29 R. L. M. Allen and R. L. M. Allen, in *Colour Chemistry*, Springer US, 1971, pp. 21–36.

30 P. C. Ghosh and E. R. Watson, LXIX. - The effect of additional auxochromes on the colour of dyes. Part II. Triphenylmethane and azo-dyes, *J. Chem. Soc. Trans.*, 1917, **111**, 815–829.

31 H. Dürr and H. Bouas-Laurent, *Photochromism*, Elsevier, 2003.

32 C. R. Crecca and A. E. Roitberg, Theoretical Study of the Isomerization Mechanism of Azobenzene and Disubstituted Azobenzene Derivatives, *J. Phys. Chem. A*, 2006, **110**, 8188–8203.

33 A. Goulet-Hanssens and C. J. Barrett, Photo-control of biological systems with azobenzene polymers, *J. Polym. Sci. Part A Polym. Chem.*, 2013, **51**, 3058–3070.

34 R. Lyndon, K. Konstas, B. P. Ladewig, P. D. Southon, P. C. J. Kepert and M. R. Hill, Dynamic photo-switching in metal-organic frameworks as a route to low-energy carbon dioxide capture and release, *Angew. Chemie - Int. Ed.*, 2013, **52**, 3695–3698.

35 H. Li, M. R. Martinez, Z. Perry, H.-C. Zhou, P. Falcaro, C. Doblin, S. Lim, A. J. Hill, B. Halstead and M. R. Hill, A Robust Metal-Organic Framework for Dynamic Light-Induced Swing Adsorption of Carbon Dioxide, *Chem. - A Eur. J.*, 2016, **22**, 11176–11179.

36 I. Mita, K. Horie and K. Hirao, *Photochemistry in Polymer Solids. 9. Photoisomerization of Azobenzene in a Polycarbonate Film*, 1989, vol. 22.

37 O. M. Wani, H. Zeng and A. Priimagi, A light-driven artificial flytrap, *Nat. Commun.*, 2017, **8**, 1–7.

38 S. Shinkai, T. Nakaji, T. Ogawa, K. Shigematsu and O. Manabe, Photoresponsive Crown Ethers. 2. Photocontrol of Ion Extraction and Ion Transport by a Bis(crown ether) with a Butterfly-like Motion, *J. Am. Chem. Soc.*, 1981, **103**, 111–115.

39 H. Shahsavan, A. Aghakhani, H. Zeng, Y. Guo, Z. S. Davidson, A. Priimagi and M. Sitti, Bioinspired underwater locomotion of light-driven liquid crystal gels, *Proc. Natl. Acad. Sci. U. S. A.*, 2020, **117**, 5125–5133.

40 H. Zeng, O. M. Wani, P. Wasylczyk, R. Kaczmarek and A. Priimagi, Self-Regulating Iris Based on Light-Actuated Liquid Crystal Elastomer, *Adv. Mater.*, , DOI:10.1002/adma.201701814.

41 M. Irie and M. Mohri, Thermally Irreversible Photochromic Systems. Reversible Photocyclization of Diarylethene Derivatives, *J. Org. Chem.*, 1988, **53**, 803–808.

42 J. P. Dela Cruz Calupitan, O. Galangau, O. Guillermet, R. Coratger, T. Nakashima, G. Rapenne and T. Kawai, Synthesis and Photochromism of Chloro- and tert-Butyl-Functionalized Terarylene Derivatives for Surface Deposition, *European J. Org. Chem.*, 2017, **2017**, 2451–2461.

43 H. Jean-Ruel, M. Gao, M. A. Kochman, C. Lu, L. C. Liu, R. R. Cooney, C. A. Morrison and R. J. Dwayne Miller, Ring-closing reaction in diarylethene captured by femtosecond electron crystallography, *J. Phys. Chem. B*, 2013, **117**, 15894–15902.

44 W. T. A. M. van der Lugt and L. J. Oosterhoff, Symmetry Control and Photoinduced Reactions, *J. Am. Chem. Soc.*, 1969, **91**, 6042–6049.

45 K. Uchida, M. Saito, A. Murakami, S. Nakamura and M. Irie, Non-Destructive Readout of the Photochromic Reactions of Diarylethene Derivatives Using Infrared Light, *Adv. Mater.*, 2003, **15**, 121–125.

46 K. Uchida, A. Takata, M. Saito, A. Murakami, S. Nakamura and M. Irie, Synthesis of Novel Photochromic Films by Oxidation Polymerization of Diarylethenes Containing Phenol Groups, *Adv. Funct. Mater.*, 2003, **13**, 755–762.

47 A. Takata, M. Saito, S. Yokojima, A. Murakami, S. Nakamura, M. Irie and K. Uchida, Micrometer-scale

photochromic recording on amorphous diarylethene film and nondestructive readout using near-field IR light, *Japanese J. Appl. Physics, Part 1 Regul. Pap. Short Notes Rev. Pap.*, 2006, **45**, 7114–7120.

48 S. Kawata, Photorefractive optics in three-dimensional digital memory, *Proc. IEEE*, 1999, **87**, 2009–2020.

49 M. Irie, T. Fukaminato, T. Sasaki, N. Tamai and T. Kawai, A digital fluorescent molecular photoswitch, *Nature*, 2002, **420**, 759–760.

50 F. Terao, M. Morimoto and M. Irie, Light-driven molecular-crystal actuators: Rapid and reversible bending of rodlike mixed crystals of diarylethene derivatives, *Angew. Chemie - Int. Ed.*, 2012, **51**, 901–904.

51 D. Kitagawa, H. Nishi and S. Kobatake, Photoinduced twisting of a photochromic diarylethene crystal, *Angew. Chemie - Int. Ed.*, 2013, **52**, 9320–9322.

52 J. Clayden, N. Greeves and S. Warren, *Organic Chemistry*, Oxford University Press, Oxford, Second., 2012.

53 H. Görner, in *Physical Chemistry Chemical Physics*, The Royal Society of Chemistry, 2001, vol. 3, pp. 416–423.

54 G. Favaro, F. Masetti, U. Mazzucato, G. Ottavi, P. Allegrini and V. Malatesta, Photochromism, thermochromism and solvatochromism of some spiro[indolinoxazine]-photomerocyanine systems: Effects of structure and solvent, *J. Chem. Soc. Faraday Trans.*, 1994, **90**, 333–338.

55 D. S. Tipikin, Mechanochromism of organic compounds as exemplified by spiropyran, *Russ. J. Phys. Chem. A*, 2001, **75**, 1876–1879.

56 X. Meng, G. Qi, C. Zhang, K. Wang, B. Zou and Y. Ma, Visible mechanochromic responses of spiropyrans in crystals via pressure-induced isomerization, *Chem. Commun.*, 2015, **51**, 9320–9323.

57 D. A. Davis, A. Hamilton, J. Yang, L. D. Cremar, D. Van Gough, S. L. Potisek, M. T. Ong, P. V Braun, T. J. Martínez, S. R. White, J. S. Moore and N. R. Sottos, Force-induced activation of covalent bonds in mechanoresponsive polymeric materials, *Nature*, 2009, **459**, 68–72.

58 W. Qiu, P. A. Gurr, G. Da Silva and G. G. Qiao, Insights into the mechanochromism of spiropyran elastomers, *Polym. Chem.*, 2019, **10**, 1650–1659.

59 Q. Shen, Y. Cao, S. Liu, M. L. Steigerwald and X. Guo, Conformation-Induced Electrostatic Gating of the Conduction of Spiropyran-Coated Organic Thin-Film Transistors, , DOI:10.1021/jp9026817.

60 A. Julià-López, J. Hernando, D. Ruiz-Molina, P. González-Monje, J. Sedó and C. Roscini, Temperature-Controlled Switchable Photochromism in Solid Materials, *Angew. Chemie*, 2016, **128**, 15268–15272.

61 A. Julià -López López, D. Ruiz-Molina, J. Hernando and C. Roscini, Solid Materials with Tunable Reverse Photochromism, , DOI:10.1021/acsami.8b22335.

62 T. Kawai, T. Koshido, Y. Kaneuchi and K. Yoshino, Photomemory effects in electrical and optical properties of photochromic dye in the non-crystalline solid state, *Thin Solid Films*, 1996, **273**, 195–198.

63 S. Kobatake, S. Takami, H. Muto, T. Ishikawa and M. Irie, Rapid and reversible shape changes of molecular crystals on photoirradiation, *Nature*, 2007, **446**, 778–781.

64 K.-J. Chen, Y.-C. Tsai, Y. Suzaki, K. Osakada, A. Miura and M. Horie, Rapid and reversible photoinduced switching of a rotaxane crystal, *Nat. Publ. Gr.*, , DOI:10.1038/ncomms13321.

65 M. Morimoto and M. Irie, A diarylethene cocrystal that converts light into mechanical work, *J. Am. Chem. Soc.*, 2010, **132**, 14172–14178.

66 Y. Gui, X. Yao, I. A. Guzei, M. M. Aristov, J. Yu and L. Yu, A Mechanism for Reversible Solid-State Transitions Involving Nitro Torsion, *Chem. Mater.*, 2020, **32**, 7765.

67 R. Medishetty, A. Husain, Z. Bai, T. Runčevski, R. E. Dinnebier, P. Naumov and J. J. Vittal, Single crystals popping under UV light: A photosalient effect triggered by a [2+2] cycloaddition reaction, *Angew. Chemie - Int. Ed.*, 2014, **53**, 5907–5911.

68 R. Medishetty, S. C. Sahoo, C. E. Mulijanto, P. Naumov and J. J. Vittal, Photosalient behavior of photoreactive crystals, *Chem. Mater.*, 2015, **27**, 1821–1829.

69 P. Commins, I. T. Desta, D. P. Karothu, M. K. Panda and P. Naumov, Crystals on the move: Mechanical effects in dynamic solids, *Chem. Commun.*, 2016, **52**, 13941–13954.

70 Y. Nakagawa, M. Morimoto, N. Yasuda, K. Hyodo, S. Yokojima, S. Nakamura and K. Uchida, Photosalient Effect of Diarylethene Crystals of Thiazoyl and Thienyl Derivatives, *Chem. – A Eur. J.*, 2019, **25**, 7874–7880.

71 K. Uchida, R. Nishimura, E. Hatano, H. Mayama and S. Yokojima, Photochromic Crystalline Systems Mimicking Bio-Functions, *Chem. - A Eur. J.*, 2018, **24**, 8491–8506.

72 D. J. Shields, D. P. Karothu, K. Sambath, R. A. A. U. Ranaweera, S. Schramm, A. Duncan, B. Duncan, J. A. Krause, A. D. Gudmundsdottir, P. Naumov and P. Naumov, Cracking Under Internal Pressure: Photodynamic Behavior of Vinyl Azide Crystals Through N2 Release Cracking Under Internal Pressure: Photodynamic Behavior of Vinyl Azide Crystals Through N 2 Release, , DOI:10.1021/jacs.0c07830.

73 A. Lévesque, T. Maris and J. D. Wuest, ROY Reclaims Its Crown: New Ways to Increase Polymorphic Diversity, *J. Am. Chem. Soc.*, 2020, **142**, 11873–11883.

74 M. K. Mishra and C. C. Sun, Conformation Directed Interaction Anisotropy Leading to Distinct Bending Behaviors of Two ROY Polymorphs, *Cryst. Growth Des.*, 2020, **20**, 4764–4769.

75 L. Yu, G. A. Stephenson, C. A. Mitchell, C. A. Bunnell, S. V. Snorek, J. J. Bowyer, T. B. Borchardt, J. G. Stowell and S. R. Byrn, Thermochemistry and conformational polymorphism of a hexamorphic crystal system, *J. Am. Chem. Soc.*, 2000, **122**, 585–591.

76 S. Chen, I. A. Guzei and L. Yu, New polymorphs of ROY and new record for coexisting polymorphs of solved structures, *J. Am. Chem. Soc.*, 2005, **127**, 9881–9885.

77 B. A. Nogueira, C. Castiglioni and R. Fausto, *Commun. Chem.*, 2020, 3, 1–12.

78 L. Yu, Polymorphism in molecular solids: An extraordinary system of red, orange, and yellow crystals, *Acc. Chem. Res.*, 2010, **43**, 1257–1266.

79 H. G. Brittain, *J. Pharm. Sci.*, 2012, 101, 464–484.

80 T. Steiner, The Hydrogen Bond in the Solid State, *Angew. Chemie Int. Ed.*, 2002, **41**, 48–76.

81 T. W. G. Solomons and C. B. Fryhle, *Organic Chemistry*, John Wiley & Sons, Inc, Wiley inte., 2004.

82 Elangannan Arunan, Gautam R. Desiraju, Roger A. Klein, Joanna Sadlej, Steve Scheiner, Ibon Alkorta, David C. Clary, Robert H. Crabtree, Joseph J. Dannenberg, Pavel Hobza, Henrik G. Kjaergaard, Anthony C. Legon, Benedetta Mennucci and David J. Nesbitt, Definition of the hydrogen bond.

83 A. A. Kananenka and J. L. Skinner, Unusually strong hydrogen bond cooperativity in particular (H2O)20 clusters, *Phys. Chem. Chem. Phys.*, 2020, **22**, 18124–18131.

84 J. L. Kuo, C. V. Ciobanu, L. Ojamäe, I. Shavitt and S. J. Singer, Short H-bonds and spontaneous self-dissociation in (H2O)20: Effects of H-bond topology, *J. Chem. Phys.*, 2003, **118**, 3583–3588.

85 U. Bergmann, A. Di Cicco, P. Wernet, E. Principi, P. Glatzel and A. Nilsson, Nearest-neighbor oxygen distances in liquid water and ice observed by x-ray Raman based extended x-ray absorption fine structure, *J. Chem. Phys.*, 2007, **127**, 174504.

86 G. R. Wileylb and S. I. Miller, *Thermodynamic Parameters for Hydrogen Bonding of Chloroform with Lewis Bases in Cyclohexane. A Proton Magnetic Resonance Study*, 1971, vol. 4.

87 S. Glasstone, The structure of some molecular complexes in the liquid phase, *Trans. Faraday Soc.*, 1937, **33**, 200–206.

88 C. H. Schwalbe, *Crystallogr. Rev.*, 2012, 18, 191–206.

89 M. C. Wahl, M. Sundaralingam and M. Sundarallngam, C-H···O hydrogen bonding in biology, *Prec. Natl. Acad. Sci. U. S. A*, 1990, **4**, 6317–6327.

90 G. A. Jeffrey, Hydrogen-bonding: An update, *Crystallogr. Rev.*, 1995, **4**, 213–254.

91 J. Stenhouse, Ueber die Oele, die bei der Einwirkung der Schwefelsäure auf verschiedene Vegetabilien entstehen, *Ann. der Chemie und Pharm.*, 1850, **74**, 278–297.

92 S. Helmy, F. A. Leibfarth, S. Oh, J. E. Poelma, C. J. Hawker and J. R. De Alaniz, Photoswitching Using Visible Light: A New Class of Organic Photochromic Molecules, *J. Am. Chem. Soc.*, 2014, **136**, 8169–8172.

93 S. Helmy, S. Oh, F. A. Leibfarth, C. J. Hawker and J. R. De Alaniz, Design and Synthesis of Donor − Acceptor

Stenhouse Adducts: A Visible Light Photoswitch Derived from Furfural, *J. Org. Chem.*, 2014, **79**, 11316–11329.

94 N. Mallo, P. T. Brown, H. Iranmanesh, T. S. C. Macdonald, M. J. Teusner, J. B. Harper, G. E. Ball and J. E. Beves, Photochromic switching behaviour of donor – acceptor Stenhouse adducts in organic solvents †, *Chem. Commun.*, 2016, **52**, 13576–13579.

95 N. Mallo, E. D. Foley, H. Iranmanesh, A. D. W. Kennedy, E. T. Luis, J. Ho, J. B. Harper and J. E. Beves, Structure-function relationships of donor-acceptor Stenhouse adduct photochromic switches, *Chem. Sci.*, 2018, **9**, 8242–8252.

96 C. Piutti and F. Quartieri, The Piancatelli Rearrangement: New Applications for an Intriguing Reaction, *Molecules*, 2013, **18**, 12290–12312.

97 J. R. Hemmer, S. O. Poelma, N. Treat, Z. A. Page, N. D. Dolinski, Y. J. Diaz, W. Tomlinson, K. D. Clark, J. P. Hooper, C. Hawker and J. Read De Alaniz, Tunable Visible and Near Infrared Photoswitches, *J. Am. Chem. Soc.*, 2016, **138**, 13960–13966.

98 J. R. Hemmer, Z. A. Page, K. D. Clark, F. Stricker, N. D. Dolinski, C. J. Hawker and J. Read De Alaniz, Controlling Dark Equilibria and Enhancing Donor-Acceptor Stenhouse Adduct Photoswitching Properties through Carbon Acid Design, *J. Am. Chem. Soc.*, 2018, **140**, 10425–10429.

99 M. M. Lerch, M. Medved, A. Lapini, A. D. Laurent, A. Iagatti, L. Bussotti, W. Szymański, W. J. Buma, P. Foggi, M. Di Donato and B. L. Feringa, Tailoring Photoisomerization Pathways in Donor-Acceptor Stenhouse Adducts: The Role of the Hydroxy Group, *J. Phys. Chem. A*, 2018, **122**, 955–964.

100 M. M. Lerch, S. J. Wezenberg, W. Szymanski and B. L. Feringa, Unraveling the Photoswitching Mechanism in Donor−Acceptor Stenhouse Adducts, *J. Am. Chem. Soc*, 2016, **138**, 6344–6347.

101 M. Di Donato, M. M. Lerch, A. Lapini, A. D. Laurent, A. Iagatti, L. Bussotti, S. P. Ihrig, M. Medved, D. Jacquemin, W. Szymański, W. J. Buma, P. Foggi and B. L. Feringa, Shedding Light on the Photoisomerization Pathway of Donor-Acceptor Stenhouse Adducts, *J. Am. Chem. Soc.*, 2017, **139**, 15596–15599.

102 B. P. Mason, M. Whittaker, J. Hemmer, S. Arora, A. Harper, S. Alnemrat, A. McEachen, S. Helmy, J. Read De Alaniz and J. P. Hooper, A temperature-mapping molecular sensor for polyurethane-based elastomers, *Appl. Phys. Lett.*, 2016, **108**, 041906.

103 S. Ulrich, J. R. Hemmer, Z. A. Page, N. D. Dolinski, O. Rifaie-Graham, N. Bruns, C. J. Hawker, L. F. Boesel and J. Read De Alaniz, Visible Light-Responsive DASA-Polymer Conjugates, *ACS Macro Lett.*, 2017, **6**, 738–742.

104 Q. Chen, Y. J. Diaz, M. C. Hawker, M. R. Martinez, Z. A. Page, S. Xiao-An Zhang, C. J. Hawker and J. Read De Alaniz, Stable Activated Furan and Donor-Acceptor Stenhouse Adduct Polymer Conjugates as Chemical and Thermal Sensors, *Macromolecules*, 2019, **52**, 4370–4375.

105 Y. J. Diaz, Z. A. Page, A. S. Knight, N. J. Treat, J. R. Hemmer, C. J. Hawker and J. Read de Alaniz, A Versatile and Highly Selective Colorimetric Sensor for the Detection of Amines, *Chem. - A Eur. J.*, 2017, **23**, 3562–3566.

106 B. Liu, P. A. Gurr and G. G. Qiao, Irreversible Spoilage Sensors for Protein-Based Food, *ACS Sensors*, , DOI:10.1021/acssensors.0c01211.

107 D. Wang, L. Zhao, H. Zhao, J. Wu, M. Wagner, W. Sun, X. Liu, M.-S. Miao and Y. Zheng, Inducing molecular isomerization assisted by water, , DOI:10.1038/s42004-019-0221-5.

108 A. Balamurugan and H. Il Lee, A Visible Light Responsive On-Off Polymeric Photoswitch for the Colorimetric Detection of Nerve Agent Mimics in Solution and in the Vapor Phase, *Macromolecules*, 2016, **49**, 2568–2574.

109 D. Zhong, Z. Cao, B. Wu, Q. Zhang and G. Wang, Polymer dots of DASA-functionalized polyethyleneimine: Synthesis, visible light/pH responsiveness, and their applications as chemosensors, *Sensors Actuators, B Chem.*, 2018, **254**, 385–392.

110 S. Jia, A. Tan, A. Hawley, B. Graham and B. J. Boyd, Visible light-triggered cargo release from donor acceptor Stenhouse adduct (DASA)-doped lyotropic liquid crystalline nanoparticles, *J. Colloid Interface Sci.*, 2019, **548**, 151–159.

111 O. Rifaie-Graham, S. Ulrich, N. F. B. Galensowske, S. Balog, M. Chami, D. Rentsch, J. R. Hemmer, J. Read De Alaniz, L. F. Boesel and N. Bruns, Wavelength-Selective Light-Responsive DASA-Functionalized Polymersome Nanoreactors, *J. Am. Chem. Soc.*, 2018, **140**, 8027–8036.

112 B. F. Lui, N. T. Tierce, F. Tong, M. M. Sroda, H. Lu, J. Read De Alaniz and C. J. Bardeen, Unusual concentration

dependence of the photoisomerization reaction in donor-acceptor Stenhouse adducts, *Photochem. Photobiol. Sci.*, 2019, **18**, 1587–1595.

113 S. W. Connolly and H. J. Shepherd, University of Kent, 2019.

114 J. W. Mullin, *Crystallization* , Butterworth-Heinemann, London, 4 th., 2001.

115 J. Schindelin, I. Arganda-Carreras, E. Frise, V. Kaynig, M. Longair, T. Pietzsch, S. Preibisch, C. Rueden, S. Saalfeld, B. Schmid, J. Y. Tinevez, D. J. White, V. Hartenstein, K. Eliceiri, P. Tomancak and A. Cardona, *Nat. Methods*, 2012, 9, 676–682.

116 Rigaku Oxford Diffraction, 2016, 171.38.43.

117 O. V. Dolomanov, L. J. Bourhis, R. J. Gildea, J. A. K. Howard and H. Puschmann, OLEX2: a complete structure solution, refinement and analysis program, *J. Appl. Crystallogr.*, 2009, **42**, 339–341.

118 G. Sheldrick, Crystal structure refinement with SHELXL, *Acta Crystallogr. Sect. C*, 2015, **71**, 3–8.

119 M. J. Turner, J. J. McKinnon, S. K. GWolff, D. J. Rimwood, P. R. Spackman, D. Jayatilaka and M. A. Spackman, CrystalExplorer17.

120 D. Jayatilaka and D. J. Grimwood, in *Lecture Notes in Computer Science (including subseries Lecture Notes in Artificial Intelligence and Lecture Notes in Bioinformatics)*, Springer Verlag, 2003, vol. 2660, pp. 142–151.

121 M. A. Spackman and P. G. Byrom, A novel definition of a molecule in a crystal, *Chem. Phys. Lett.*, 1997, **267**, 215–220.

122 F. L. Hirshfeld, Bonded-atom fragments for describing molecular charge densities, *Theor. Chim. Acta*, 1977, **44**, 129–138.

123 M. J. Turner, J. J. McKinnon, D. Jayatilaka and M. A. Spackman, Visualisation and characterisation of voids in crystalline materials, *CrystEngComm*, 2011, **13**, 1804–1813.

124 J. J. Mckinnon, A. S. Mitchell and M. A. Spackman, *Visualising intermolecular interactions in crystals: naphthalene vs. terephthalic acid*, 1998.

125 J. J. McKinnon, D. Jayatilaka and M. A. Spackman, Towards quantitative analysis of intermolecular interactions with Hirshfeld surfaces, *Chem. Commun.*, 2007, 3814–3816.

126 M. A. Spackman and J. J. McKinnon, Fingerprinting intermolecular interactions in molecular crystals, *CrystEngComm*, 2002, **4**, 378–392.

127 M. A. Spackman and D. Jayatilaka, Hirshfeld surface analysis, *CrystEngComm*, 2009, **11**, 19–32.

128 I. Advanced Chemistry Development, 2010.

129 G. R. Fulmer, A. J. M Miller, N. H. Sherden, H. E. Gottlieb, A. Nudelman, B. M. Stoltz, J. E. Bercaw, K. I. Goldberg and M. Beckman, NMR Chemical Shifts of Trace Impurities: Common Laboratory Solvents, Organics, and Gases in Deuterated Solvents Relevant to the Organometallic Chemist, *Organometallics*, 2010, **29**, 2176–2179.

130 N. Mallo, A. Tron, J. Andréasson, J. B. Harper, L. S. D. Jacob, N. D. McClenaghan, G. Jonusauskas and J. E. Beves, Hydrogen-Bonding Donor-Acceptor Stenhouse Adducts, *ChemPhotoChem*, 2020, **4**, 407–412.

131 P. D. Bailey and K. M. Morgan, in *Organonitrogen Chemistry*, eds. S. G. Davies, R. G. Compton, J. Evans and L. F. Gladden, Oxford University Press, 1996, pp. 4–25.

132 G. A. Jeffrey, *An Introduction to Hydrogen Bonding*, Oxford University Press, Oxford, 1997.

133 A. H. White and W. S. Bishop, Dielectric Evidence of Molecular Rotation in the Crystals of Certain Non-aromatic Compounds, *J. Am. Chem. Soc.*, 1940, **62**, 8–16.

134 E. Li, K. Jie, M. Liu, X. Sheng, W. Zhu and F. Huang, *Chem. Soc. Rev.*, 2020, 49, 1517–1544.

135 L. Greenspan, Humidity Fixed Points of Binary Saturated Aqueous Solutions, *J. Res. Natl. Bur. Stand. Phys. Chem.*, 1976, **81**, 89–96.

136 J. Qi, Y. Gao, H. Jia, M. Richter, L. Huang, Y. Cao, H. Yang, Q. Zheng, R. Berger, J. Liu, X. Lin, H. Lu, Z. Cheng, M. Ouyang, X. Feng, S. Du and H.-J. Gao, Force-Activated Isomerization of a Single Molecule, *Cite This J. Am. Chem. Soc*, , DOI:10.1021/jacs.0c00192.

137 W. Huang, Z. Zhu, J. Wen, X. Wang, M. Qin, Y. Cao, H. Ma and W. Wang, Single Molecule Study of Force-Induced Rotation of Carbon-Carbon Double Bonds in Polymers, *ACS Nano*, 2017, **11**, 194–203.

138 J. N. Ladenthin, T. Frederiksen, M. Persson, J. C. Sharp, S. Gawinkowski, J. Waluk and T. Kumagai, Force-induced tautomerization in a single molecule, *Nat. Chem.*, 2016, **8**, 935–940.

139 C. R. Taylor and G. M. Day, Evaluating the Energetic Driving Force for Cocrystal Formation, *Cryst. Growth Des.*, 2018, **18**, 892–904.

140 A. G. Athanassiadis, M. Z. Miskin, P. Kaplan, N. Rodenberg, S. H. Lee, J. Merritt, E. Brown, J. Amend, H. Lipson and H. M. Jaeger, Particle shape effects on the stress response of granular packings, *Soft Matter*, 2014, **10**, 48–59.

141 J. Baker and A. Kudrolli, Maximum and minimum stable random packings of Platonic solids, *Phys. Rev. E - Stat. Nonlinear, Soft Matter Phys.*, 2010, **82**, 061304.

142 H. Maruyama, T. Kawai, M.-S. Kim and M. Irie, Novel Nondestructive Readout Methods For Near-field Optical Recording with Large Refractive Index Modulation in Amorphous Diarylethene Layer, *Japanese J. Appl. Phys. To*, 2004, **43**, 1625.

143 R. T. Downs, G. V. Gibbs, M. B. Boisen and K. M. Rosso, A comparison of procrystal and ab initio model representations of the electron-density distributions of minerals, *Phys. Chem. Miner.*, 2002, **29**, 369–385.

Thesis Appendix

Thomas Hitchings

Contents

Appendix A – Reflectivity Measurement and Data Processing

Reflectivity Backgrounds

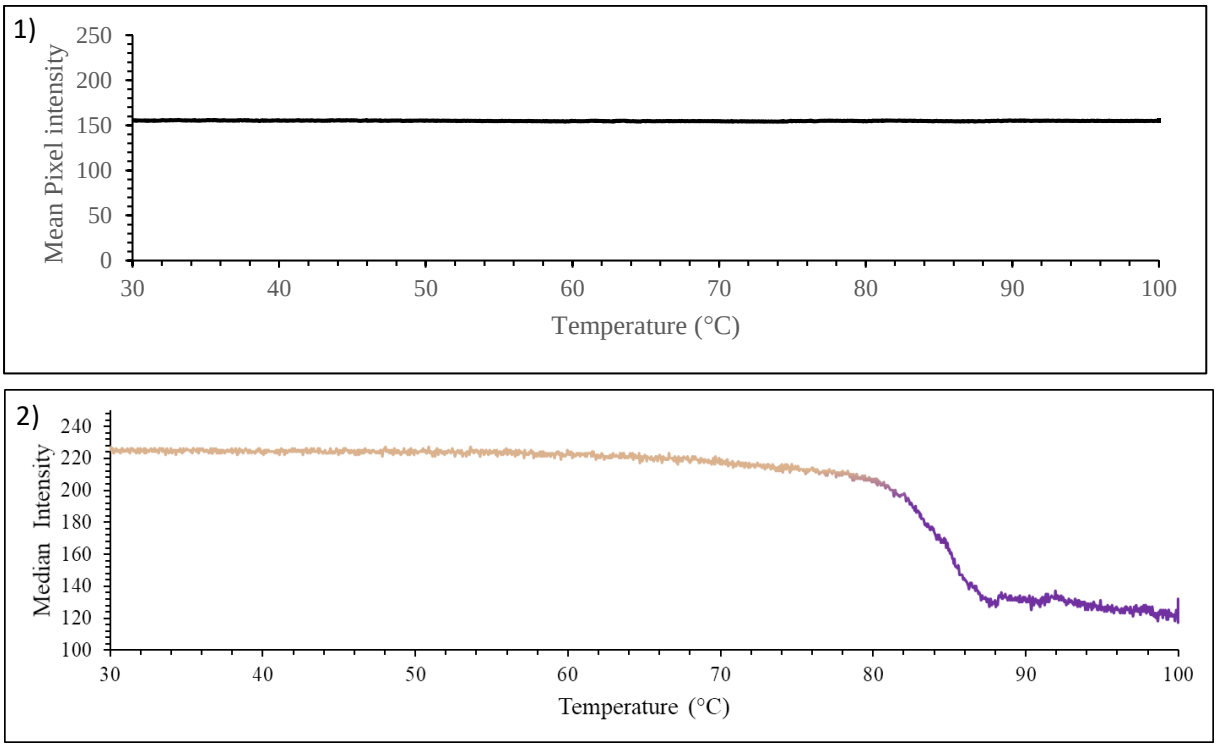

Figure A. 1) Changes in background pixel intensity for reflectivity measurements on the same scale as 2) a reflectivity measurement from the main text.

As can be seen in Figure A1, there are negligible changes in the background of this measurement, so no corrections were needed as the effects were minimal. Equation A was used as the general method for normalising data as a percentage and also describes how a background would have been deducted if needed.

$$z = \frac{x_i - Max(y)}{Max(y) - (Min(y)} \times 100$$

Equation A. min-max normalisation

$$y = x - bgrd$$

z = normalised measurement value as a percentage

X_i = individual value from the data population

X = measurement data population (1xn column)

Bgrd = Background data population (1xn column)

y = background corrected measurement data (1xn column)

Appendix B- Synthetic Procedure

Synthetic intermediate (**INT1**)

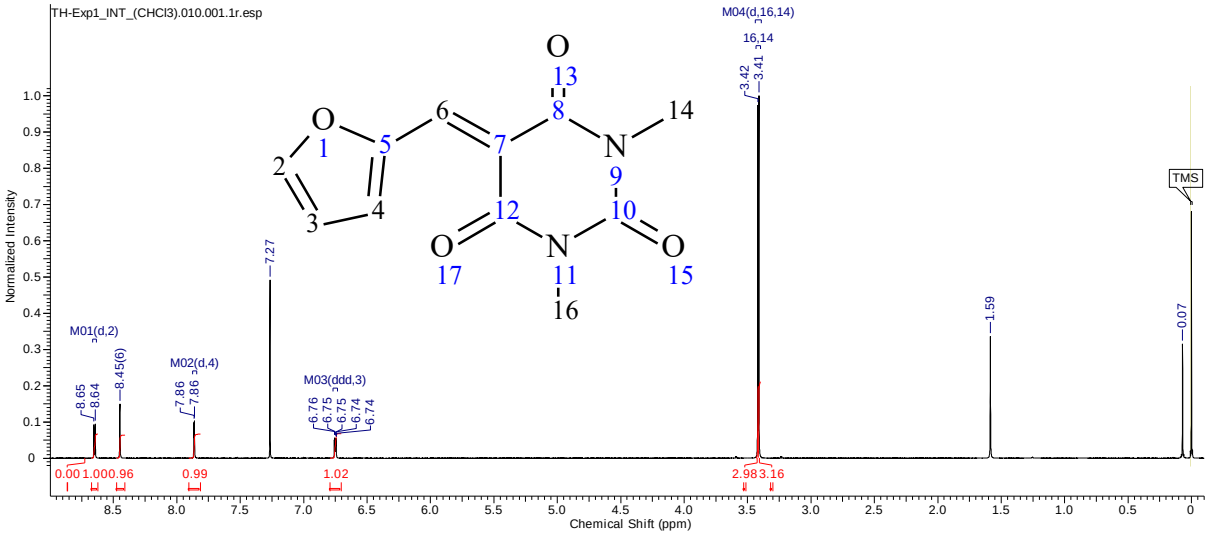

*Figure B. ^{1}H-NMR of **INT1** in deuterated Chloroform*

PXRD

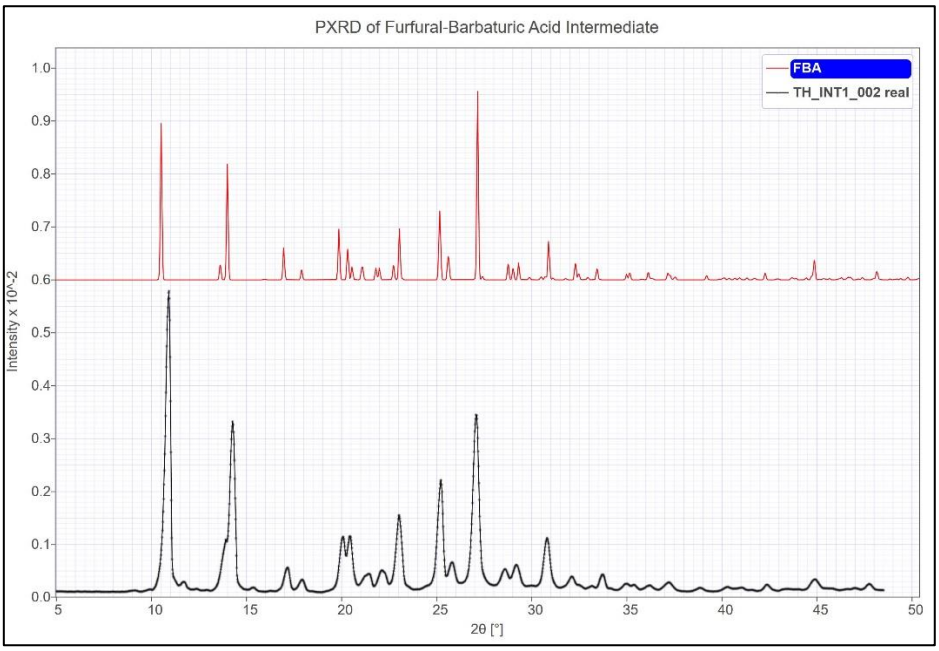

Figure C - PXRD pattern of TH_INT1_002 vs the virtual pattern generated by SCXRD from REF 1

The PXRD pattern show unambiguously the phase purity of the intermediate for this reaction. The high crystallinity will also make it a significant impurity in subsequent samples produced from it and therefore easily identifiable.

DASA 1(**D1**)

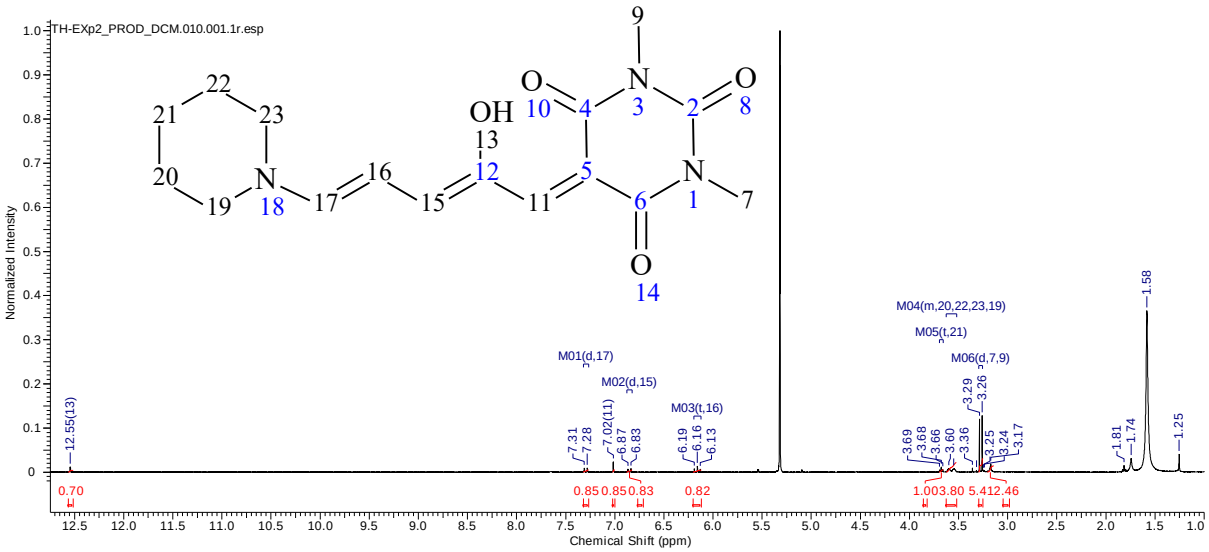

*Figure D. ^{1}H-NMR of **D1** in deuterated dichloromethane*

There were a couple of commonly identified solvent residues in the sample alongside the reference and sample peaks.[2]

Appendix C – Miscellaneous Spectroscopy

Fluorometry

Solid-state fluorometry was performed using the Agilent Cary Eclipse fluorescence spectrophotometer with the Agilent Cary Eclipse solid sample holder accessory. An excitation wavelength of 350 nm was used with emission data collected over the range of 300 nm - 800 nm. Spectra are then exported as .txt files and processed in Microsoft Excel. Results are in Figure E.

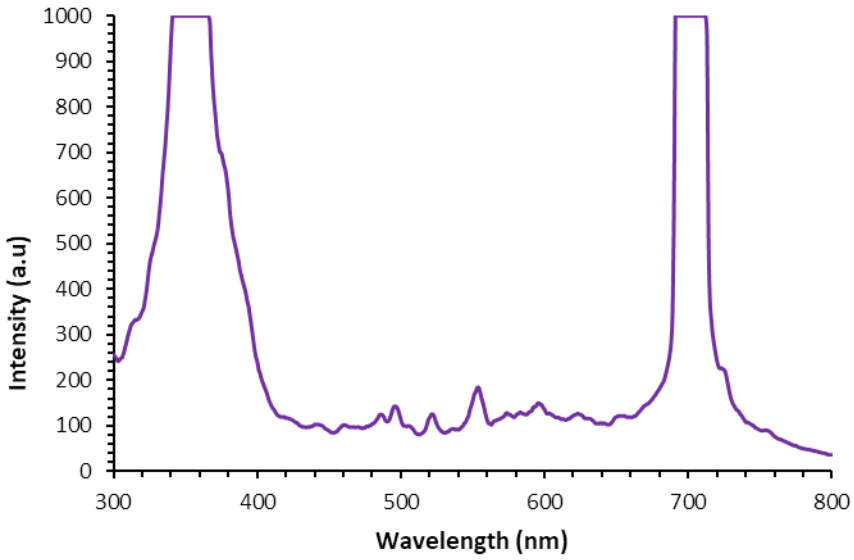

*Figure E. Solid-state fluorescence emission spectrum produced from excitation at 350 nm for freshly synthesised **D1***

Raman spectroscopy was attempted to understand the solid-state switching of **D1** but surprisingly it was found that the material fluoresces. This fluorescence was measured using solid-state fluorometry with an optimum excitation wavelength of 350 nm (UV) to produce strong emissions around 700 nm (red). This fluorescence could not be observed visually by irradiating with a UV lamp and so it is assumed that the emission is either just beyond the visible spectrum or too weak to be observed.

FTIR

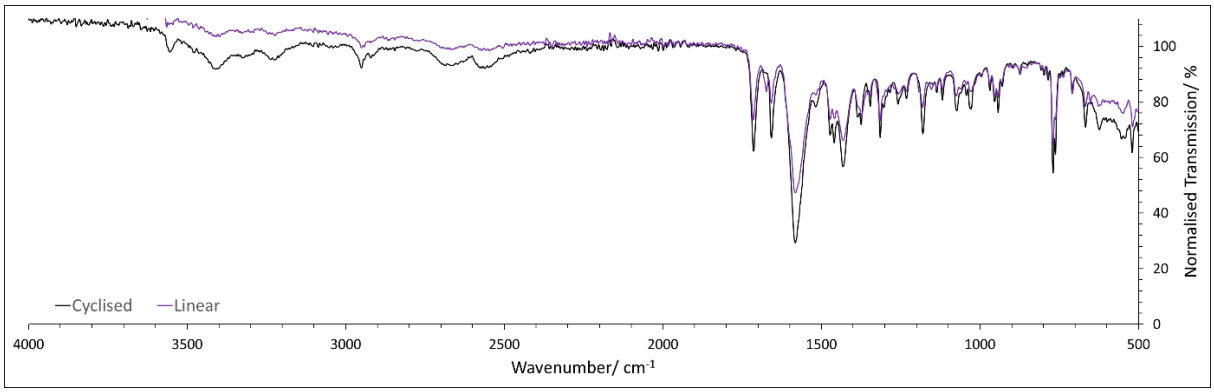

*Figure F. FTIR of **D1·1.5H$_2$O** crystals labelled as 'Cyclised' overlaid with the spectrum of **D1·1.5H$_2$O** post-heating, labelled 'linear'.*

Little can be gleaned from the FTIR in Figure F, there are no expected broad bands at 3000 cm^{-1} denoting O-H stretches, and because the isomerism presents a large structural change its expected

the FTIR to be different between the two forms. A drop in normalised intensity from the cyclised to linear form could suggest a decrease in the amount of cyclised form present, potentially suggesting the heating time was insufficient to convert to the linear form. Alternatively ambient light may have been sufficient to isomerise the majority of the sample back to the cyclised form in the time between the oven and the spectrometer.

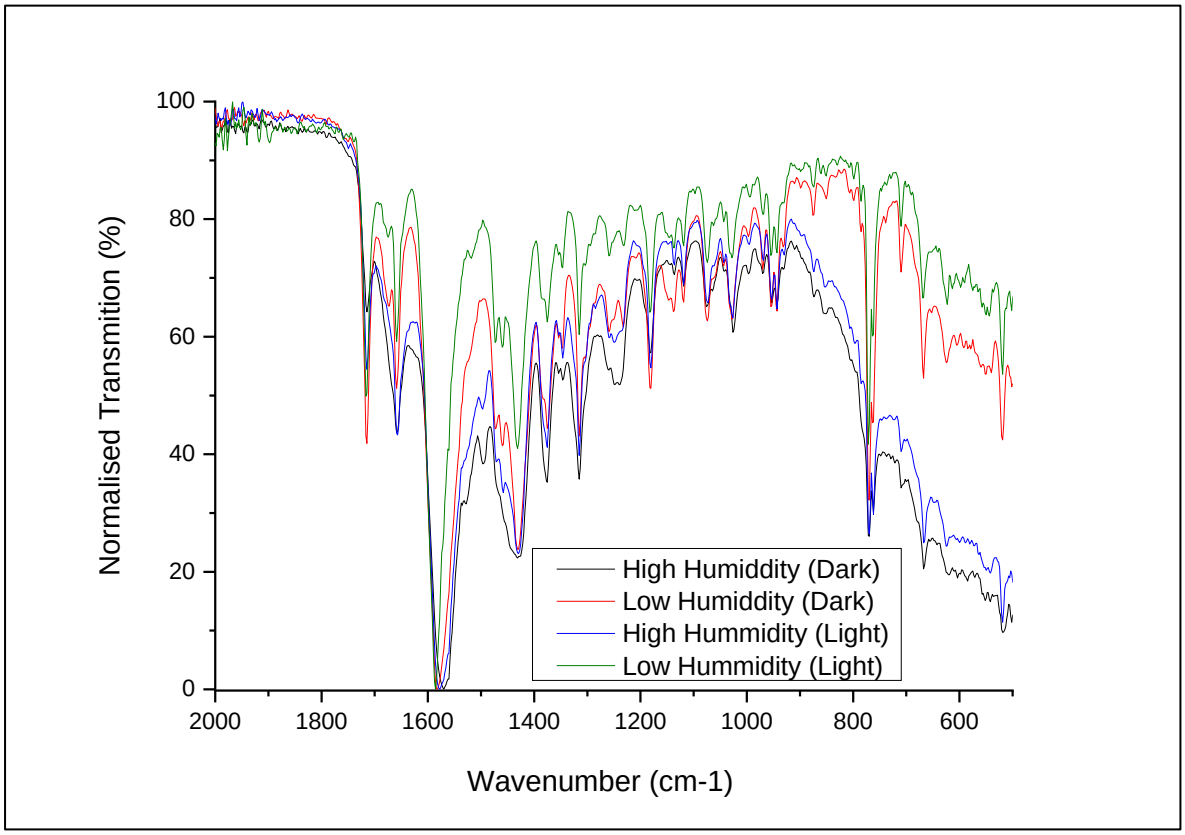

Figure G. FTIR analysis of samples exposed to different lighting/humidity conditions.

These results in Figure G were inconclusive, likely due to residual solvent impurities in the samples resulting in wide, overlapping peaks. In this case **Error! Reference source not found.** refers to high humidity as >99 % humidity and low humidity as 17 % controlled by placing samples in a desiccator with binary salt slurries.[3] The data range has been cut-off at 2000 cm^{-1} as similar to Figure F, there was no obvious peaks beyond this point.

References

1 N. Mallo, E. D. Foley, H. Iranmanesh, A. D. W. Kennedy, E. T. Luis, J. Ho, J. B. Harper and J. E. Beves, Structure-function relationships of donor-acceptor Stenhouse adduct photochromic switches, *Chem. Sci.*, 2018, **9**, 8242–8252.

2 G. R. Fulmer, A. J. M Miller, N. H. Sherden, H. E. Gottlieb, A. Nudelman, B. M. Stoltz, J. E. Bercaw, K. I. Goldberg and M. Beckman, NMR Chemical Shifts of Trace Impurities: Common Laboratory Solvents, Organics, and Gases in Deuterated Solvents Relevant to the Organometallic Chemist, *Organometallics*, 2010, **29**, 2176–2179.

3 L. Greenspan, Humidity Fixed Points of Binary Saturated Aqueous Solutions, *J. Res. Natl. Bur. Stand. Phys. Chem.*, 1976, **81**, 89–96.